The RESEARCH LABORATORY
of
ELECTRONICS
at the
MASSACHUSETTS INSTITUTE OF TECHNOLOGY
CAMBRIDGE, MASSACHUSETTS 02139

Touch Lab Report 10

Investigation of the Internal Geometry and Mechanics of the Human Fingertip, *in vivo*, using Magnetic Resonance Imaging

Kimberly Jo Voss and Mandayam A. Srinivasan

RLE Technical Report No. 622

January 1998

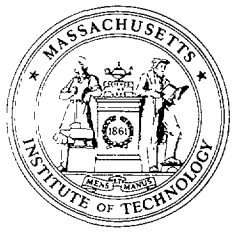

Touch Lab Report 10

Investigation of the Internal Geometry and Mechanics of the Human Fingertip, *in vivo*, using Magnetic Resonance Imaging

Kimberly Jo Voss and Mandayam A. Srinivasan

RLE Technical Report No. 622

January 1998

Sponsored by the National Institutes of Health
NIH-5-ROI-NS33778

The Research Laboratory of Electronics
MASSACHUSETTS INSTITUTE OF TECHNOLOGY
CAMBRIDGE, MASSACHUSETTS 02139-4307

Abstract

To gain insight into the mechanistic bases of the human tactile sensory system, a deeper understanding of the biomechanical behavior of the skin and subcutaneous tissues is needed. One approach has been to develop a series of increasingly complex and detailed biomechanical models of monkey and human fingerpads which can be used to generate testable hypotheses on neural coding or predict neural response. Although three dimensional (3-D) models of human and monkey fingertips with realistic external geometry and multi-layered interior have been completed, the geometry and material properties of the internal layers have been idealized. Empirical data on the deformation behavior of the internal layers is essential for validating these models.

This thesis is concerned with the use of Magnetic Resonance Imaging (MRI) to obtain realistic internal geometry and deformation of the tissue layers of the *in vivo* human fingerpad. The fingerpad was statically loaded with various indentors to examine the effects of indentation depth and indentor shape on tissue deformation. Geometric surfaces which simulate edges and surfaces of objects such as a line load, various sized rectangular bars and cylinders were used to load the fingertip. Utilizing a 4.7 Tesla magnet and a RARE sequence, images with 125μm x 125μm in-plane resolution were used to obtain data on three subjects. Digital image processing techniques were used to filter the images and to detect the boundaries of the tissues located in the fingertip. Edge detection algorithms based on conformable contours ("snakes") allowed for separation of tissue layers. Published data on histology, and anatomy were used to identify each tissue layer in the fingertip.

The geometric information extracted from each tissue layer was used to examine tissue deformation during loading and will eventually be used to help build computational models. This data revealed that the soft tissues of the fingerpad act as low pass filters, resulting in the removal of high spatial frequencies such as corners inside the fingerpad. Additionally, the results indicate that the fingerpad is compressible under load. MRI proved to be a powerful tool to visualize soft tissue structures under *in vivo* conditions. Its high resolution and ability to discriminate tissue layers makes it a useful tool for further investigation of static loading and, in the future, dynamic loading of the fingertip.

Table of Contents

Chapter 1

Introduction

1.1 Introduction

Humans use five sensory systems to explore their environment. The tactual system is unique in that it uses a large number of different types of sensors in the skin, muscles, and joints to create a feedback system for motion and coordination. Without the sense of touch, it becomes difficult or even impossible to manipulate objects, feel pain or pleasure, and to move through space. This feedback system has proven to be far superior to any similar man made system and, therefore, can be viewed as an "ideal" model. A deeper understanding of this system would allow engineers and scientists to develop and improve existing virtual reality systems, human-machine haptic interfaces, rehabilitation devices and machine sensory components.

1.2 Human Haptic System

Haptics is defined as the study of all the aspects of the hand-brain system involved in manual tasks such as exploration and manipulation. It consists of the biomechanical, sensory, motor and cognitive subsystems. The tactual sensory information from the hand in contact with an object can be divided into two classes: 1) tactile information and 2) kinesthetic information. Tactile information originates from the sensors embedded in the skin within and around the contact region. Kinesthetic information, referring to the sense of position and motion of limbs along with the associated forces, arises from sensory receptors in the skin around joints, joint capsules, tendons, and muscles, together with neural signals derived from the motor commands (Srinivasan, 1995).

The sequence of events involved in tactile perception can be seen in Figure 1.1. First, the skin comes into physical contact with an object which applies a mechanical, chemical, thermal and/or electrical stimulus to the skin surface. Additional stress and strain resulting from weight and position of the object are also imposed on the muscle and joint receptors. Depending on the type, magnitude, and location on the skin, this stimulus triggers a response from specialized receptors. Specific nerve endings respond depending on the relevant stimuli, for example, thermoreceptors respond to changes in skin temperature, mechanoreceptors fire based on mechanical action (force, vibration, slip) and nocioreceptors react only to intensive stimuli that cause pain. The neuroreceptor responds by generating an electrical discharge (or "action potential") in the afferent nerve fiber. Secondary neurons propagate the signal further up the spine and into the thalamus

region of the central nervous system (CNS). Here, third-order neurons complete the path to the somesthetic area of the cortex where the corresponding sensations of pressure, temperature, or pain are registered [Seow, 1988]

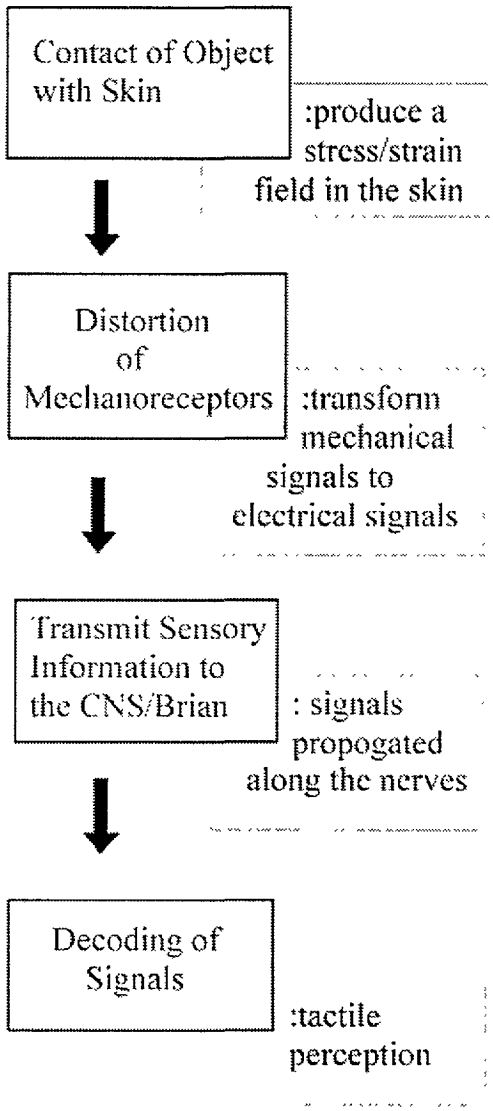

Figure 1.1: Demonstrates the sequence of events that occur in tactile sensing through mechanoreceptors.

The glabrous (hairless) skin of the fingertips and palms play the largest role in tactile exploration. The fingertip is highly innervated with sensory receptors which map to large areas in the cortex. Glabrous skin hosts five different types of sensory receptors: free

receptors, Meissner's corpuscles, Merkel's disks, Pacinian corpuscles, and Ruffini corpuscles. Free receptors or nerve endings are triggered by noxious stimuli and are located near the surface. Just below the skin surface, Meissner's corpuscles detect motion from the ridges of the skin and function similar to velocity sensors. Merkel disks which are located deeper in the skin and act as pressure sensors. Located deeper in the skin (the dermis), the Pacinian corpuscles function similar to accelerometers and aid in detection of light touch and vibration (around 250Hz). Finally, Ruffini corpuscles lie slightly deeper in the dermis and detect pressure, skin shear and change in temperature (Burdea, 1996).

Tactile mechanoreceptors are classified according to the type of response produced during a constant stimulus. The slowly adapting receptors (SA) exhibit a very slow rate of decay of their discharge rate, while rapidly adapting receptors (RA) have a fast rate of decay. Table 1.1 describes the rate of adaptation, stimulus frequency, receptive field and function for each receptor type.

Receptor Type	Rate of Adaptation	Stimulus frequency, Hz	Receptive Field	Function
Merkel Disks	SA-I	0-10	Small, well defined	Edges, Shape
Ruffini Corpuscles	SA-II	0-10	Large, indistinct	Static force, skin stretch
Meissner Corpuscles	RA-I	20-50	Small, well defined	Velocity, moving edges
Pacinian Corpuscles	RA-II	100-300	Large, indistinct	Acceleration, vibration

Table 1.1 Characteristics of Skin Mechanoreceptors (adapted from Burdea, 1996).

The shape of the fingerpad plays a large role in how these sensors work together to collect information. The pulp of the finger consists of bone, nail, blood vessels, fat, nerves, sweat glands and skin. The convex shape of the fingertip makes it conducive to grasping and tactile sensing. The shape allows for location of objects in contact with the skin and the skin ridges along with moisture from sweat glands make the outer surface an ideal gripping surface. The subcutaneous fat allows for compliance of the finger in conforming to objects which aids in tactile sensing and gripping.

1.3 The Problem

In order to gain a deeper understanding of how the fingertip encodes spatial and temporal signals, the mechanical behavior of the fingertip tissue needs to be examined. Phillips and Johnson hypothesized that certain relevant stimuli (i.e. different combinations of stress/strain) trigger particular responses in mechanoreceptors (Phillips and Johnson, 1981). The receptors encode information both spatially and temporally from the stress and strain fields created by the stimulus on the skin surface. To gain insight into neural coding of tactile information, an understanding of the biomechanical behavior of the fingertip structures is necessary.

The problem lies in the fact that at present, non-invasive research methods limit what can be studied on *in vivo* subjects, which means relevant stimuli for various mechanoreceptors and their relative importance in manual tasks remains largely unknown. One step towards examining these relevant stimuli is to build and test mechanical models of the fingerpad for stress and strain fields. Mechanistic models have

the advantage of testing hypothesized relevant stimuli for each specific class of receptors and provide a method to predict the results of biomechanical, neurophysiological and perceptual experiments.

One way to develop a mechanical model is to use the finite element method. This requires building a model of the fingerpad which requires determining the actual interior and exterior geometry. In previous studies, Dandekar and Srinivasan constructed 3D models of primate fingerpad for finite element analysis and also measured surface deformation of the human fingertip *in vivo* by indenting with various sizes and shapes (Dandekar and Srinivasan, 1995). They used a videomicroscopy system to obtain external geometry information and to determine surface deformation under load (Dandekar, et al, 1995). Approximate internal geometry information was used to construct the interior of the models.

Dandekar and Srinivasan (1996) found that strain energy density at the receptor location is directly related to the static discharge rate of the slowly adapting afferents. They showed that strain energy density is a direct measure of the distortion of the receptor caused by deformation of the tissue. Additionally, they showed that the model geometry significantly influences the performance of the model. Therefore, the idealized model needs to be more realistic, which in turn, requires data on geometry and mechanical behavior of soft tissues beneath the skin.

1.4 The Approach

This research project hopes to further improve the finite element models by utilizing Magnetic Resonance Imaging (MRI) to obtain functional information about internal and external geometry of the fingertip. Image processing techniques were used to capture tissue edges and to generate the geometric profiles of each tissue type including epidermis, dermis, subcutaneous fat, bone and bone marrow . Furthermore, the fingerpad was indented with various shapes which simulate edges and surfaces of objects such as line load, various sized bars and cylinders. These loads were applied to the index finger 1mm proximal to end of distal phalanx (bone).

By varying the depths of the indentors, the biomechanical behavior of each tissue and overall composite behavior was visualized. Static tissue behavior during loading was examined to look for compression, strain, and surface profiles. Superposition techniques of the MRI images provided insight to the effects of size and depth on these properties. This data will eventually be used to verify performance of the computational models.

Knowledge gained from this research project will result in a better understanding of the biomechanics of the fingerpad, which is critical in developing constitutive models of the tactile system. These models and the knowledge gained can be used to design improved robotic and prosthetic sensors, rehabilitation devices, tactile communication devices, diagnostic and functional sensory tests, and virtual haptic devices.

1.5 Thesis Overview

This thesis discusses experimental methods and procedures used to obtain MRI images of the fingerpad both with and without static load. Computational image processing techniques were used to extract edges and to aid in image registration. The results will be used in future work on improving constitutive models.

Chapter 1 gives a brief introduction to the problem and direction of this project. Chapter 2 reviews previous work completed in high resolution MRI imaging of the fingerpad and fingerpad modeling. Also, this chapter discusses anatomical structures of the fingerpad and what geometric structures this study hopes to resolve from the MRI images.

Chapter 3 reviews the basics of MRI to help set a framework for the design methods used in this study. Chapter 4 presents experimental methods and protocols for MRI techniques and loading methods. Results of the MRI images will be presented in Chapter 5 along with a discussion of issues related to signal-to-noise ratios. Chapter 5 also covers anatomical correlation of MRI images with anatomy and histology studies of the fingerpad.

Chapter 6 addresses image processing techniques and edge detection algorithms utilized to obtain geometric data. Results of edge detection and image registration techniques will be shown to illustrate the effects of static loading on the fingerpad. Chapter 7 explores the biomechanical behavior observed in this study. And finally, Chapter 8 discusses the

results, suggests future application of this research, and reviews questions that remain unanswered by this research project.

Chapter 2

Background

2.1 Examining tissue mechanics of the human fingerpad

The fingerpad is the most commonly used part of the body for obtaining tactile information. When a fingertip is loaded with a shape, the soft tissues deform to resist the applied load. As the load increases, the tissues respond by increased displacement, accommodation and resistance. One non-invasive method for looking at this process is through the use of MRI. MRI techniques produce functional or structural information of soft tissues, as well as, bone. To extract information from the image, a method of edge detection is needed to separate tissue structures so that tissue location and displacement under load can be measured. However, MRI images are non-uniform in intensity and therefore image processing in order to extract the data.

2.2 Previous Work

To date, most mechanical behaviors of biological tissues and especially that of skin have been obtained from *in vitro* experiments. Studies show a significant difference between *in vivo* and *in vitro* tests due to loss of fluid, changes in the differential proteins and alterations in boundary conditions [Lanir, 1987]. Due to the difficulties associated with animal and human studies, limited models and information exists.

2.2.1 Attempts at fingerpad modeling

Phillips and Johnson [1981a; 1981b] recorded the neural responses of slow adapting, type I mechanoreceptors in monkey fingers resulting from steady indentations of rectangular bars. To calculate the stress and strain values at the mechanoreceptors, they modeled the fingerpad to be a homogeneous, isotropic, incompressible and linearly elastic half-space in a state of plane stress or strain with small deformations. They showed that maximum compressive strain profiles calculated by the model closely agreed with the recorded neural response profiles for a range of periodic and aperiodic gratings. Similar studies using a linear, homogeneous , isotropic, viscoelastic, infinitely wide, flat medium (Van Doren, 1987), showed that normal strain triggered mechanoreceptors. Although these models approximately predict the neural responses, they use broad assumptions which do not take into account the geometrical shape or behavior of the fingerpad. In addition, they cannot account for changes in area of contact or non-linear behavior.

The "waterbed" model (Srinivasan, 1989) predicted skin surface deflection profiles of monkey and human fingerpads under line loads. The skin was modeled as an elastic

membrane which encompassed an incompressible fluid. Because of the uniform tension of the membrane and uniform pressure field within the fluid, this model provided highly accurate profiles of skin deformation. The limitations of this model are that it cannot predict responses of the receptors at different locations in the skin.

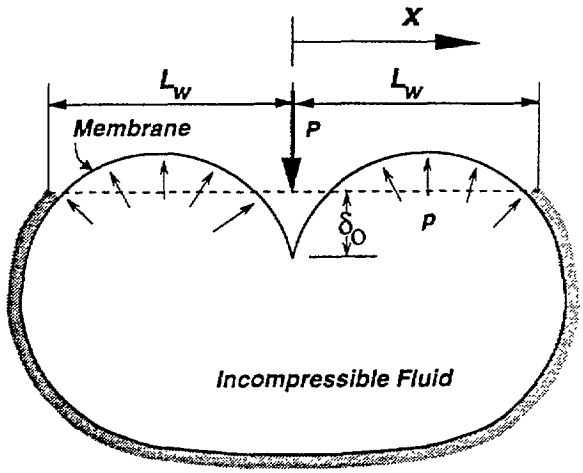

Figure 2-1: Shows a cross section through the "waterbed" model of the primate fingerpad skin. The dashed line is the resting state of the model and the solid line is the deformed state under point load.

Gulati and Srinivasan (1995) took the modeling another step when they developed a Kelvin type model to explain nonlinear visoelastic force responses observed in their experiments. They indented human fingerpads with point, flat circular and flat plate indentors and measured the temporal force response. From this data, they developed a lumped parameter model consisting of non-linear spring in parallel with a spring and dashpot in series. This model matches the experimental data quite well.

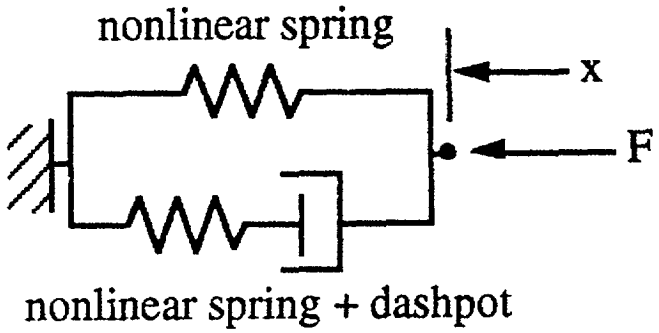

Figure 2-2: Proposed nonlinear model to predict fingerpad force response.

To expand modeling to 3D, Dandekar and Srinivasan(1996) developed 3D finite element model of both human and monkey fingertips which were composed of several layers of tissues. The realistic external geometry was captured using video microscopy techniques and idealized tissue layer geometry was assumed. Although the material was assumed to be linear elastic, the predictions of surface deformation matched empirical data quite well. From these models, they found strain energy density and maximum compressive strain to be excellent predictors of relevant stimuli for mechanoreceptors. Additionally, the models showed that geometry played a significant role in the ability of the model to accurately predict experimental deformations and neural response recordings. Figure 2.3 shows an example of this 3-D model where the different grayscales indicate different layers of the finger.

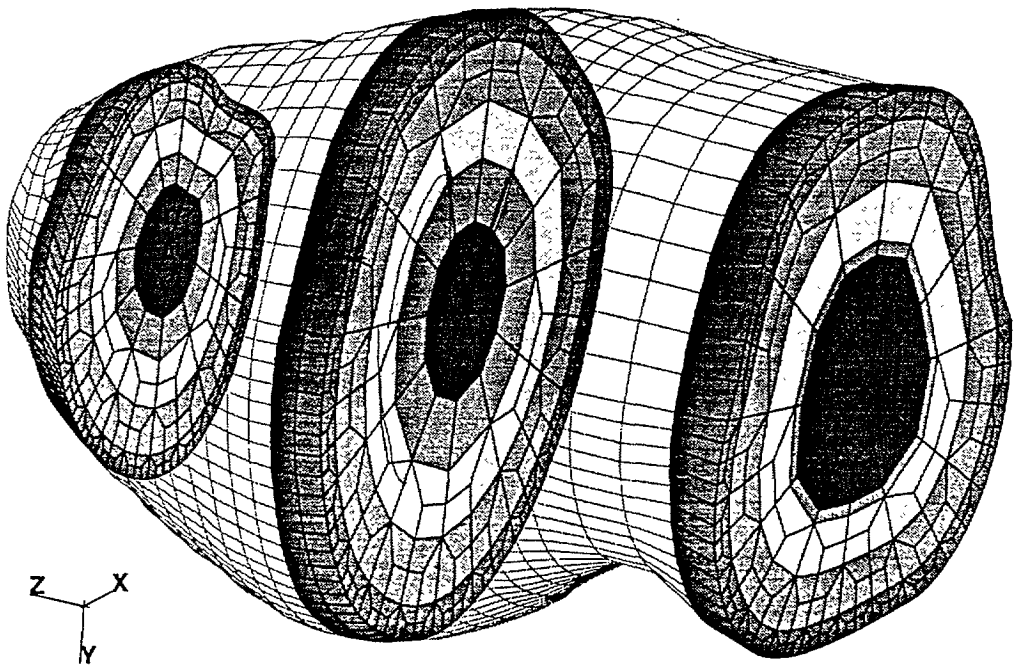

Figure 2-3: Three slices of the monkey fingertip are shown with elements shaded to show layers of tissue (Dandekar and Srinivasan, 1996).

Acquiring the data required for the next iteration these of models is the subject of this thesis. In this research project, MRI images were used to obtain information on internal and external geometry of the fingertip as well as its mechanical behavior. In order to extract deformation data from the image, the internal structures were tagged to determine their location and displacement when the fingertip was under load. An MRI image contains intensity, texture and spatial information which aided in determining tissue type, location and boundaries.

2.2.2 Previous MRI Imaging of the Fingerpad

Since finite element models improve with increased resolution, the goal of this thesis was to obtain maximum possible resolution in the images of the fingerpad. Several studies of

the hand and wrist have been completed with ranges of resolution between 1.5 mm and 3.0 mm. Only a few research publications were found which examined specifically the fingerpad. A closely related study by Hodgson utilized MRI to evaluate the integrity of hyaline cartilage in the distal interphalangeal joint [Hodgson, et al, 1995]. Hodges, et al, used a wide range of MRI imaging conditions and found a protocol that allows for maximum contrast of all finger structures. A range of spin echo protocols with chemical shift suppression where used to visualize the functional structures of the finger. They found that a spin-echo protocol with a TR = 1500 msec and a TE = 30 msec can capture structural data with an in-plane resolution of 0.075 x 0.150 mm for a slice thickness of 1 mm in 13 minutes. Although this protocol does not optimize contrast for any particular structure, it allows for maximum visibility of all structures.

In examining specifically the skin, several recent studies found differentiation of skin layers can be achieved with the use of a special coils that lay on the skin surface. One particular study [Bittoun et al.,1990], using a 1.5 Tesla magnet, achieved an in plane resolution of 70 x 390 μm with a 1.2mm slice thickness of human calf and heel skin. A more recent study, utilizing a 1.5T magnet, achieved 78 x 78x 800 μm^3 voxel size utilizing a surface coil and a 3D FLASE protocol [Song et al., 1997]. Additionally, they scanned the skin utilizing a 3D pulse sequence.

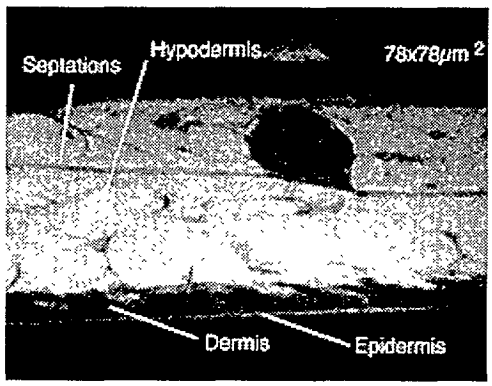

Figure2-4: A 3D FLASE image of a male's calf utilizing a 3-cm receiver coil. The epidermis, dermis, hypodermis, and septations of the hypodermis have been labeled. [Song et al., 1997]

The goal of the thesis is to obtain highest possible resolution while also achieving high functional contrast. Initially, the project hoped to achieve visualization of the all structures of the fingerpad, especially the dermis and epidermis. This meant to effectively examine biomechanical behaviors of the skin under load near nerve endings, and spatial resolutions of 10-40 μm were desired .

2.3 Anatomy of the fingerpad

2.3.1 Object Handling

The entire human finger plays a major role in the exploration of objects and tactile recognition. Each structure of the finger plays an intricate role in the function and positioning of the finger during any activity. The flexor digitorium profundus (FDP), flexor digitorium superficialis (FDS) and intrinsics muscles work in conjugation to flex (bend) the finger. The extensor digitorium communis muscle acts as the actuator to extend the fingers. A pulley system in the hand allows these muscles to direct the motion. The muscles operate as agonist and antagonist with both actively driving the direction of motion. Along with the use of the intrinsic muscles and the flexible arch systems of the hand, the human hand can conform to the shape of an object, manipulate,

rotate, lift or set it down. These systems allow for the exploration of an object. However, it is the conformable fingerpad which gives the largest sensory feedback. Figure 2.5 shows the intricate complexity of the finger.

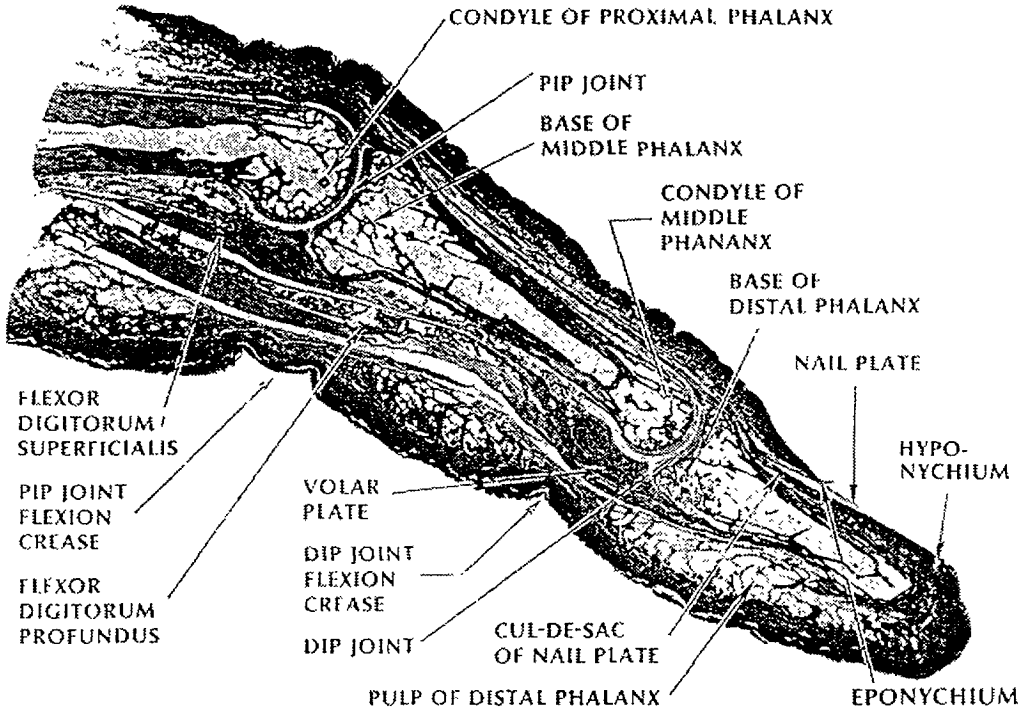

Figure 2.5: Sagittal section through the finger demonstrates the intimate relationship between tendons, bone, skin and flexion creases (Sandzen, S., "Atlas of Acute Hand Injuries", p. 24, 1980).

2.3.2 The Human Fingerpad

The human fingerpad is comprised of the distal phalanx and a nailbed which provides rigidity to the pulp of the finger during manipulation of an object. The nail bed or matrix anchors the nail plate to the finger and helps maintain the integrity of the nail. The depression between the periphery of the nail plate and the skin which demarcates the nail laterally is called the paronychium. At the proximal end of the distal phalanx, the

extensor digitorium communis (EDC) and flexor digitorium profundus (FDP) attach and drive the motion of the distal third of the finger.

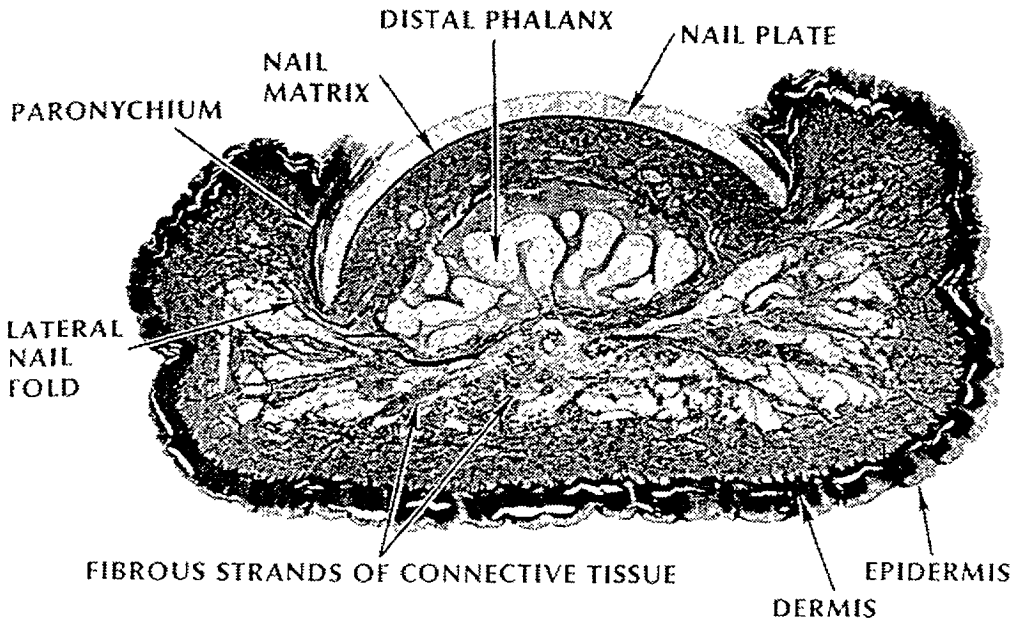

Figure 2.6: Cross section through the distal phalanx (Sandzen, S., "Atlas of Acute Hand Injuries", p. 24, 1980).

Adipose tissue makes up most of the belly of the fingerpad which functions as a compliant pad to enhance gripping by helping skin to conform to the objects held. These structures are all encapsulated by the largest organ in the body, the skin. The pulp of the distal phalanx is held in place proximally at the transverse flexion crease of the distal interphalangeal (DIP) joint. Multiple tough, fibrous bands tether together the periosteum of the distal phalanx and the dermis of the skin [Sandez, 1980]. Additionally, these bands encase and help to maintain position of the fat-containing subcutaneous tissue. Figure 2.6 illustrates the connective tissue architecture of a cross section through the distal phalanx.

2.3.3 Skin

The skin is made up of three layers: epidermis, dermis, and hypodermis. The volar skin of the fingerpad contains papillary ridges which help prevent slippage and possibly aid in detection of temporal information during tactile recognition. The dorsal skin is thinner, more mobile and more pliable than volar skin. The dorsal skin lacks the fibrous septae seen in volar skin. Nerves and blood vessels which innervate and supply blood to the skin run parallel to the surface and are protected by longitudinal fascial septae. Figure 2.7 shows the relationship between the three layers of the skin.

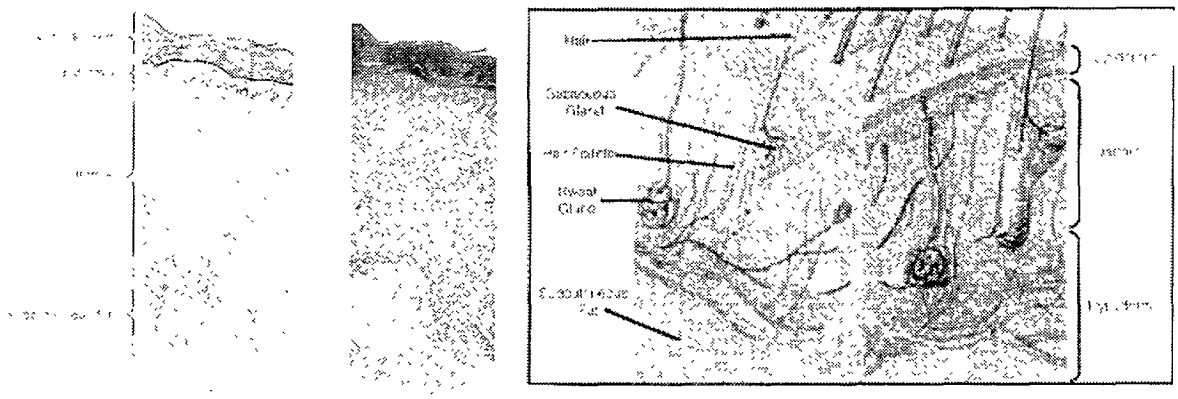

Figure 2.7: The two images show a cross section through the human skin. The three cutaneous layers of the skin includes the epidermis, dermis and hypodermis (Tubiana, R., "The Hand", p. 108, 1981 and Martini, F., "Fundamentals of Anatomy and Physiology", 3rd ed., p. 150, 1995.).

The epidermis is comprised of four layers: the stratum corneum, consisting of dead cells, and inner layers (basal, malpighian and grandular) of living cells in various stages of differentiation. The epidermis protects the body from water loss, impact and ultraviolet rays. Additionally, the epidermis acts as one of the body's thermoregulators and one of the primary sensory organs. The stratum corneum varies in thickness from 20 μm to 2

mm [Tubiana, 1981] and the epidermis from 100μm to 600μm for various parts of the body [Song et al., 1997].

Located below the epidermis is the dermis, which consist of about 60-65% water, 20-25% collagen, elastin, and ground substance [Song et al.,1997]. The junction line between the dermis and epidermis is characterized by alternating dermal and epidermal protrusions which creates a sinusoidal border known as the papillary border. The dermis consists of two layers, the superficial and reticular which provide strength and elasticity to the skin. Below the dermis, the hypodermis contains mostly fat tissue which functions as an energy storage unit and protective cushion.

Chapter 3

Physical Principles of Magnetic Resonance Imaging

3.1 Fundamentals

Electrons, protons and neutrons are all elementary particles of an atom which form the building blocks of living tissues. Electrons have a minute negative charge and protons have a positive charge of the same magnitude. Neutrons have no net charge. All three particles posses a property called spin, and may be thought of as spinning rapidly on their own axis like tiny tops. The combination of spin and electric charge produces a small circulating current in each particle that results in the creation of a tiny magnetic field around the particle.

The orientation of the magnetic moments of the protons and neutrons in a sample of nuclei create a net magnetization termed the magnetic moment. Without an external

magnetic field, the spins point randomly resulting in a net magnetization of zero as seen in Figure 3.1.

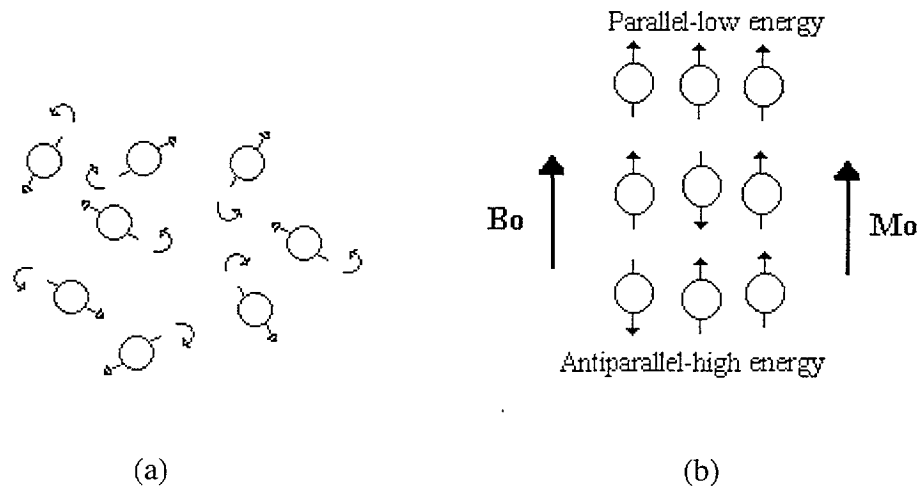

Figure 3.1: (a) In the absence of an applied magnetic field, the proton dipole moments orient in random directions. (b) Once a magnet field Bo is applied, the nuclei align themselves with the field. A majority of these align parallel to the field which creates an effective magnetic moment called M_0.

When a magnetic field is applied to the substance, however, many of the nuclei become oriented either parallel or antiparallel to the magnetic field (Figure 3.1). Usually, more nuclei orient parallel verses antiparallel to the applied field. The nuclei in the two orientations differ in energy; however, the energy difference is very slight (about 1/1000 of thermal energy at body temperature). The energy difference, as well as the number of nuclei oriented antiparallel to the applied field, increases with the strength of the applied magnetic field. Typically in medical applications, magnetic fields of 0.2-1.5 Tesla are used to polarize the protons and neutrons.

The source of signal found in human imaging comes mainly from protons in cellular water. The human body is primarily fat and water. Fat and water are high in hydrogen

atoms which make the human body to be composed of approximately 63% hydrogen atoms (Hornak J., 1996). Typically, hydrogen proton nuclei are used to generate images because they are the most abundant nuclei in tissues and the most sensitive of all nuclei to magnetic fields and radiowaves. As an external field is applied, the nuclei (or spins) rotate or precess about the magnetic field until they orient themselves with the external magnetic field (Figure 3.2).

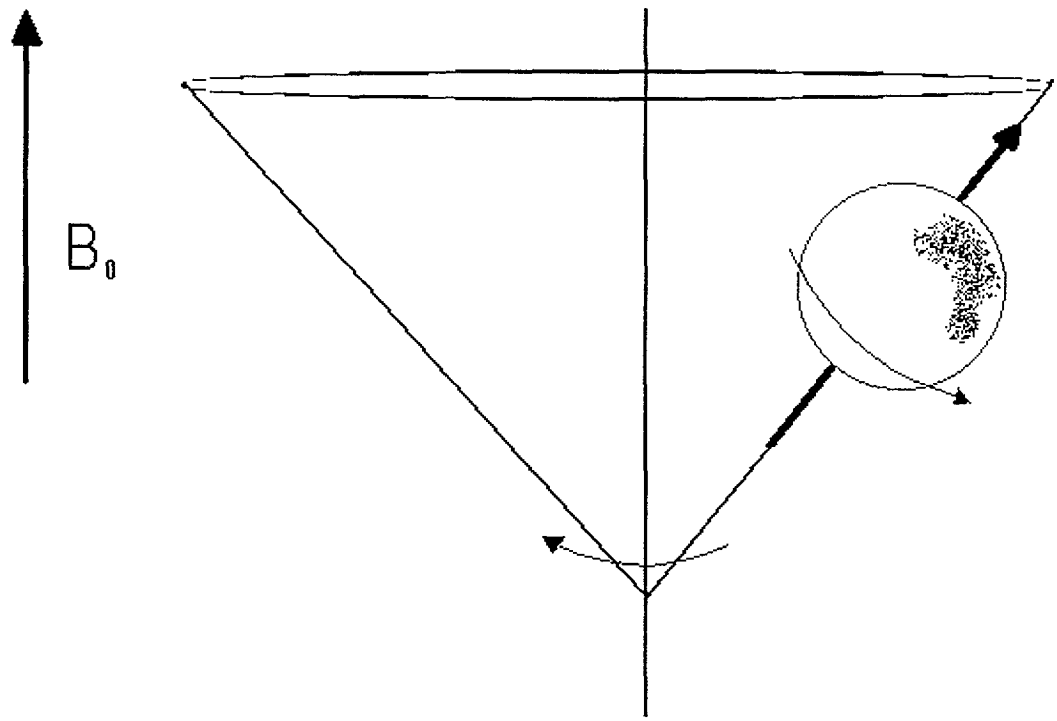

Figure 3.2: This image illustrates the precession of the proton around the axis of the applied magnetic field (B_0), as well as, its own natural rotation about its central axis.

The frequency at which these nuclei precess is called the Larmor frequency. The Larmor frequency (ω) is given by

$$\omega=\gamma B \qquad (3.1)$$

where B is the external magnetic field and γ is the gyromagnetic ratio of the magnetic moment of the nuclei to their angular momentum which depends on the strength of the external magnetic field and the internal magnetic properties of the nuclei (Kean et al.,1986).

The Larmor frequency for hydrogen nuclei is approximately 64 MHz at 1 Tesla. The Larmor frequency is unique for each type of nucleus and all identical nuclei emit a signal of the same frequency. This is crucial in the spatial encoding of the signal into an image. A radio frequency field at a frequency equal to the Larmor frequency will be in resonance with the magnetic moments, hence the term magnetic resonance (MR).

3.2 Image Formation

To create an image, a short radio frequency (RF) pulse equal to the Larmor frequency of the precessing spins is delivered to the tissue. This causes the net longitudinal magnetization to rotate out of alignment with the external magnetic field (Figure 3.3).

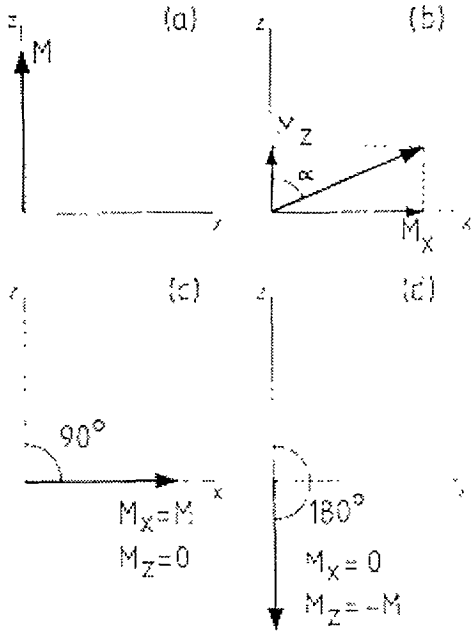

Figure 3.3: (a) The magnetic moment M is in the z direction when in equilibrium. (b) The application of an RF pulse tips the magnetic moment towards the x axis through an angle α. The magnetic moment is broken down into its components to help illustrate the reduction of the signal in the z direction and the increased signal in the x direction. (c) & (d) If a large enough RF pulse is given, the magnetic moment will be tipped by 90^0 or 180^0. (Adapted from Kean et al, "Magnetic Resonance Imaging", p.12, 1986)

The angle of deviation, also known as the flip angle, depends on the amplitude and/or the duration of the RF pulse. The resulting vector has a longitudinal (longitudinal magnetization) and horizontal component (transverse magnetization). As the spins begin to realign themselves, the changing magnetization vector can induce a current in a receiving coil, hence yielding the MR signal (Figure 3.4). At a given time, the MR signal

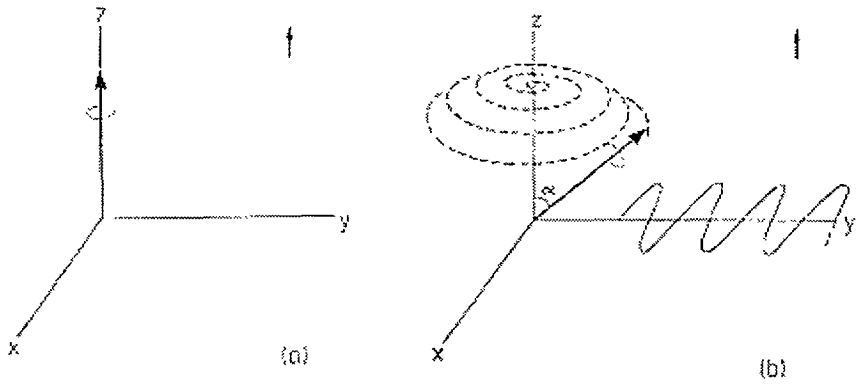

Figure 3.4: (a) A single proton is aligned in a magnetic field. (b) As the RF pulse pushes the magnetic moment through an angle α , a sinusoidal electromagnetic signal is produced along the y axis (This is also true for the x axis)

is measuring a particular spatial frequency. The spatial frequency information is fed into a computer algorithm which converts the data to a real image via a Fast Fourier Transform.

3.3 Decay of the Magnetic Resonance Signal

After the magnetic moment of a sample is pulsed out of alignment with the applied field, it tends to gradually become realigned with the field. The realignment process occurs as nuclei return to a lower energy state by releasing energy to the lattice of atoms around the nuclei. This form of realignment is termed spin-lattice relaxation. Relaxation is any process whereby a system returns to its original state after absorbing energy. At the same time, the precessing magnetic moment tends to separate into components through a dephasing process termed spin-spin relaxation. It is important to understand these processes because they determine the appearance of various tissues in a magnetic resonance image.

The spins maintain some of the excited state induced by an RF pulse for a characteristic time, but eventually will realign with the external magnetic field. Spin-lattice relaxation involves the gradual return of the magnetic moment of a sample to alignment with the applied magnetic field. The rate at which the magnetic moment (M) realigns with the applied field over time (t) is governed by the following equation:

$$M = M_0 (1-e^{-t/T_1}) \qquad (3.2)$$

In equation 3.2, T_1 is the spin-lattice relaxation time and M_0 is the original magnetization aligned with the applied field. The process of T_1 relaxation involves dissipation of energy to the chemical lattice and returns protons to a lower energy state with the help of thermal motion. As thermal motion increases, the rate of energy transfer also increases and relaxation by spin-lattice interactions occurs more readily. Since temperature is a measure of thermal motion, increasing the temperature of a sample leads to a reduction in T_1. Different substances have different T_1 values, signifying that spin-lattice relaxation occurs at different rates in different substances. T_1 varies between 300 and 1500 msec for human tissue because of differences in the interaction between the precessing magnetic moment and the particular molecular lattice.

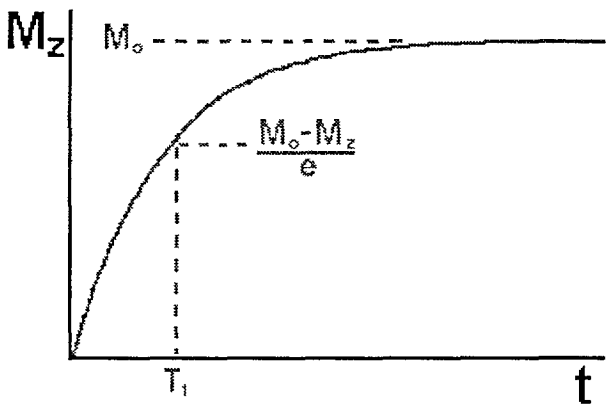

Figure3.5: A plot of the M_z verses time after a 90° RF pulse shows T_1 during the recovery of the magnetic moment to equilibrium.

3.4 T_2 Processes

Spin-spin relaxation occurs by a different mechanism. Initially, the magnetic moment of the sample begins aligned with the applied magnetic field. As the magnetic moment is tilted out of alignment by an RF pulse, the magnetic moment begins to precess about the direction applied field. The localized inhomogeneities in the applied field and the interaction between spins (hence the name spin-spin) cause the precessing magnetic

moment to separate into various components that precess at slightly different rates. Figure 3.6 shows this dephasing process which is termed spin-spin relaxation T_2.

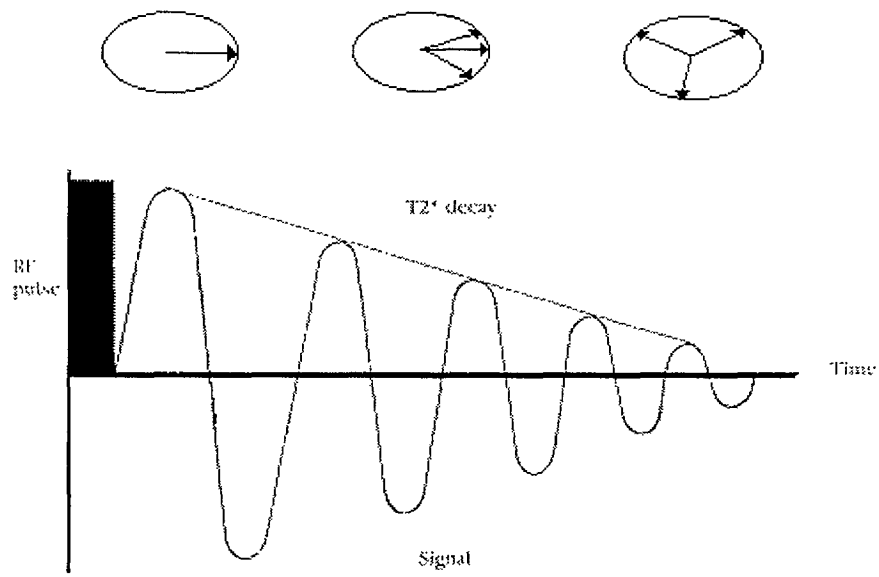

Figure 3.3 After excitation with a RF pulse, all spins rotate with the same frequency and phase. After the RF pulse, the spins begin to dephase, reducing the net transverse magnetization or T_2 decay (adapted from Beltran J., "MRI Musculoskeletal System", 1990).

This dephasing process, termed spin-spin relaxation or T_2 relaxation, leads to a decay in signal intensity characterized by the expression:

$$M = M_0 (1\text{-}e^{-t/T_2}) \qquad (3.3)$$

When the dephasing process is complete, each xy component of the signal is balanced by a component in the opposite direction, and the signal intensity falls to zero. The magnetic moment then begins to rephase and the magnetization vector continues to realign with the applied field until realignment is complete. It should be noted that T_2 can approach but never exceed T_1.

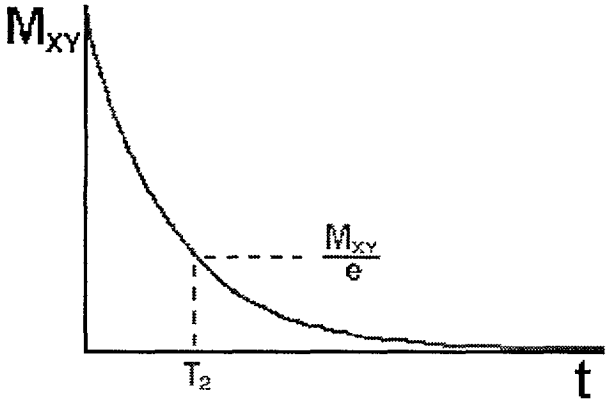

Figure 3.7: The plot illustrates the how T_2 can be determined from the transverse magnetization decay (adapted from Hornak J., "MRI", 1996).

The two factors which contribute to the decay of transverse magnetization are the molecular interactions and inhomogeneous T_2 from variations in B_o.

3.5 Pulse Sequences

The MR signal contains more functional information about all the tissues of a sample in which it originates that does the signal from any other imaging modality. Different spin sequences or alternations in RF sequences and amplitudes can be used to highlight different aspects of a sample. In pure spin density sequences the relaxation times T_1 and T_2 are difficult to measure exactly, making them difficult to use. However, other methods which take on various combinations of RF sequences to highlight proton density, T_1 and T_2 relaxation times and are more frequently used in clinical imaging. Pulse sequences heighten the differences in tissue relaxation times (T_1 and T_2) and thus provide necessary image contrast. The three pulse sequences most frequently used in musculoskeletal MRI are spin echo, inversion recovery, and fast scan techniques (Beltran, 1990).

Disease processes create changes in T_2 and T_1, especially T_2. Spin echo pulse sequences are designed to highlight the spin-spin relaxation time T_2. To measure T_2, the nuclei need

to be dephased to see the influence of spin-spin interactions on nuclei. In spin echo pulse sequences, the spins are excited by two RF pulses, one at 90° , and then after a short period of time, one at 180°. Allowing another period of time equal to the interval between the pulses, the spins will come back into phase and a signal is produced. This period of time from the initial 90° pulse until the echo signal is called the echo time (TE). Repeated applications of the 180° pulse results in multiple echo signals which can be used to improve the signal to noise ratio. The strength of each consecutive echo then reflects T_2 relaxation. Figure 3.8 illustrates echo's created from repeated 90 and 180 degree pulses.

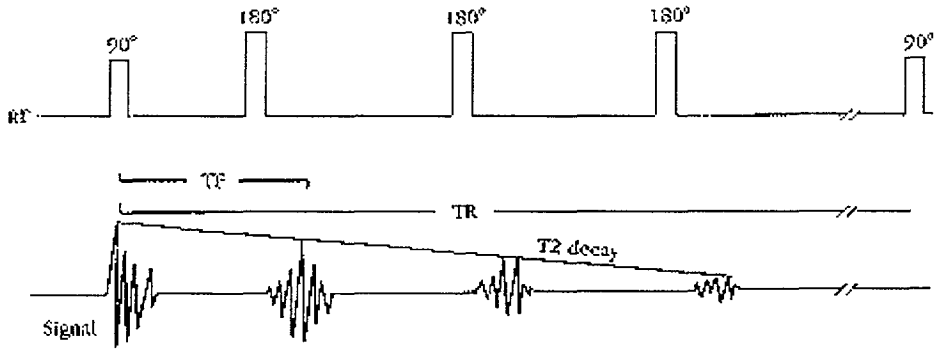

Table 3.8: Multiecho pulse sequence. A 90° pulse is followed by repeated 180° pulses to create multiple echoes. The reduction in amplitude of each subsequent echo reflects T_2 relaxation(adapted from Beltran J., "MRI Musculoskeletal System", 1990).

If the time between 90° pulses (Repetition time [TR]) is relatively long, the spins have enough time to return to complete equilibrium and T_1 relaxation occurs. If the spin echo sequence has a TR less than the 5 T_1 of the sample, the longitudinal magnetization does fully recover and is, therefore, smaller than initially. Following another 90° degree pulse,

this reduced longitudinal magnetization is tipped into the transverse plane. This reduction in a signal amplitude reflects the T_1 relaxation.

Fast scan techniques don't completely transform the longitudinal magnetization into transverse magnetization (limited flip angle excitation). For flip angles less than 30°, proton density dominates the image, and for angles of 30-60 degrees, T_1 relaxation determines the signal. If TE is comparable to the T_2 relaxation time of the sample, a T_2-weighted image is obtained.

3.6 Slice Selection

Isolating a single MRI slice involves selecting the spins in a plane through the object. Slice selection is achieved by applying a one-dimensional, linear magnetic field gradient during the period that the RF pulse is applied. A 90° pulse applied along with a magnetic field gradient will cause the spins which are located in a slice to rotate.

3.7 Phase Encoding Gradient

When an RF pulse with a given range of frequency is used to excite spins, a readout gradient (frequency encoding gradient) is turned on while the signal is measured. At different locations, the spins yield signals with different frequencies which can be decoded using Fast Fourier Transform. Another gradient (phase encoding gradient) which is activated between the excitation of spins and recording of signals causes the excited spins to rotate with a frequency specific to a location. Once the gradient switches off, the spins have different phases depending on their location.

3.8 Signal Processing

The image is obtained by transforming the signal acquired in the receiver coil or the free induction decay into intensity levels by Fourier methods. The signals are transformed along the read direction (or x axis) to gain frequency information and then along the phase encoding direction (y axis) to gather information about phase and locations. By converting the intensities of the peaks to intensities of pixels, the image topography can be displayed. The resolution of the image depends on the field of view (FOV) and the number of pixels per direction,

$$\textbf{Resolution} = \textbf{FOV/ \# pixels} \qquad (3.4)$$

which is determined by the magnetic field and set by the user.

3.9 Artifacts

As with any imaging modality, artifacts in MRI images can cause reduction in signal to noise or loss of contrast. These artifacts can stem from problems in sampling to motion of the sample. The following table summarizes these problems and their causes.

Artifact	Cause
RF Quadrature	Failure of the RF detection circuitry
Bo Inhomogeneity	Metal object distorting the magnetic field
Gradient	Failure in a magnetic field gradient
RF Inhomogeneity	Failure of RF coil
Motion	Movement of the imaged object during the sequence
Flow	Movement of body fluids during the sequence
Chemical Shift	Large B_o and chemical shift difference between tissues
Partial Volume	Large voxel size
Wrap Around	Improperly chosen field of view

Table 3.1: This table associates MRI image problems with their cause.

3.10 Noise

The relationship between the strength of a signal and the magnitude of the noise is often described in terms of the signal-to-noise (S/N) ratio. Since the signal increases approximately linearly with magnetic field intensity, whereas the noise increases more slowly, improved S/N ratios are obtained in higher magnetic fields and consequently the imaging times can be reduced. High S/N ratios also permit the imaging of thinner sections of tissue, and facilitate high-resolution magnified ("zoom") images of small regions. Among the disadvantages of a high field strength system are difficulties in obtaining multiple images of different sections simultaneously because of limitations in RF coil design, and some loss of image contrast caused by a reduction in differences in T_1 among tissues at higher field strengths.

3.11 Hardware Overview

Figure 3.9 displays a schematic representation of the major systems on a magnetic resonance imager. The magnet produces the B_o field for the imaging procedure. Within the magnet are the gradient coils for producing a gradient in B_o in the X, Y, and Z directions. Within the gradient coils is the radio frequency (RF) coil, which produces the B_1 magnetic field necessary to rotate the spins by 90^o or 180^o. The RF coil also detects the signal from the spins within the body. The scan room is surrounded by an RF shield which prevents the various RF signals from television and radio stations from being detected by the imager.

The computer controls all the components of the imager, including the RF frequency source and the pulse programmer. The source produces a sine wave of the desired frequency and the pulse programmer shapes the RF pulses. The RF amplifier increases the pulse power from mWatts to kWatts. The computer also controls the gradient pulse programmer which sets the shape and amplitude of each of the three gradient fields. The gradient amplifier increases the power of gradient pulses to a level sufficient to drive the

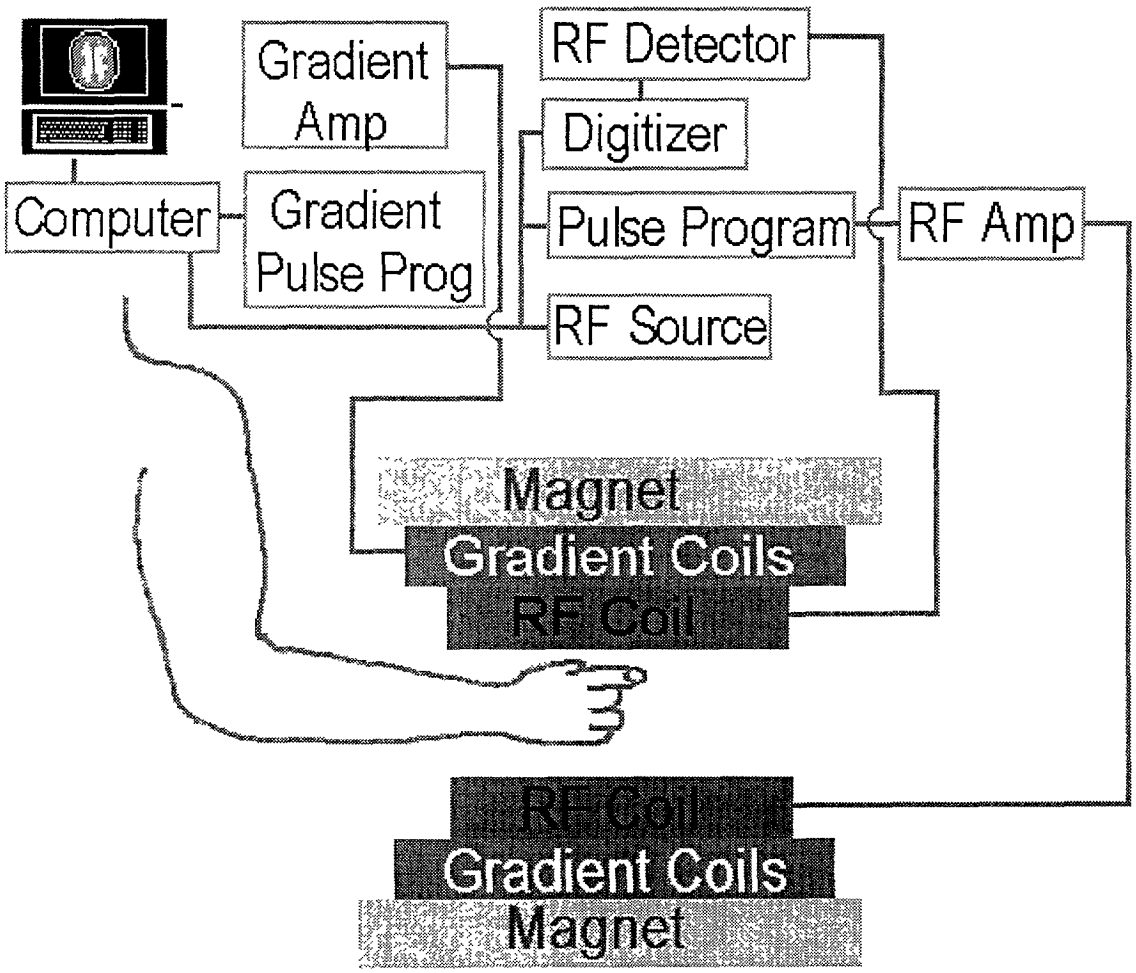

Figure 3.8: The figure shows the hardware set-up for imaging the hand. The computer acts as the main processor and system actuator (adapted from Hornak, J.,1996).

gradient coils.

The array processor, located on some imagers, is a device which is capable of performing a two-dimensional Fourier transform in fractions of a second. The computer off-loads the Fourier transform to this faster device. The operator of the imager gives input to the computer through a control console. An imaging sequence is selected and customized from the console. The operator can see the images on a video display located on the console or can make hard copies of the images on a film printer.

3.12 Safety

Although MRI does not utilize ionizing radiation, the safety areas of consideration are the use of strong magnetic fields, radio frequency energy, time varying magnetic fields, cryogenic liquids, and magnetic field gradients. Large magnetic fields can pull ferromagnetic articles into the bore of the magnet which can result in injury to the subject or damage the magnet and coils. Those who have ferromagnetic metal implants or foreign matter in their bodies should remain out of the magnetic field. The forces of the magnetic field can cause failure of the implant or displacement of the material causing further injury. Further precaution should be taken with credit cards and magnetic storage elements in magnetic fields since it can erase these items.

The United States Food and Drug Administration (USFDA) safety guidelines state that field strengths not exceeding 2.0 Tesla (T) may be routinely used. One study showed that imaging of human subjects in a 4.7T magnet can cause symptoms such as mild vertigo,

headaches, nausea, magnetophosphenes and metallic taste in mouth (Redington, et al). Furthermore, because of possible heating secondary to RF energy, the USFDA recommends the specific absorption rate be less that 0.4 W/Kg. The USFDA also recommends that the rate of change of magnetic field state (dB/dt) be less than that required to produce peripheral nerve stimulation.

High magnetic fields of 4.7T was used for this research in order to achieve the high resolution, good signal-to noise ratio and minimal chemical shift. Since the subjects sat out side the magnet, only their finger experienced the 4.7T field. At the region of their heart, they experience only about 0.34T. None of the subjects reported any symptoms or peripheral nerve stimulation. The Committee On The Use of Human as Experimental Subjects (COUHES) at MIT approved all the studies completed (No. 2275).

Chapter 4

Experimental Procedures and Methods

4.1 Introduction

At this point in time, very few methods for the direct measurement of *in vivo* tissue properties exist. One approach to examine the biomechanical behavior and to determine the mechanical properties is to measure the deflection of tissues under different loads to determine how a tissue deforms. Although videomicroscopy can image external surfaces, internal structures need to be imaged using a noninvasive method. Various visualization techniques are available on the market, but MRI is the only method which can differentiate between all soft tissues. In this study, static loading of the index fingerpad of the dominant hand was used to study the biomechanical behavior of the tissues. MRI images were taken of three male subjects using 6 different stimulus shapes indented to

two different levels. A Biospec micro-imager by Bruker Instruments, Inc. (Billerica, MA) with a 4.7 Tesla (T) static field strength was used. Approval for human subject studies was granted by MIT's COUHES, application number 2275.

The strength of the MRI signal depends on the length of imaging time, pulse sequence and magnet strength. In the initial stages of this study, it was found that the maximum time, a subject could comfortably sit without significant motion of the fingers was roughly 20 minutes. The high resolution (~100μm) of these images clearly displayed any motion when it occurred. Motion artifacts sharply declined with improved positioning techniques of the finger and reduced imaging times. Papillary pulses and regular breathing patterns did not seem to influence results significantly. This phenomenon results from the fact that blood flowing perpendicular to the plane of imaging transverses the section within the time it takes to complete a single pulse sequence. Thus the signal from the demagnetized protons is lost because the protons have left the imaging plane.

4.2 Subject Preparation

For the purpose of this paper, only the response of the *in vivo* fingerpad under static loads was examined. To explore the static responses under a variety of conditions, the finger was loaded with various shapes and at different depths. When someone indents or strokes an object to explore its material or surface properties, often the fingerpad will come in contact with the surface at roughly 20-40 degrees from the surface to the axis of the bone. To constrain the direction and orientation of the load, the static loads were applied at an angle of 30° and parallel to the bone axis.

4.2.1 Finger Preparation

The subject needed to remain as motionless as possible during imaging. Therefore a static finger holder was designed to immobilize the finger, while allowing loads to be applied at different depths. The device was built out of a thermoset plastic, Lexan, to maintain the homogeneity of the magnetic field and to prevent any harm to the machine or the subject from ferrous materials. Figure 4.1 demonstrates the shape and loading mechanism of the finger mount.

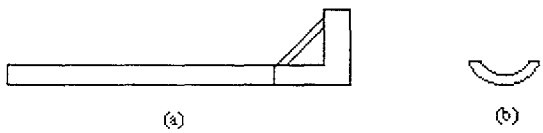

Figure 4.1: (a) Shows a side view of the finger indentor with diagonal rails which allows a load to be applied at 30 degrees. (b) Illustrates the curvature of the bottom piece on which the finger is mounted.

The imaging coil is a cylindrical tube with an internal bore diameter of 2.54 cm and 4 cm in length. The finger holder is cylindrical in shape with a flat end which helps reduce lateral and axial motions. The finger nail was attached to the probe by cyano-acrylate (superglue) as shown in Figure 4.2.

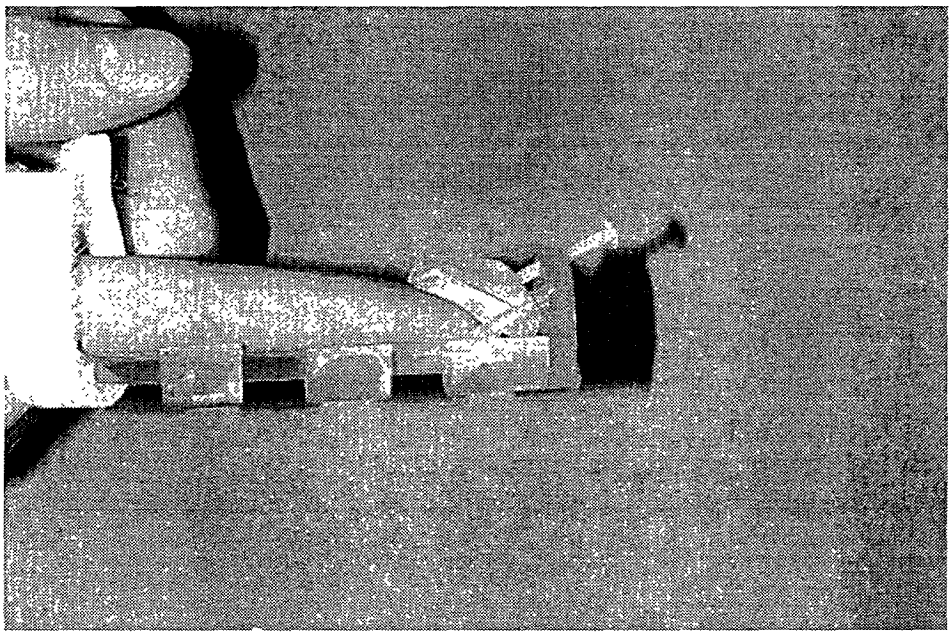

Figure 4.2: The finger is attached to a finger holder which holds the finger in full extension. The holder allows different indentors to be statically loaded to the fingerpad, with a screw for indentor depth adjustment.

The finger was indented with six different shapes at 0 mm, 1 mm and 2 mm depths by the use of a screw. All the indentors were 1 inch long. The shapes of the indentors included a line load, cylinders of $^1/_8$, ¼, ½, and 1 inch diameters and rectangular bars with widths of $^1/_{16}$ and $^1/_8$ inches. The line load was simulated by using a wedge machined to a 50μm

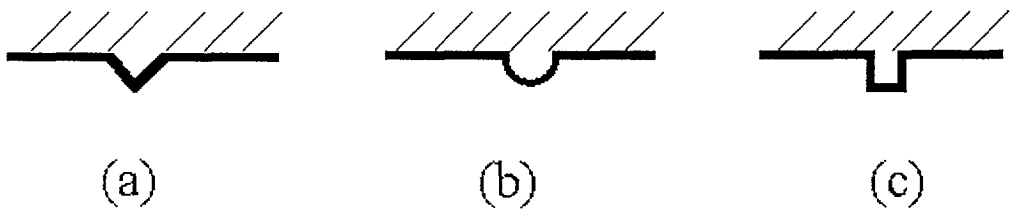

Figure 4.3: Cross section of indentors used to apply a load to the fingerpad. (a) A wedge with an edge of 50μm was used to simulate a line load. (b) Cylindrical shapes with varying diameters of $^1/_8$, ¼, ½, and 1 inch were used to simulate rounded surfaces. (c) Rectangular bars of $^1/_{16}$ and $^1/_8$ inches width were used to examine the fingerpad responses to abrupt changes in surface direction.

width edge. This 50μm edge was selected as the minimum thickness which would not cut the subject. Figure 4.3 shows the cross section of the indentors.

4.2.2 Upper Extremity Preparation

To stabilize the forearm, each subject was fitted with a customized splint fabricated from a low temperature thermoform plastic (polyform). The splint extends down the forearm and holds the wrist at 10° of extension. The splint positions the index metacarpal phalangeal joint in full extension. The splint attaches to the finger probe to prevent any flexion at the proximal and distal interphalangeal joints. Figure 4.4 illustrates the forearm splint.

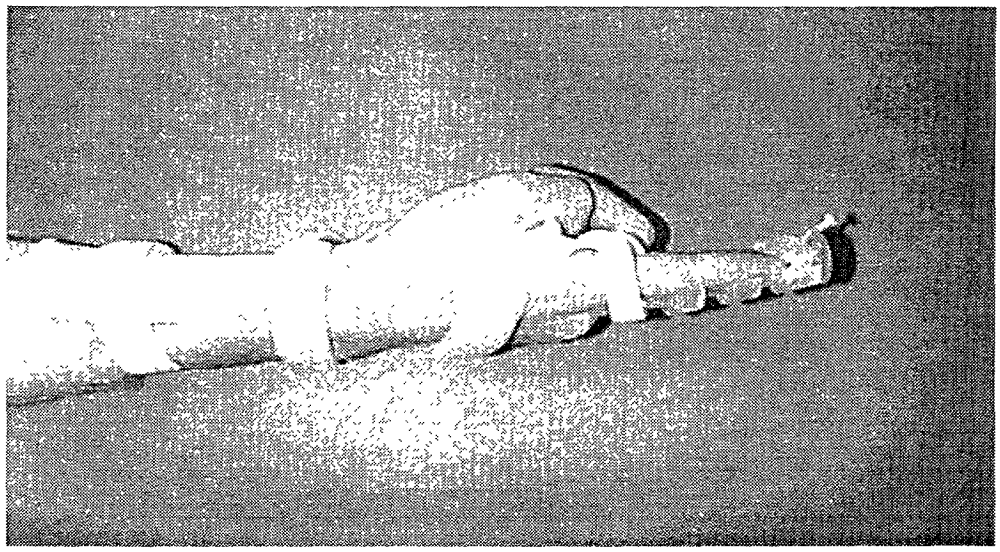

Figure4.4: A low temperature plastic splint which extends up the forearm and holds the wrist at 10° of extension and finger in full extension.

The upper extremity was positioned on a customized table which placed the arm in full elbow extension and shoulder flexion of 85-90°. The shoulder was slightly protracted so that the subject could relax the shoulder muscles on the platform. A foam V- wedge

cradled the arm to prevent lateral and rotational motions of the forearm. The subject was seated facing the magnet so that arm was directly in front of the subject (or at 90° horizontal adduction). This positioning also prevented the subject from looking around and allowed the individual to concentrate on remaining motionless.

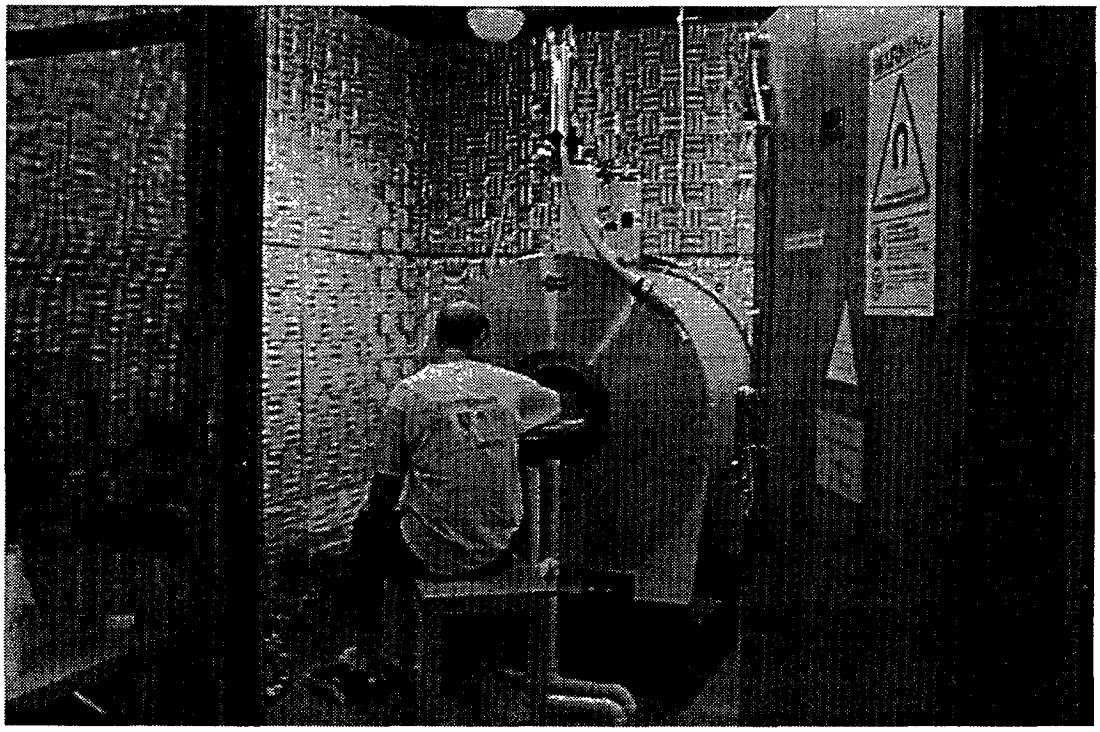

Figure 4.5: Subject setup with arm placed inside the magnet and supported on a table with a foam wedge. Subject is seated facing the magnet to decrease any distractions.

4.3 MRI Protocol

One of MRI's intrinsic strengths and distinguishing features is its ability to give high contrast and functional data for various soft tissues. The MRI signal depends on the tissue's chemical make-up and is directly related to the relaxation times T_1 and T_2. The MRI protocol can be adjusted to emphasize a desired T_1 and T_2 for a particular tissue. This makes MRI techniques ideal for differentiating the layers of the fingerpad.

In MRI, there are three interacting quantities to be considered: image acquisition time, signal to noise ratio and spatial resolution. Figure 4.6 shows the interactions between these qualities. To maximize the amount of data collected for this study, the imaging protocol was broken down into two categories, cross-sectional images and longitudinal section images.

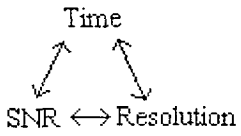

Figure 4.6: For MRI images, these qualities are directly related and improvement in one of these three is at the expense of one or both of the other two.

Cross sectional images were used to gain high resolution and tissue contrast for examining each static load for a given depth. An additional set of longitudinal section images were taken to obtain structural information of the fingerpad and to examine tissue translation along the axis of the bone.

4.4 Cross Sectional Images

4.4.1 RARE Sequence

At high resolution, to gain sufficient signal to noise ratio (SNR), the subject must be imaged for extended periods of time. The higher the resolution, the greater the time that is needed to get sufficient SNR. SNR is given by:

$$SNR \cong f(\text{intrinsic})*f(\text{extrinsic})/N \qquad (4.1)$$

where f(intrinsic) is as follows:

$$f(intrinsic) \cong (N_H*(1-e^{-(TR/T1)})*(e^{-(TE/T2)}) \qquad (4.2)$$

where N = noise level, and N_H = proton density

The TR is linked to T_1, such that only variations in TR affect the amount of T1 weighting, or signal attenuation, in an MR image. Similarly, TE is linked to T_2 and variations in the extrinsic parameter TE affect the amount of T_2 weighting in an image.

For a given combination of invariant and intrinsic parameters of TR and TE, the equation for the signal strength as a function of the remaining extrinsic parameters is given as the following:

$$f(extrinsic) \approx \Delta t \cdot \left(\sqrt{n}\right) \cdot \left(\frac{FOV_x}{\#x}\right) \cdot \left(\frac{FOV_y}{\#y}\right) \qquad (4.3)$$

where sampling bandwidth in each spatial dimension FOV_x (field of view) and FOV_y are the spatial dimensions (x = readout and y= phase encode directions), #x and #y is the resolution in a particular direction, Δt is the slice thickness, n is the number of points sampled in each spatial dimension.

These parameters have no impact on the contrast in an image, but do have several other important consequences. For example, a twofold magnification (i.e. fixed matrix size but FOV reduced by one half) reduces the SNR per voxel in the image by a factor of four. Doubling the matrix size in both the phase encoding and readout dimension for a fixed FOV, doubles the resolution, reduces the SNR by $2\sqrt{2}$ and doubles the scan time (T_s). Sampling for twice as long increases the SNR by a maximum of only $\sqrt{2}$.

The spin echo sequence is ideal for developing tissue contrast by isolating out the TR and TE out of the echo. However, the conventional spin echo sequences collect one line of image data per repetition period. The scan time for this sequence can be calculated by the following equation:

$$Time \approx TR * (total\#of\ phase\ encodings) \quad (4.5)$$

The pulse sequence is then repeated for a number of TR periods until all phase encoding are collected, which can result in long imaging times. Trials showed that subjects could not remain still for image times greater than 20 minutes and subjects performed well with images lasting approximately 10 minutes in duration.

One way to reduce the image time is to use a fast spin echo acquisition with relaxation enhancement also called the RARE technique. The basic difference between the RARE and spin echo sequence lies in the second half of the pulse sequence. The RARE sequence also utilizes a refocusing pulse for each echo. This helps reduce artifacts created by the decomposition of repeated echoes. The use of this technique reduces the total imaging time by the number of echoes, as seen by the following equation:

$$\mathbf{Time = TR * \#\ phase\ encodes * \#\ of\ averages / \#\ of\ echos} \quad \mathbf{(4.7)}$$

The SNR of the image can be enhanced by increasing the number of averages but will directly increase the total scan time. Because of the higher SNR for a set scan time, the RARE sequence was the sequence of choice. Each subject was imaged fifteen times with various loads for an average image time of 7 minutes and 50 seconds for each slice. See section 4.6 for settings used in the RARE protocol.

4.4.2 GEFI Sequence

The RARE sequence highlights the blood vessels and fat equally, making it difficult to locate blood vessels. Gradient echo techniques emphasize effective T_2 weighted structures so that tissue differentiation is minimal. This method enabled the signal intensity of fat to be minimized and the blood vessels to be highlighted. A single image was taken after each RARE sequence. These imaging times (32 seconds) were kept to a minimum since resolution was not significant and only location was needed. The settings for the GEFI sequence can be seen in section 4.6

4.5 Longitudinal Images

To obtain functional structural data of the fingertip along the axis of the bone, the same RARE sequence was utilized. The resolution of each image was 118 x 118μm in-plane with a 1mm slice thickness. The thicker slice allowed the number of averages to be decreased to 10 and the total image time to 4 mins and 15 secs per slice. Only the 1/8" wide rectangular bar was used because of the flat surface profile which decreased error from curvature from averaging over the 1mm slice thickness. These images were taken to examine tissue displacement longitudinally.

4.6 Parameters

Parameters for each sequence can be seen in the Table 4.1.

Measuring Method	Rare	Gefi
Matrix Dimension	160 x 160	160 x 160
Spectral Width (Hz)	100,000	50,000
TR	1500 msec	50.0 msec
TE	4.7 msec	5.2 msec
Total Time	7min 51sec	32 sec
Excitation Pulse Length	600msec	2000μsec
Refocusing Pulse Length	600msec	
Number of Averages	30	4
Number of Echoes	16	
RARE Factor	16	
Field of View (FOV)	2 cm * 2cm	2 cm * 2 cm
Slice Orientation	Transverse_Coronal_Left_Right	Transverse_Left_Right
Slice Thickness	0.5 mm	0.5 mm
Read Extension Factor	1	1
Phase Encoding Start	-0.92	-0.92

Figure 4.1: Listed above are the parameters used to obtain functional data for thesis project which were determined by experiment. The RARE sequence was use to capture soft tissue layers. The GEFI sequence highlighted the blood vessels and the Gradient Echo 3D provided structural data of the entire fingerpad.

These parameters were determined by multiple experiments until maximum contrast for the fingerpad was achieved.

Chapter 5

MRI Results and Anatomical Correlation

5.1 Cross-Sectional Images

5.1.1 Raw Data

Cross sectional images of the fingerpad were taken using a MRI RARE technique with the finger loaded and unloaded. As described earlier, the fingerpad was loaded with a static line load, ⅛", ¼", ½" and 1" diameter cylinders, and 1/16" and ⅛" wide rectangular bars. The voxel size for the image slices was 125 x 125 x500μm for the three subjects. Figure 5.1 contains each of the cross sections under a given load for Subject 1. At the top of each image is the location of the fingernail. The fingernail images appears black in the MRI because the nail contains very low water content. Working from the outside in, a thin light and a thicker dark ring can be seen which correlates to the epidermis and dermis, respectively. The epidermis contains significant water (H^+

protons) and thus images lighter. The dermis is composed of tightly bound water molecules which do not give much MRI signals, and hence look dark. The next inner region is the hypodermis or fat region. This area images bright since fat contains a high level of water. This region is striated with black strands which are collagen fibers that hold the fingerpad together. The last two elliptical areas are the bone and bone marrow. Bone lacks water content, but bone marrow contains high levels of water since it is highly vascular. As a result, bone will image dark and bone marrow will image the brightest. The effects of the indentors applied to the finger can be seen on the bottom half of each picture. The indentors themselves image black since they contain no water.

One disadvantage of using MRI is that each image requires a finite slice thickness. The machine averages the signal produced over this thickness to give a signal value for a particular pixel. For these experiments, the image slice is 500μm thick which causes some blurring of the image. This is owning to the fact that the finger gets wider at more proximal loci. In other words, the location of a particular tissue in one area maybe slightly displaced a few microns away for a given slice. The MRI averages all of these signals which results in blurring and making a particular tissue in a distal cross section look wider than its actual measurement. Ideally, minimizing the slice thickness would result in decreased error from averaging. However, thinner slices produce less signal, which means considerably increased scan time is necessary to gain sufficient signal-to-noise ratio.

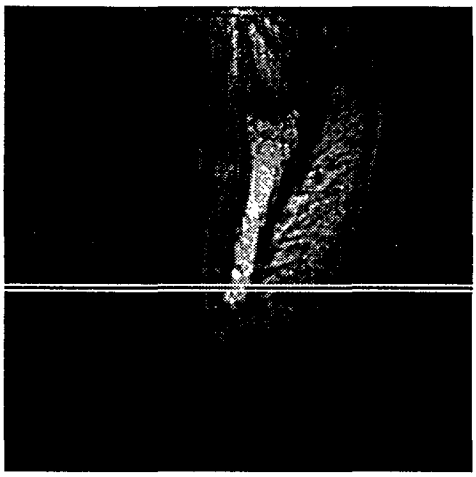

Figure 5.1.1: Longitudinal cross section of the finger pad used to locate the axial image at 2mm from the tip of the bone (white lines).

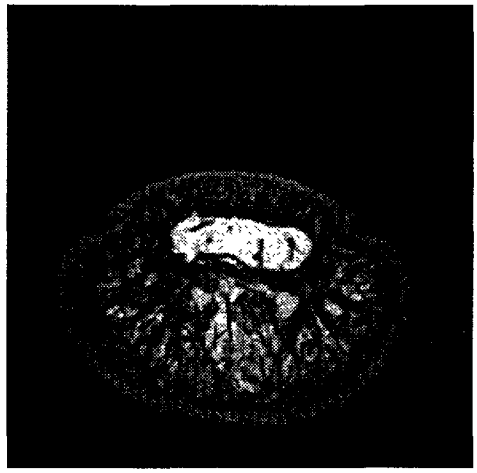

Figure 5.1.2: Axial section of the fingerpad with no load applied.

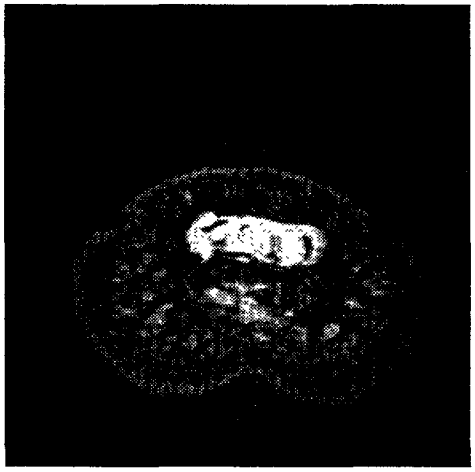

Figure 5.1.3: Fingerpad indented to 1 mm with a line load.

Figure 5.1.4: Fingerpad indented to 2 mm with a line load.

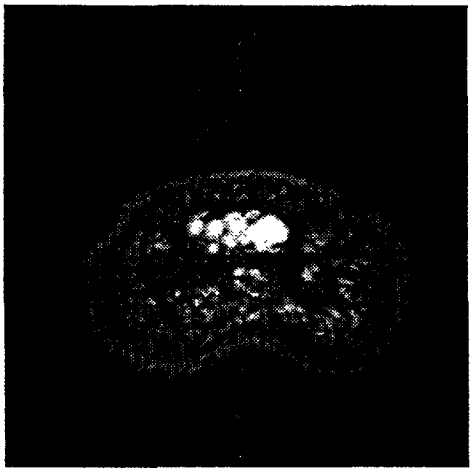

Figure 5.1.5: Fingerpad indented to 1 mm with a 1/16" wide rectangular bar.

Figure 5.1.6: Fingerpad indented to 2 mm with a 1/16" wide rectangular bar.

Figure 5.1.7: Fingerpad indented to 1mm with a 1/8" wide retangular bar.

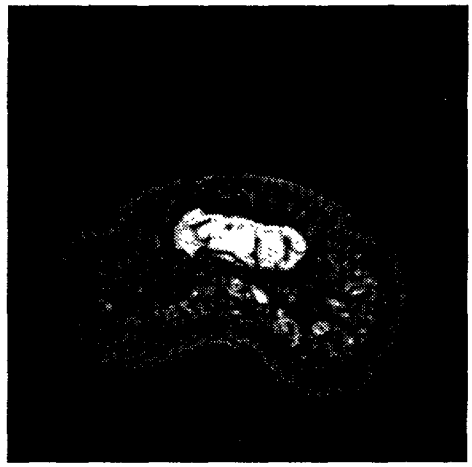

Figure 5.1.8: Fingerpad indented to 2 mm with a 1/8" wide rectangular bar.

Figure 5.1.9: Fingerpad indented to 1 mm with a 1/8" diameter cylinder.

Figure 5.1.10: Fingerpad indented to 2 mm with a 1/8" diameter cylinder.

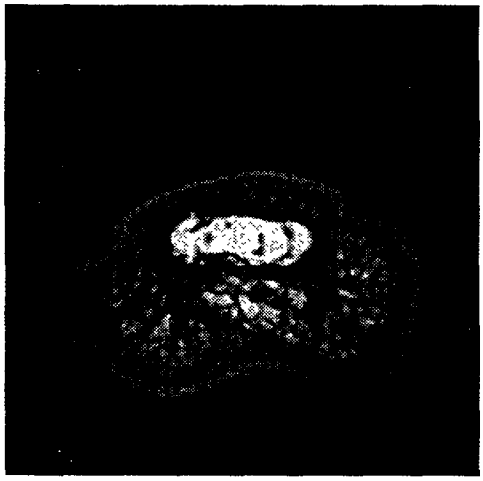

Figure 5.1.11: Fingerpad indented to 1mm with a 1/4" diameter cylinder.

Figure 5.1.12: Fingerpad indented to 2mm with a 1/4" diameter cylinder.

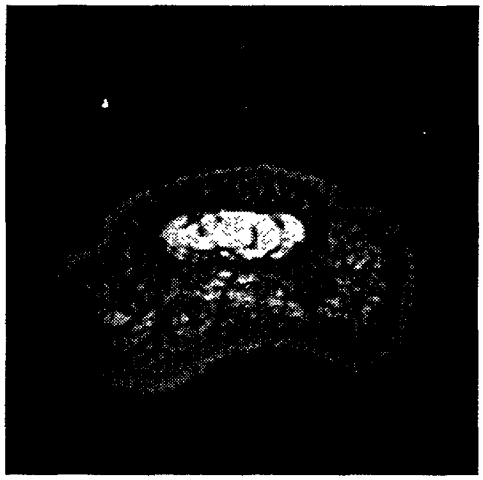

Figure 5.1.13: Fingerpad indented to 1mm with a 1/2" diameter cylinder.

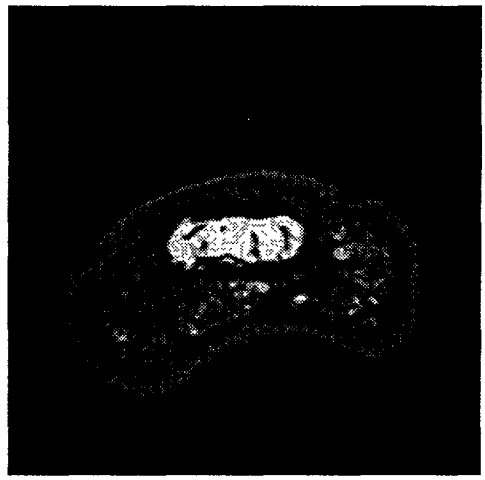

Figure 5.1.14: Fingerpad indented to 2 mm with a 1/2" diameter cylinder.

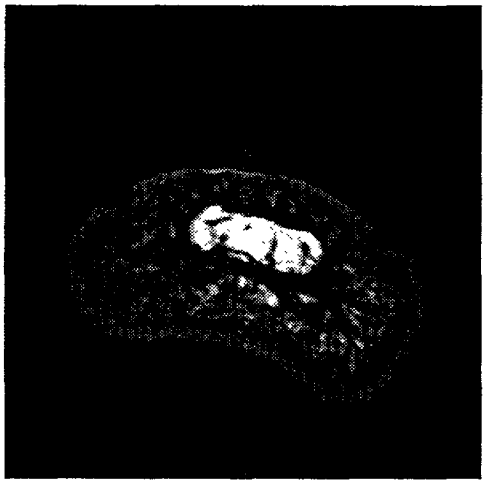

Figure 5.1.15: Fingerpad indented to 1 mm with a 1" diameter cylinder.

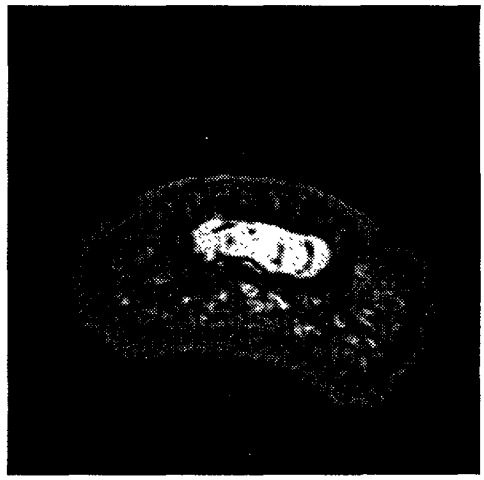

Figure 5.1.16: Fingerpad indented to 2 mm with a 1" diameter cylinder.

Figure 5.1: Cross sectional images located 2mm proximal to the tip of the bone of the human fingerpad. The resolution of each image is 125 x 125 x500μm with a field of view of 2.0 cm. Each image indicates the type of load and depth of indentation.

Data for the other two subjects is located in Appendices A and B.

5.1.2 Errors

The spatial resolution of the images limits the level of detail obtained from each image. Long image times and motion artifacts limited the resolutions to less than 125μm for cross -sectional images. The high magnetic field strength of 4.7T helped reduce error due to chemical shift. In these studies, a band width of 100KHz resulted in a chemical shift of 1.2 pixels at the fat-water border. The average signal to noise ratio was 10:1, which

allowed for sufficient resolution for image segmentation and visualization. Errors resulting for magnetic field non-linearities were reduced using post processing techniques which are discussed in Chapter 6.

5.2 Subject Variability

Variability between subjects was easily seen. No two individuals are alike and the fingerpad is no exception. Depending on age, gender, race, health and other factors, tissue thickness, size and location can vary. In the pulp, the amount of fat, fibrous tissue and dermal thickness change as the cross-sections approach the distal tip.

To minimize the number of variables in the study, the location of the image slice was constrained to be 1mm proximal to the end of the bone. In this study, four subjects were imaged to obtain fingertip cross sections. Figure 5.2 shows the variability in the tissues of the fingerpad structures among the subjects. Size of the fingerpad varied for a given field of view, with one subject having a significantly smaller finger. It can be seen that the shape of the nailbed changed from subject to subject and the amount of fat for this given region also changed. One subject was dropped from the study due to the lack of adipose tissue that resulted in poor imaging of the area of study.

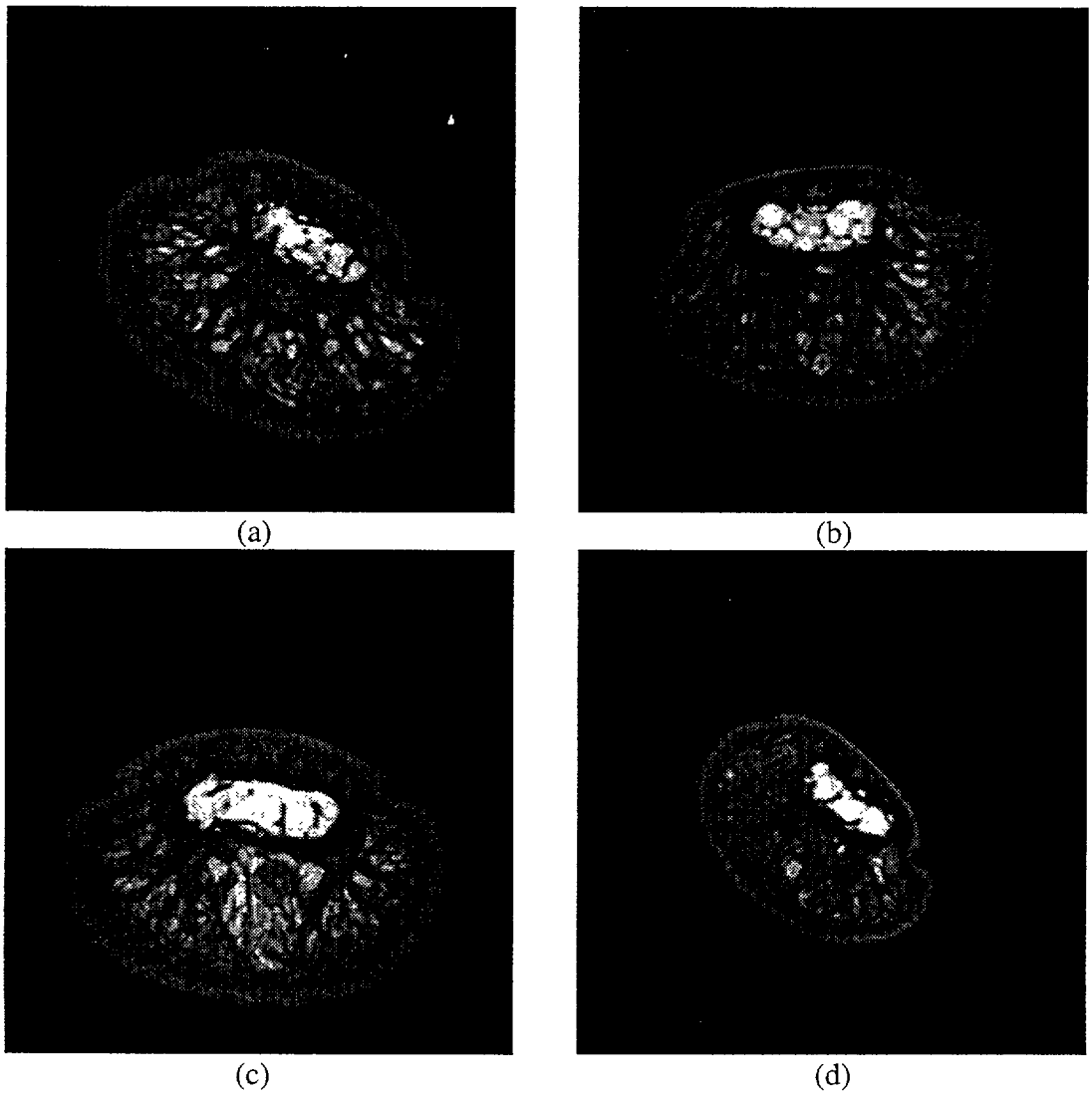

Figure 5.2: Fingertip cross sections of four individuals were taken with a FOV of 2 cm by 2 cm and a resolution of 125 x 125 x500μm. The image was located at 1mm proximal to the end of the bone. The amount of adipose tissue (fat) which images as bright white in each individual is a good indicator of the variability from subject to subject. Additionally, the shape of the nailbed varied from subject to subject.

5.3 MRI Skin Images

One objective of this study was to analyze the deformation of the fingerpad at the dermal layers which means identifying each layer. The first question to ask is whether or not all of the layers are being captured, especially since finger ridges could not be seen. To determine if the outer edge was being captured, the finger was imaged in a coating of

Agrose, a gelatin based substance with high water content. The image illustrated a thin outer border that was not being captured by the imaging done without agrose. The question is what is creating that dark ring, either an air boundary, oil film or a skin layer. To eliminate the possibility of an air boundary, the finger was then re-imaged under water which is less viscous than Agrose and not likely to leave a significant air boundary layer. Figure 5.4 shows that once again a dark ring lies on the outer edge of the finger. The

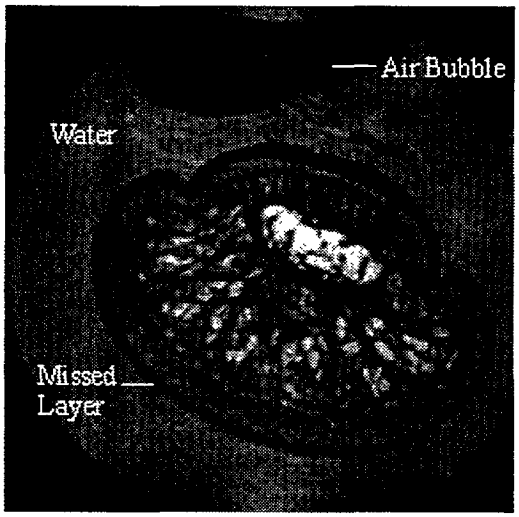

Figure 5.4: Cross section of the finger submerged in water. A dark ring appears around the image indicating an additional outer layer that is missing in the previous pictures.

average thickness of this layer is 350μm which corresponds to the average thicness of the stratum corneum (Tubiana, 1981).

To verify that this ring is a part of the skin layers, a FLASE (fast large spin-echo sequence) sequence with a short TR of 80μs and a TE of 10.3μs was tried to capture the signal of the outer layer (Song, et al, 1997). Studies done by Song, et al, showed that the stratum corneum could be detected using a surface coil and this protocol. These studies indicated that portions of the dark circle were captured with this protocol, but the signal to noise ratio was poor. Further studies are needed with a surface coil to improve the

signal-to-noise ratio to compare our initial results for the skin layers with results obtained by Song, et al.

In addition, the finger was compressed with a flat piece of glass to allow a larger image slice (increases SNR) to be taken without effects of finger curvature affectively the results. The finger was coated with a layer of Agrose before being compressed to aid in locating the edge of the plate. The sequence used was a RARE protocol with a TR of 1500μs and a TE of 4.7μs. Figure 5.5 displays one image which shows an axial view of the finger compressed and the other image is a repeated image with the skin coated in Agrose.

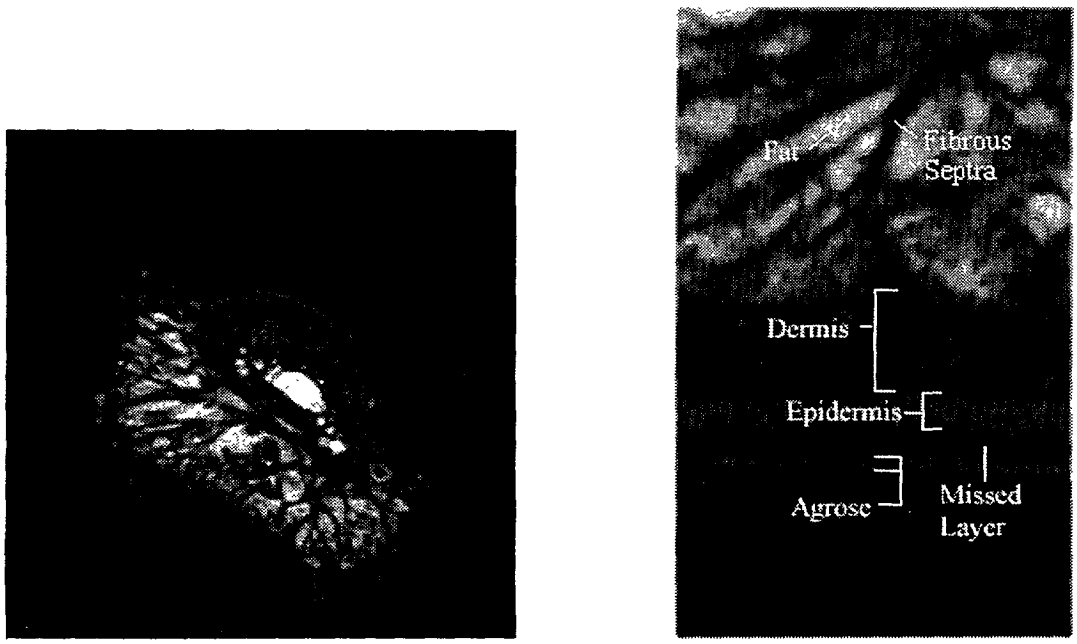

Figure 5.5: Images of the outer edge of the fingerpad which has been compressed by a flat piece of glass (left image). A RARE sequence with TR=1500ms and TE=4.7ms with a resolution of 125μm in-plane resolution. The right image shows is a zoomed area at the center of the glass plate with the finger coated in Agrose.

These studies with both Agrose and water establish the existence of a single outer layer that is not captured by the RARE sequence used. The possibility of a that this layer is a

thin film or water boundary is minimal since it could be reproduced with the use of water. Additionally, the resolution of the images limits the noticeable effects of any artifact below 125μm.

The average thickness of the next inner layer (light layer) is 400-500μm. The sum of these two layers corresponds to the thickness of the epidermis in the fingerpad, which is about runs 700 to 900μm in thick (Lockhart, et al, 1965, Lanir, 1987). Since the stratum corneum consists mostly of dead cells and almost no moisture, it is likely that the outer dark layer is the stratum corneum. The other layers of the epidermis serve as protective layers and are rich in water, which explains the lighter color.

The next inner layer found in human skin is the dermis which consists of tightly bound water. This means that the tissue will not emit a strong MRI signals and will appear black on the image, (See section 5.4 for further discussion of anatomical correlation). This is consistent with what is seen in the images. See Figure 5.5 b for the labeling of various layers.

5.5 Anatomical Correlation

The fingertip consists of the nail, a distal phalanx (bone), adipose tissue (fat), fibrous septae, and dermal (skin) layers. The skin layers can be broken down into the dermis and epidermis with a sublayer of the epidermis called the stratum corneum (finger ridges are a a part of this layer). In the fingerpad, the epidermis is about 700 to 900μm thick and has multiple functions. The larger portion of the epidermis called the horny stratum corneum

consists of keratinized cells which are continually cast away (Lockhart, et al, 1965, Lanir, 1987). The thicker dermis adjoins the epidermis at the dermoepidermal junction consisting of ridges which correspond to the papillary ridges of the fingerprint (Tubiana,1987). The dermis is made up of a combination of collagen, elastin and reticular fibers (Tubiana,1987). Because of the pixel resolution (order of 100 microns) obtain on the MRI images, further subdivision of the dermal layers becomes irrelevant for our purpose. Figure 5.6 displays the layers of the skin.

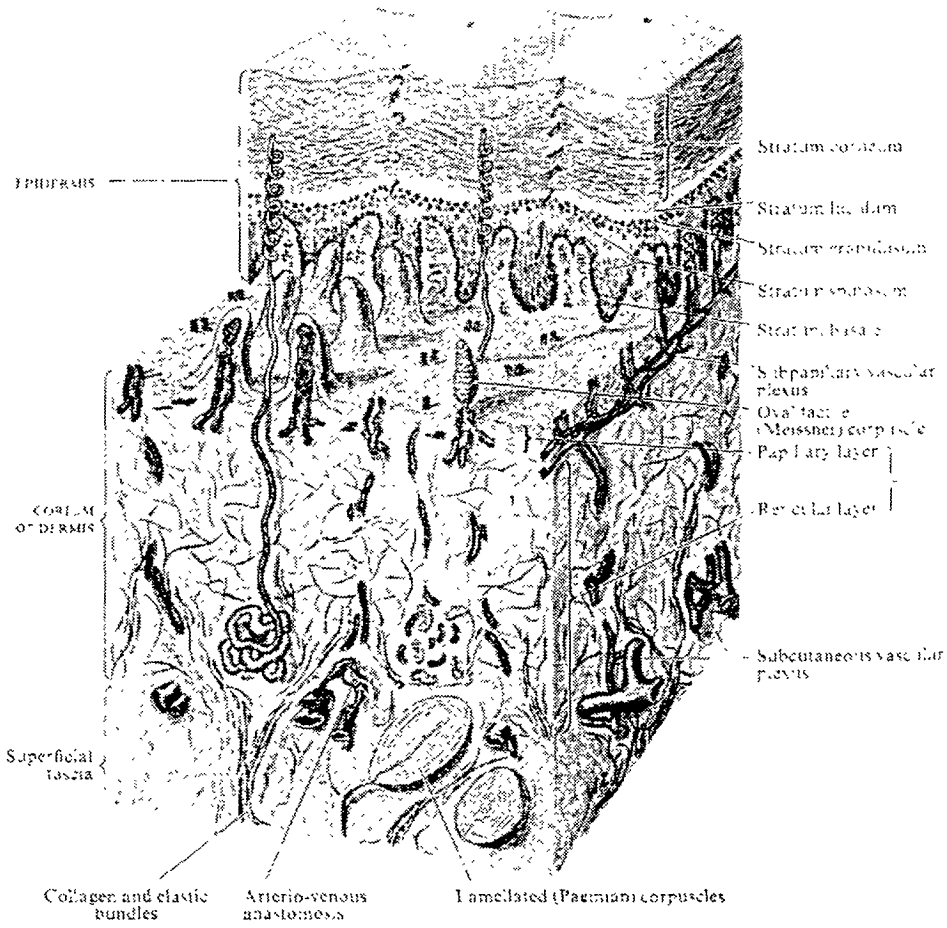

Figure 5.6: Cross section of the human skin with structural layers identified. The thicknesses of the epidermis and dermis depend on the location within the body with a thickness ratio of roughly 3:4, respectively. Adapted from Anatomy of the Human Body by Lockhart, et al, 1965.

The hypodermis makes up the bulk of the fingerpad by connecting the skin to the bone. It includes adipose cells (fat) divided by fibrous septae which help anchor the skin to prevent gliding and large displacements of tissue.

In order to accurately label fingerpad structures, histological cross sections of both finger tips and skin were used. A cross section through the distal phalanx, as shown in Figure 5.7 (a), identifies the various structures. Image (b) of Figure 5.7 is a typical MRI cross section of the distal phalanx located at 1mm from the tip of the bone.

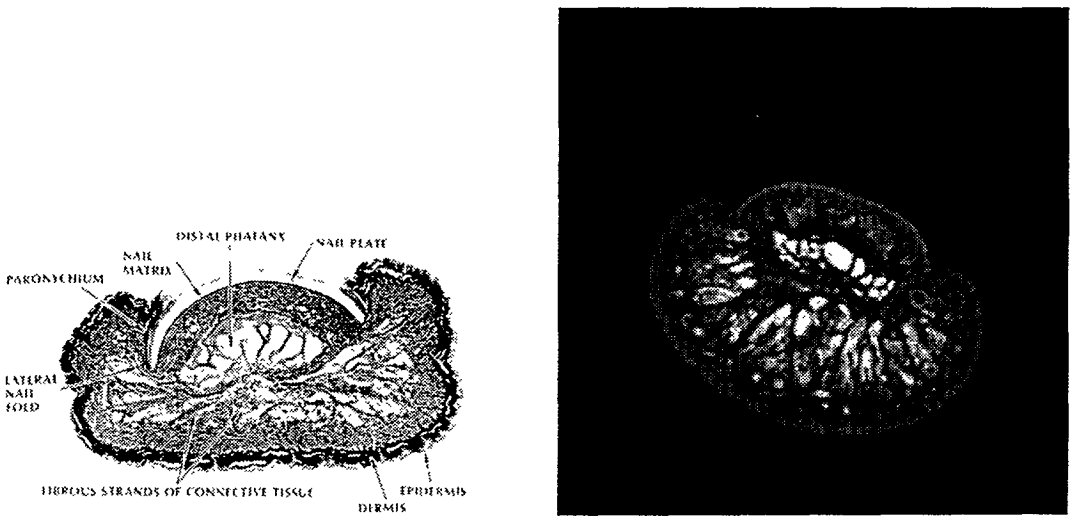

Figure 5.7: (a) Histological cross section of the distal phalanx; (b) MRI cross section of the distal phalanx

Using all the methods described above, each structure in the cross sectional images was identified as shown in Figure 5.8. Further verification of the dermal layers were used to positively label each section.

The skin layers and borders were less clear on the MRI image because of the missed outer layer. Also, it was unclear if skin contrast was lost in order to gain overall contrast. The

studies on the skin as described in section 5.3 show that a thin layer was not highlighted by the RARE sequence. Direct measurements from the MRI images indicates this layer is approximately 350μm which correlates with the typical thickness of the stratum

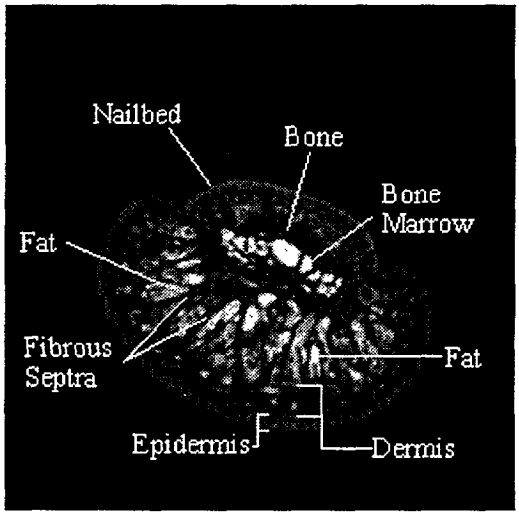

Figure 5.8: Anatomically correlated MRI image of a cross section of the distal phalanx located 1mm proximal to the end of the bone. Not that the stratum corneum portion of the epidermis is missing.

corneum. The loss of contrast by this layer maybe due to the lack of moisture (H^+ protons) to the atmosphere. The dermis composed of mostly collagen images dark to the MRI image because of a shorten T2 from tightly bounded water (Song, et al, 1997). The dark region located on each MRI image is estimated to range in size from 350μm. The outer light ring seen on the MRI image ranges in size from 300-500μm. This lighter ring and the missed outer ring sum to ~650-850μm which is consistent with data found for the thickness values of the epidermis (Tubiana, 1981).

5.4 Cadaver Studies

A series of cadaver studies were completed to help relate MRI structures to anatomical structures. The cadaver finger was fixed to the finger mount and imaged using the RARE.

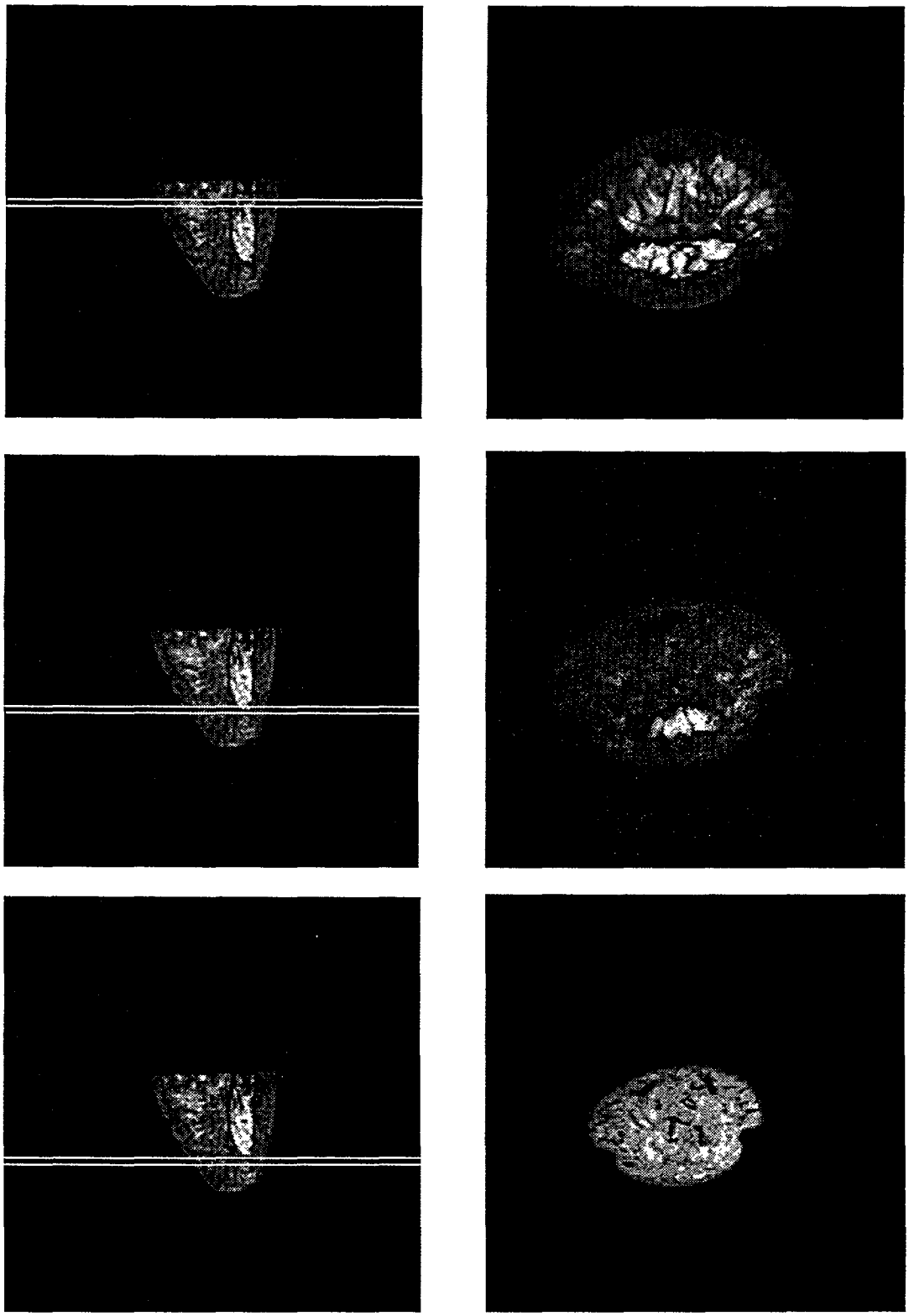

Figure 5.9: Several cross sections on a cadaver finger were sampled. The left hand images illustrate slice location along the longitudinal axis of the finger and the right hand images are the cross sectional images.

sequence. The in plane resolution was 78x78x500μm for an in plane field of view of 2cm. Since the finger could be mounted and remains stationary, high resolution images were obtained over 25 minute periods.

Additionally, the end of the cadaver finger at the location of the amputation was imaged with a video microscopy system to capture tissue features. Figure 5.10 shows one of the images obtained under approximately 2X magnification.

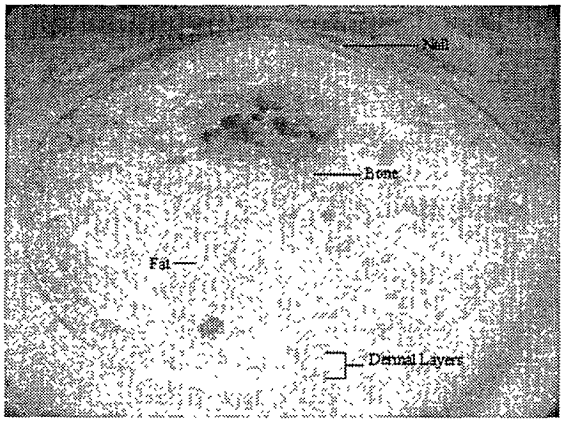

Figure5.10: Axial Cross section through a cadaver fingertip with anatomical structures identified.

The MRI results for the cadaver finger showed that the contrast among the skin layers was not sufficient. This maybe a result of change in the differential proteins post-mortum and due to the embalming solution. The video microscopy image illustrated the two separate layers of the skin (epidermis and dermis) along with fascia and adipose tissue that anchors the skin to the distal phalanx. Figure 5.11 shows an enlarged area near the skin in which the change in protein and collagen structure allows for visible differentiation of the skin layers.

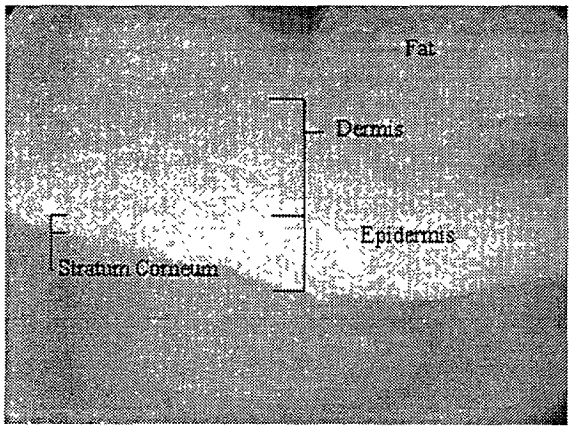

Figure 5.11: Close up of the skin region of a cadaver finger.

Tissue identification was done with methods discussed in section 5.4.

Chapter 6

Image Processing

6.1 Introduction

When a fingertip is loaded with a shape, the tissue responds by deformation, accommodation and resistance. To analyze and interpret these biomechanical behaviors, segmentation and quantification of anatomic structures is essential. Investigating tissue behavior requires tasks such as registration, quantitative analysis, labeling and displacement tracking of anatomical structures in the original image to be reduced to a compact, geometric representation of their shape.

To extract information from the image, a method of edge detection is needed to isolate tissue structures. This gives data which can be used to measure tissue displacement and location under load. An image can be segmented by several different techniques such as

manual methods, thresholding, automatic edge finding techniques, connectivity and homomorphic operations. Each method contains its own advantages and disadvantages. For this project, an automatic edge finding technique along with image processing was used in a Matlab program to isolate portions of a image. See Appendix B for the full program source code.

6.2 Image Enhancement

Image enhancement refers to image processing that makes an image more appropriate for inspection by a human observer or automatic analysis by a digital computer. Image enhancement allows for specific aspects of the image, such as edges, to be emphasized. Image enhancement techniques vary widely depending on the type of images and the nature of the application.

6.2.1 Histogram Modification

This process changes the distribution of image brightness to enhance or minimize features such as contours or noise. A histogram represents the number of pixels verses a given intensity. The histogram of an image gives information regarding the use of the range of intensity and can be adjusted to enhance details.

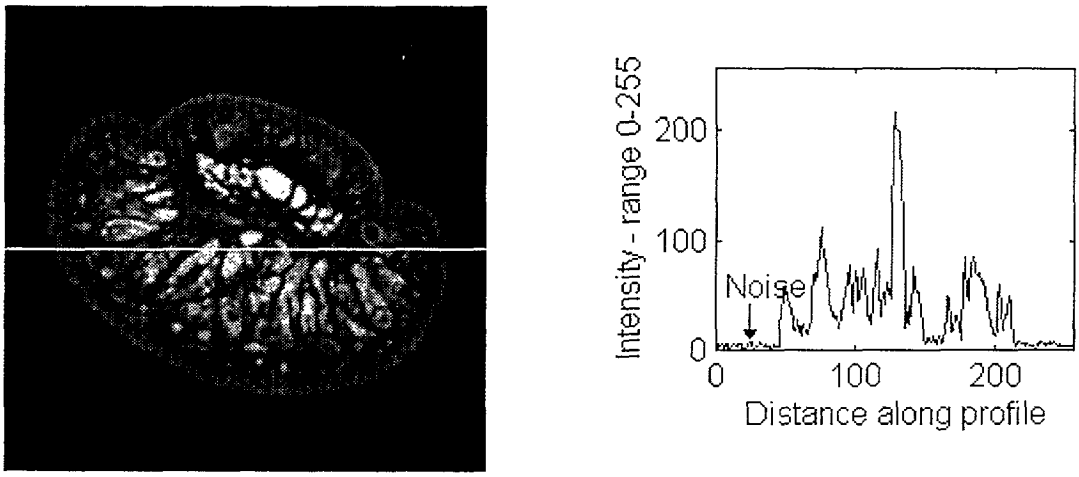

Figure 6.1: Image on the left is a cross section of the fingertip 3.2mm proximal from the end of the bone. The plot on the right presents a histogram of the image located at the white line. The noise level can be removed by simple thresholding technique of setting all values below 6 to zero. This eliminates the background noise but maintains the magnitude of the remaining signal.

For these MRI images, histogram modification was used to minimize background noise and minimizing quantization errors. Assuming no signal exists in the areas around the finger, a histogram of the image reveals the level of the background noise of a image. Using a simple thresholding technique, the noise was removed from each image prior to edge detection. Additionally, the program mapped the maximum and minimum intensity values to a range of 0-255 in order to use the entire intensity range.

6.6.2 Image Sharpening and Softening

The application of simple linear filters is another method to enhance images. Define the image to be a signal $x[n_1,n_2]$ which can be decomposed into low and high frequencies,

$$x[n_1,n_2]= x_L[n_1,n_2]+ x_H[n_1,n_2]$$

where $x_L[n_1,n_2]$ represents the low frequency components of the image, while $x_H[n_1,n_2]$ represents the higher frequencies. Overall, $x_L[n_1,n_2]$ is usually associated with the smooth variations and $x_H[n_1,n_2]$ with the local contrast and actual details of the image.

Linear filters can alter the relative contributions of $x_L[n_1,n_2]$ and $x_H[n_1,n_2]$. A low pass filter decreases the contribution of $x_H[n_1,n_2]$ which results in softening of the image making the image appear hazy or blurred. A filter which increases the relative contribution of $x_H[n_1,n_2]$ is a sharpening filter and emphasizes the edges and makes an image appear sharper.

The nature of the magnetic field used to capture a MRI image creates nonuniform intensities. These effects were minimized by placing the image in the "sweet" spot of the magnet where the field lines are approximately linear. These effects also can be minimized through filtering.

The effects of varying illumination can be seen in the histogram of the image. The finger can be assumed to be symmetric around the sagittal axis of the bone and therefore, the histogram should be symmetric. In these particular MRI images, a high pass filter was used to decrease the effects of nonuniform intensity which presented as low frequency components. Figure 6.2 displays the nonuniformity of intensity and the effects of the high pass filtering.

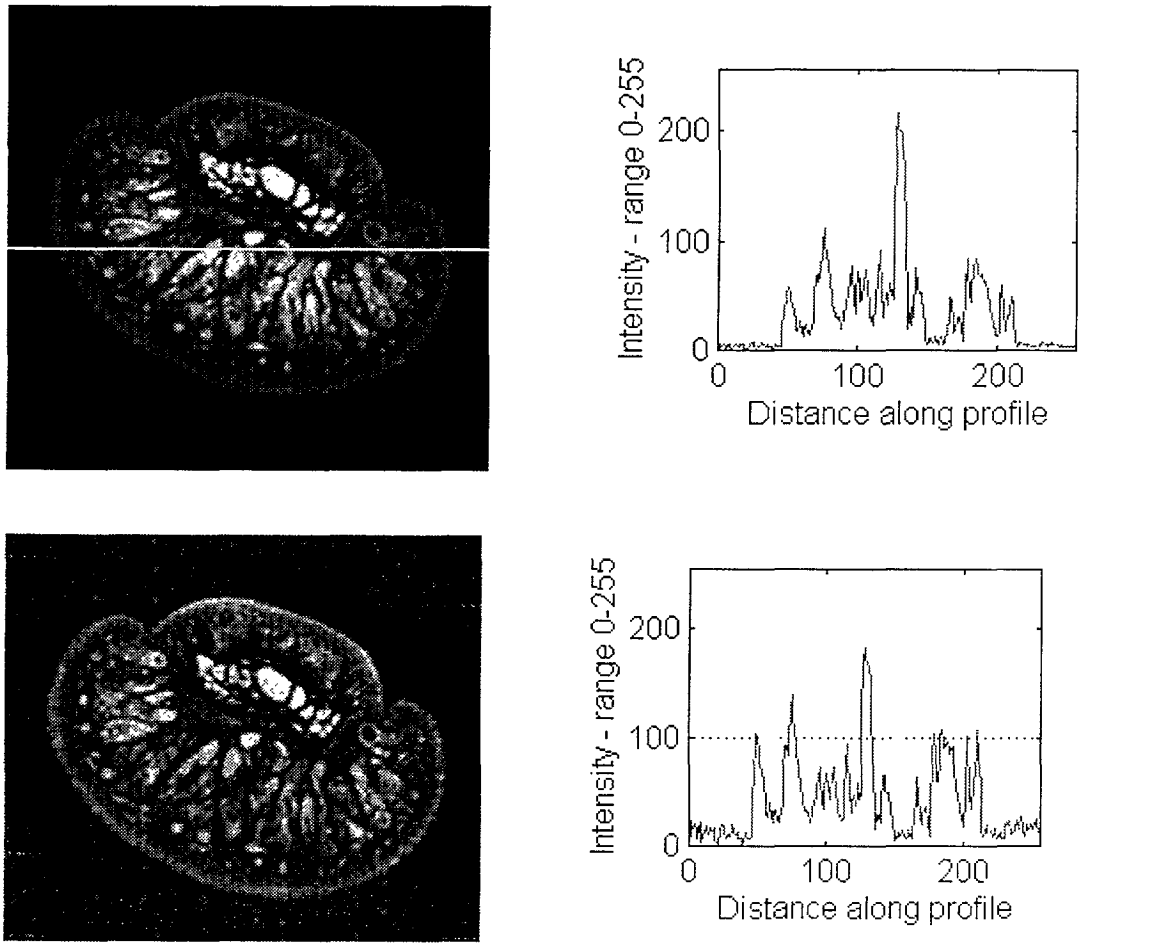

Figure 6.2: The upper left and right pictures demonstrates the intensity variation across the image. The image is most intense in the center portion along the vertical axis of the image with decreasing intensity away from the center. The lower two images demonstrate the image corrected for intensity variations across the magnetic field. The histogram illustrates increased symmetry in intensity values on both sides of the image.

6.2.3 Median Filtering

MRI images can contain significant amounts of noise from random sources. This salt and pepper noise was removed using a nonlinear filter. The filter used was a median filter which removes the spurious noise by sliding a 3 by 3 kernel over each pixel. The filter determines the median of the 3 by 3 neighborhood and replaces the center pixel by that intensity value. The following figure demonstrates the effects of the median filter.

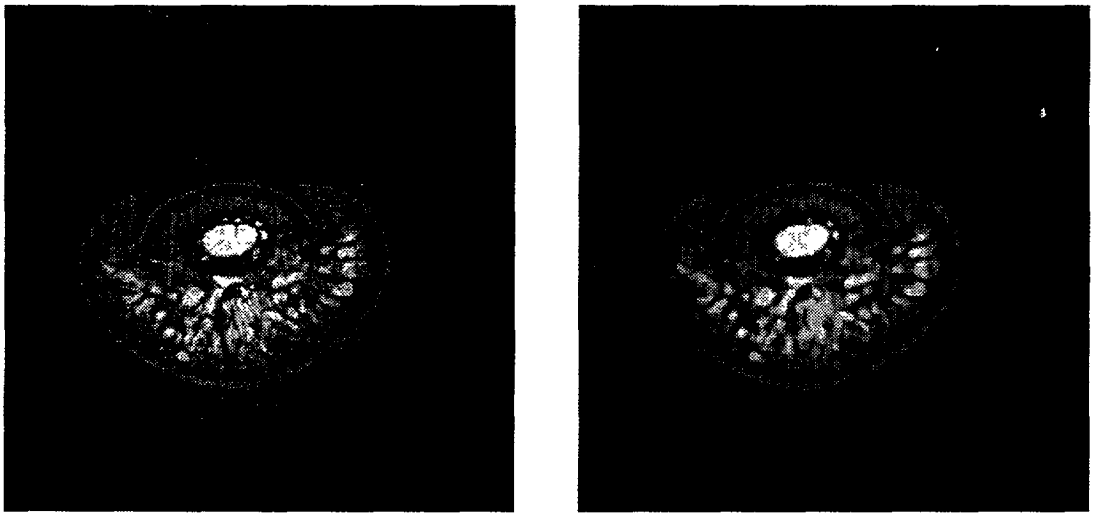

Figure6.3: The left image is the unfiltered image. The right image filtered with a median filter which softens the image by removing salt and pepper noise.

6.3 Edge Detection

One method for segmenting different edges involves the use of active contour models or "snakes". A snake is an energy-minimizing, controlled continuity spline which attracts to lines and edges by external constraint forces and image forces (Kass, 1987). This model simulates an elastic type rubberband (contour) which dynamically conforms to object shapes in response to internal forces, external image forces and user-provided constraints. The snake results in a free form geometric shape which outlines a particular region or tissue.

The application of active contour models to extract regions of interest is however, not without limitations. The models were designed as interactive models and are sensitive to their initial conditions. Consequently, they must be placed close to the preferred shape to guarantee good performance. The internal energy constraints of the models can limit their geometric flexibility and prevent a model from representing sharp curves or shapes

with significant protrusions. Furthermore, the topology of the structure of interest must be known in advance since classical snake models are parametric and are incapable of topological transformations without additional algorithms (McInerney, et.al., 1996).

The model used for these experiments consisted of a set of nodes interconnected by springs and thin plates. The position of the snake can be parameterized by $\mathbf{v}(s)=(x(s),y(s))$ and the energy functional as

$$E^{*}_{snake} = \int_{0}^{1} (E_{\text{int}}(\vec{v}(s)) + E_{image}(\vec{v}(s)) + E_{con}(\vec{v}(s)))ds$$

where E_{int} represents the internal spline energy, E_{image} represents image forces and E_{con} gives rise to the external constraint forces.[Kass,et al, 1988] See Appendix C for program source code and Appendix D for mathematical derivation of the snake.

In this project, the fingertip cross-section was broken down into five regions: bone marrow, compact bone, fat and skin layers. The initial shape of the snake is that of an ellipse with the dimensions of the shape being dependent on tissue location and size. Figure 6.4 illustrates the motion of an active contour. The of path of the snake from the initial ellipse to the outer edges can be seen by the dotted lines.

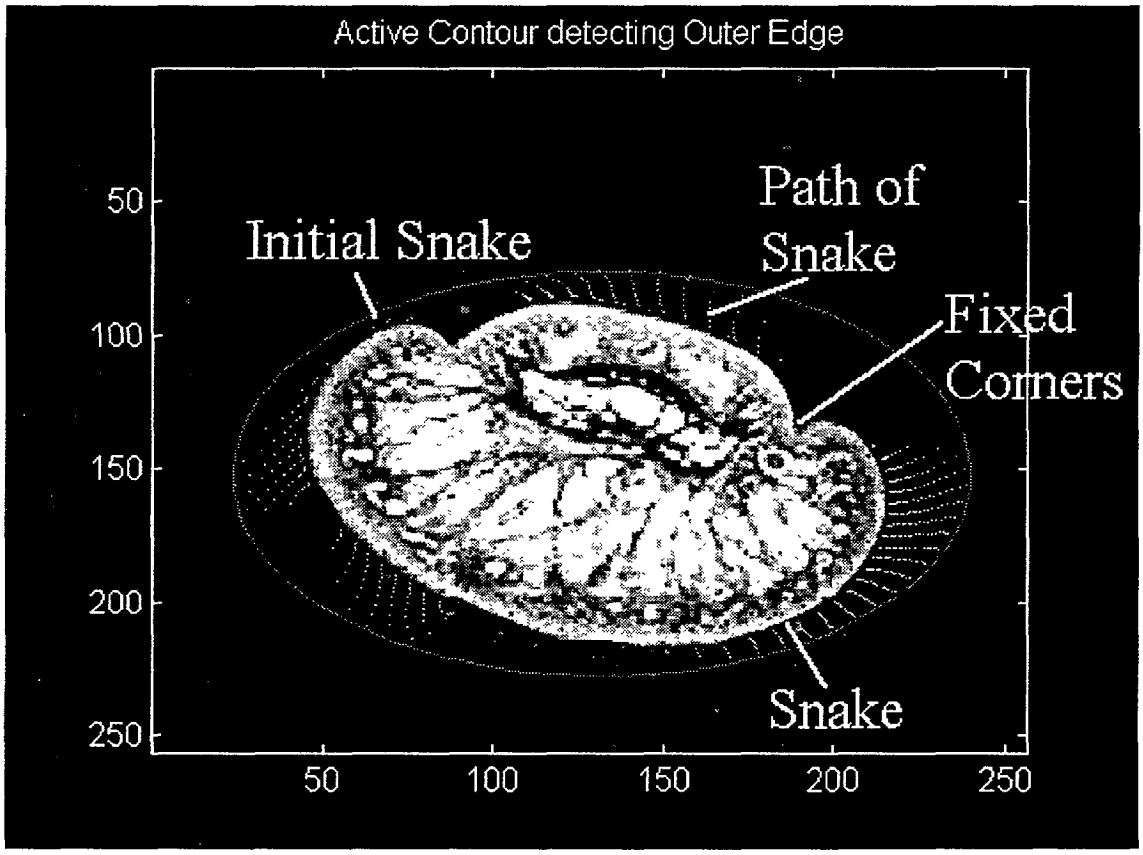

Figure 6.4: The outer ellipse is the initial starting point of the snake. The closer the initial position to the final position, the more accurate the snake is in locating the edge. The path of this snake can be seen by the dotted lines and finally the snake converges on the outer edge. The nail bed edges had to be fixed by user input in order for the snake to find these edges.

It was found that for the dramatic changes in direction around the nail bed, the snake had to be anchored in several spots for the snake to converge completely on the image. Figure 6.5 shows how the snake was unable to adapt to the rapid changes in directions along the edges near the nail bed. These anchor points were located by the user with the mouse. This technique was also used with the middle layers where the edge location was less defined.

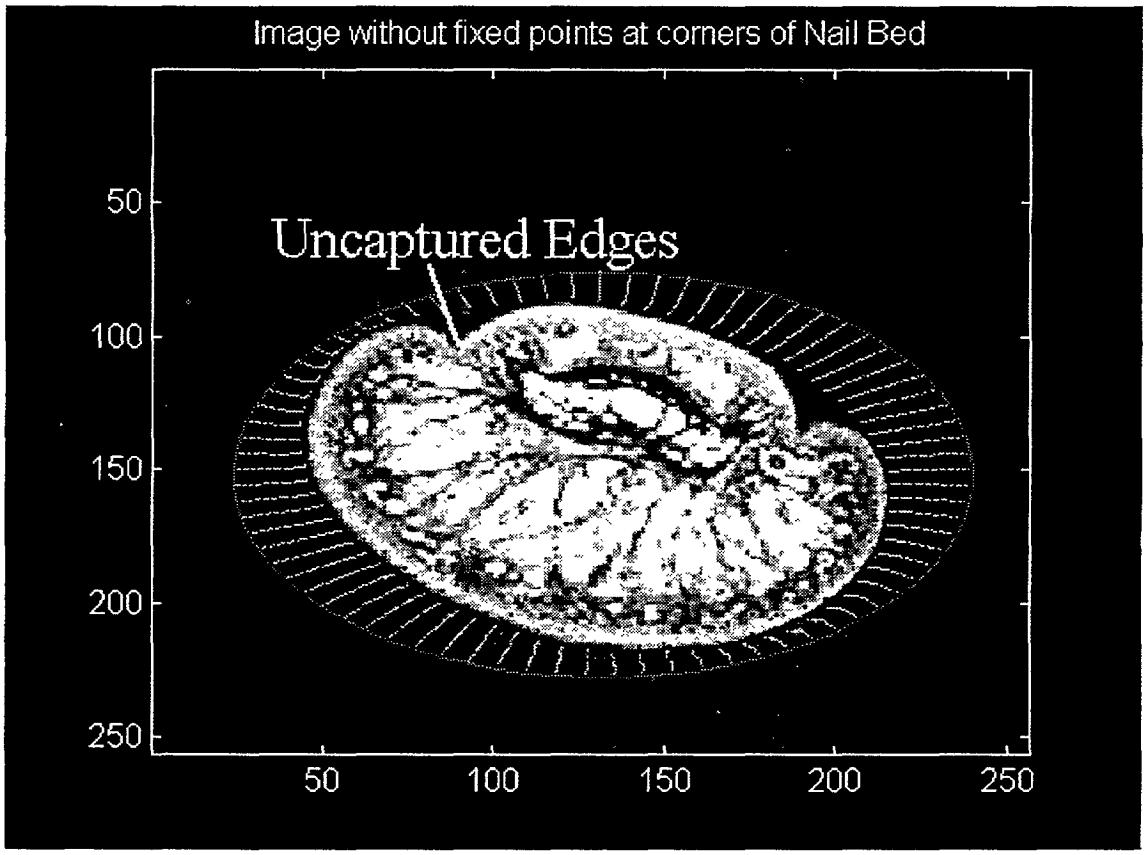

Figure 6.5: Snake locating the edge without any influence from mouse inputs. If the snake is adjusted so that the parameters are made loose enough to conform to the edges of the nailbed, the snake will not snugly conform to the other edges. By fixing the points along the nail creases, the trade off between flexibility and rigidity could be made to find the other edges.

Changing the starting parameters of the snake allowed the edges of all five regions to be located, as seen in figure 6.6.

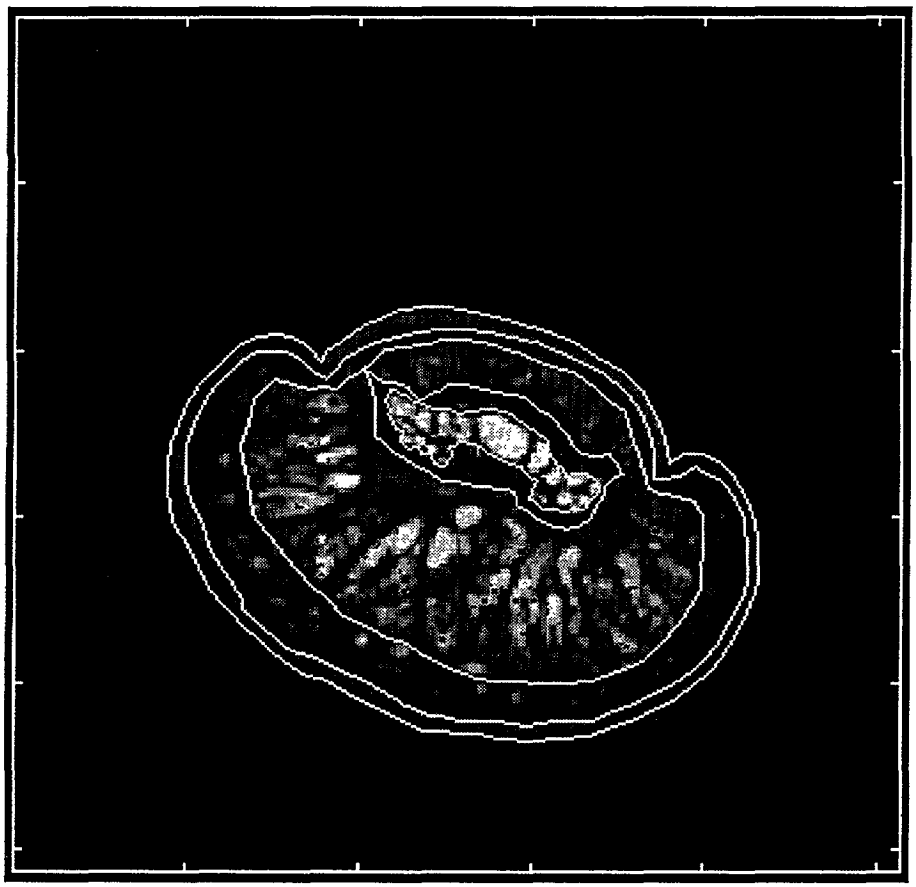

Figure 6.6: The above image shows the five tissue layers segmented by the use of "snakes"

6.4 Image Registration

To analyze the biomechanical behavior of the fingerpad, the edge profiles of the deformed tissues need to be compared to the undeformed tissues. The method used for this project was superposition where the tissue profiles were laid on top of each other to examine biomechanical behaviors. In order to obtain accurate measurements, the images need to be taken in the exact same location each time. As described earlier, the image slice was obtained 1mm from the tip of the compact bone. The error in the placement of this slice was $\pm$ 100μm.

To position the finger profiles one on top of the other, Adobe Photoshop was used with masking techniques to overlay images and edge profiles. The blood vessels, nail bed and bone acted as fixed points to define the plane, rotation and location of each image. Figure 6.7 shows two separate images of the undeformed and deformed finger which were then superimposed to form the third image.

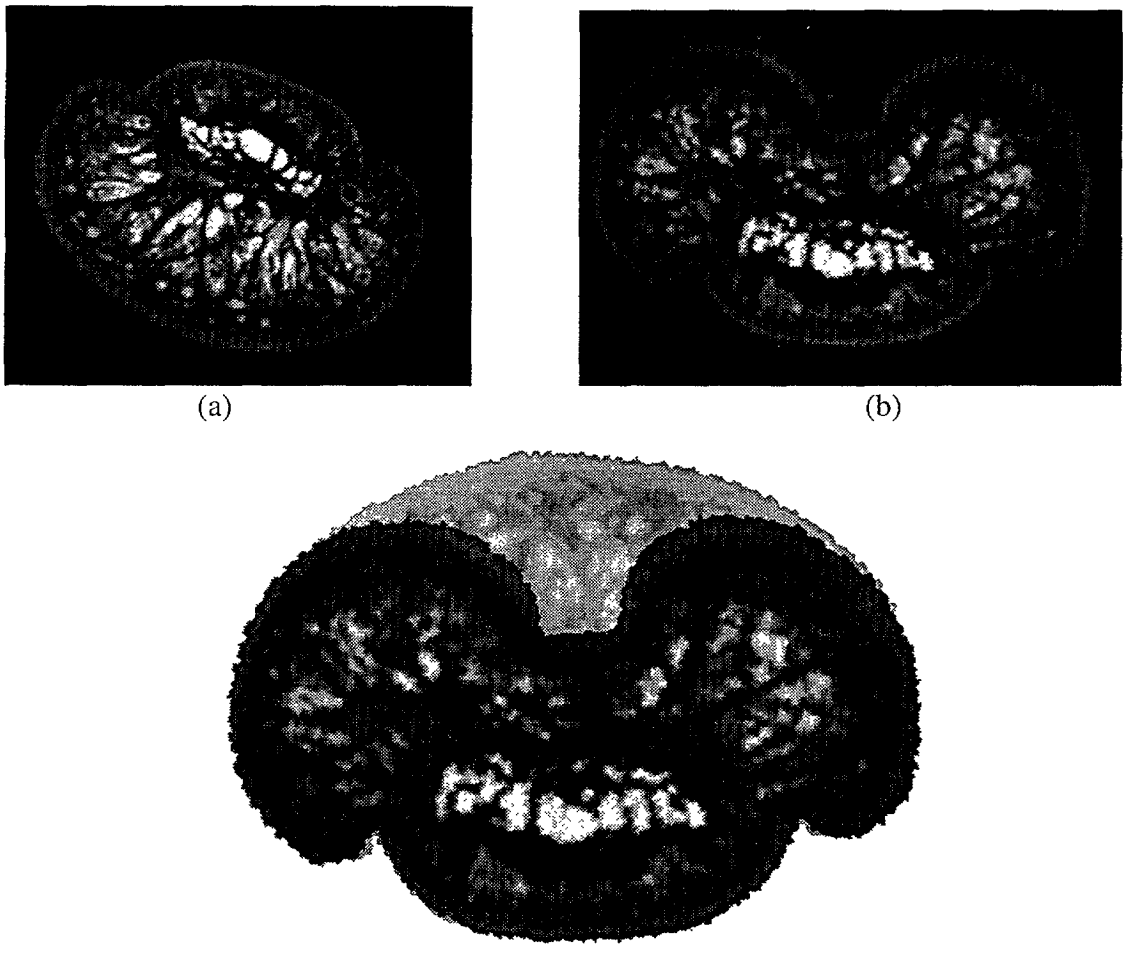

(a) (b)

(c)

Figure 6.7: Image B is superimposed onto image A, in order to view biomechanical behavior of the fingerpad. The images were registered by matching bone and nailbed landmarks.

The images had to be translated, rotated and scaled to the same dimensions in order to view results of the static loading. This was also done with just the snake contours which can be seen in the next chapter.

Chapter 7

Biomechanical Results

7.1 Edge Profiles

To model the behavior of the *in vivo* fingerpad tissues under load, direct measurements of stress, strain, deformation, and compressibility are needed. Presently, direct measurements of stress and strain are not possible. One way to gain information on deformation and compressibility is by analyzing tissue boundary profiles in the images obtained by MRI. The deformation behavior of the tissue at the surface and at deeper layers can provide guidance on how the fingerpad processes data and functions.

7.1.1 Functional Images

Superimposition of the finger images before and after loading allow for the examination of how the tissue deforms and to determine the direction of displacement. Figure 7.1

illustrates the fingerpad loaded with a line load at 1 and 2mm depths of indentation. It can be seen that tissue appears to displace downwards in the center, since very little of it displaces laterally, as indicated by relatively little bulging of tissues on the side. This

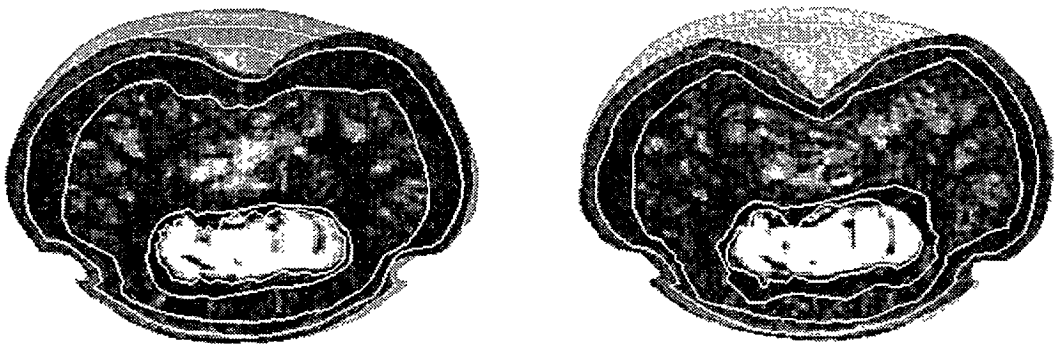

(a) (b)

Figure 7.1: (a) This image is a superposition of the undeformed fingerpad and the fingerpad loaded with a line load at 1mm indentation. Note the minimal expansion of the loaded finger in the lateral direction. (b) This image is a superposition of the undeformed fingerpad and the fingerpad loaded with a line load at 2mm indentation. At the point of load there is considerable compression of the tissue with minimal lateral expansion.

would imply that the tissue is either compressing or is being displaced along the longitudinal axis of the bone (refer to section 7.4).

To obtain the displacement field over the fingerpad cross section, attempts were made to use the fibrous septae as indicators of tissue displacement. However, these studies proved to have significant variability from section to section that it was not a feasible method. This was a result of both changes in location of fibrous septae over small regions and errors resulting from slice relocation when removing the finger from the magnet to change indentors. These relocation errors proved to be on the order of 200-500μm. Additionally, the image is averaged over the thickness of the slice which was 500μm.

Blood vessel images were also taken to use in locating tissue displacement. Problems arose in consistently obtaining equal number of blood vessels on each image and in identifying their location before and after indentation. The problems appear to be caused by pulse rate, motion artifacts and difficulties with the MRI machine and imaging pulse sequence. Figure 7.2 illustrates the blood vessels found for no load and line load at 1mm

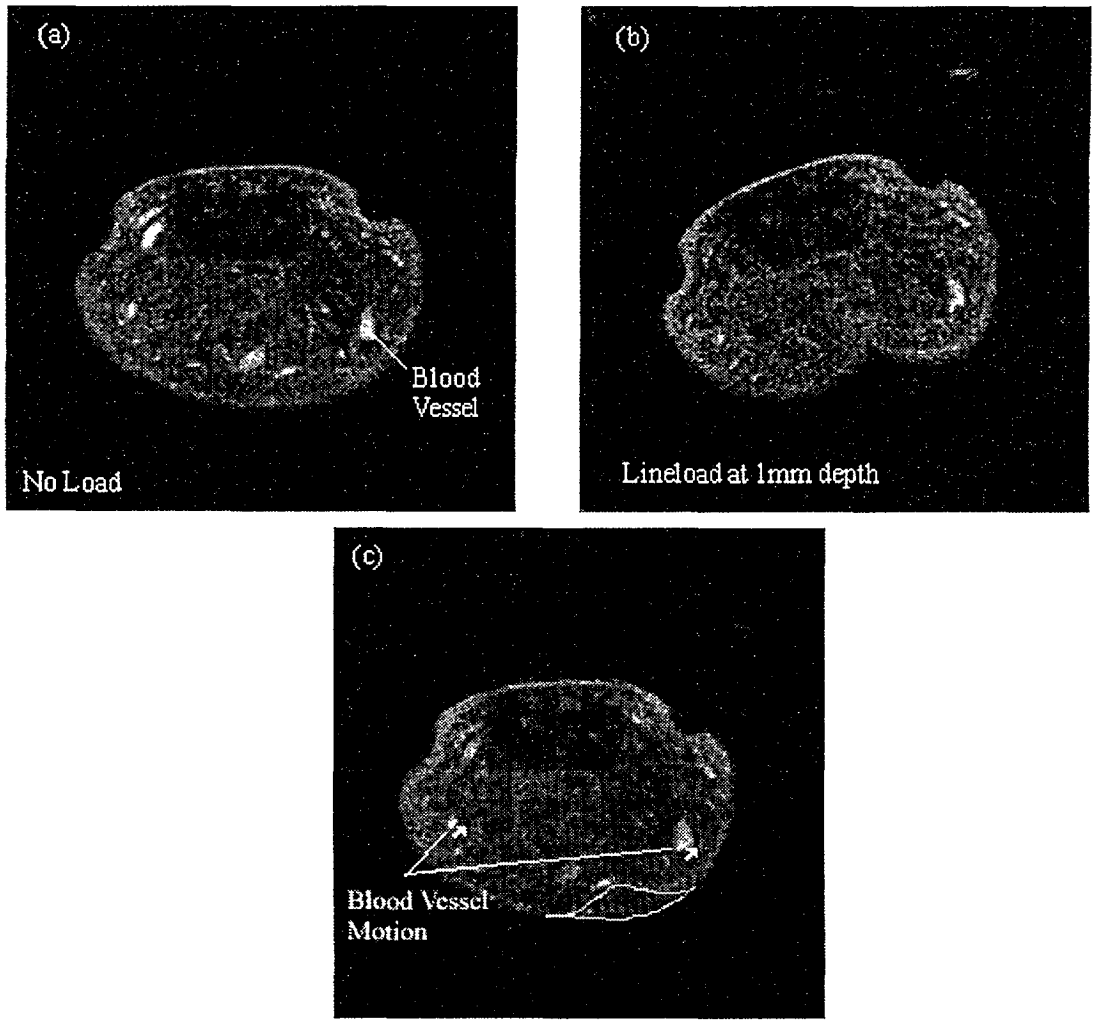

Figure 7.2: (a) Blood vessels captured using a GEFI protocol with a TR=50.0ms and a TE=5.2ms for the unloaded fingertip seen in Figure 7.1. (b) Blood vessels imaged using the same protocol for the fingerpad loaded with the line load at 1mm. This image has fewer highlighted blood vessels (c) Two images superimposed to examine the direction of displacement, which corresponds to the offset in direction of application of the line load.

depth. The third image shows the two images superimposed and the suggested direction of motion. Results from these studies proved to be inconclusive because of the reasons just described.

7.1.2 Tissue Differentiation

To better understand tissue deformation as a function of indentation depth and load shape, the boundaries of tissue layers were extracted using active contours as described in Chapter 6. This segmentation enabled visualization of deformation and gave a method to obtain measurements of areas, tissue layer profiles and displacements. Figure 7.3 demonstrates the segmentation of the unloaded finger and shows two images superimposed on each other.

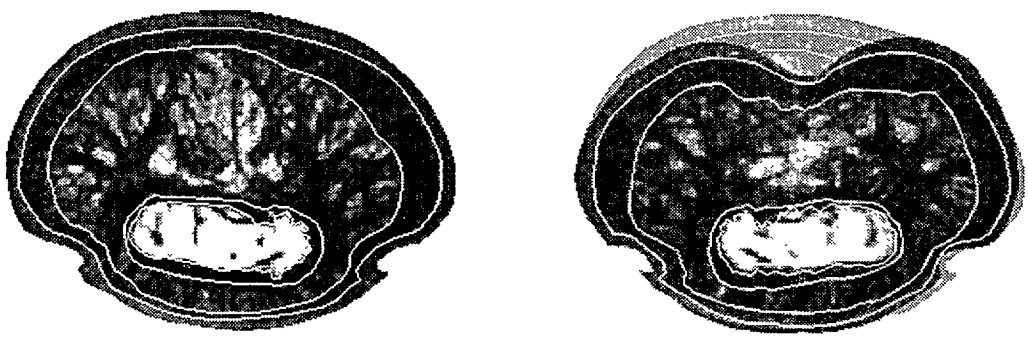

(a) (b)

Figure 7.3: (a) An axial cross section of the fingerpad with five tissue layers segmented. (b) This image shows the segmented undeformed finger superimposed with the finger with a line load at 1mm depth.

Each cross section taken for the finger of a subject was segmented and the results can be found in Figure 7.4. Segmentation data for the other two subjects can be located in Appendix E and F.

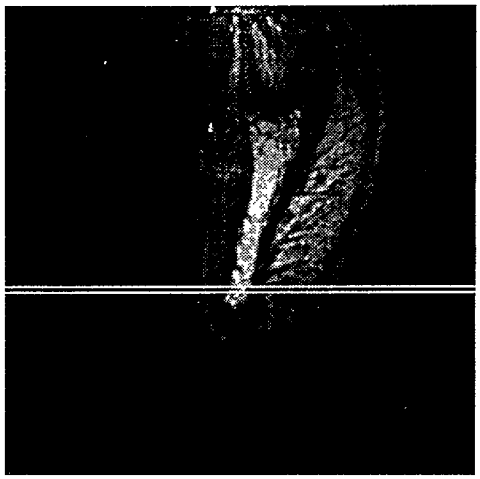

Figure 7.4.1: Longitudinal cross section of the finger pad used to locate axial image at 1mm from the tip of the bone (white lines).

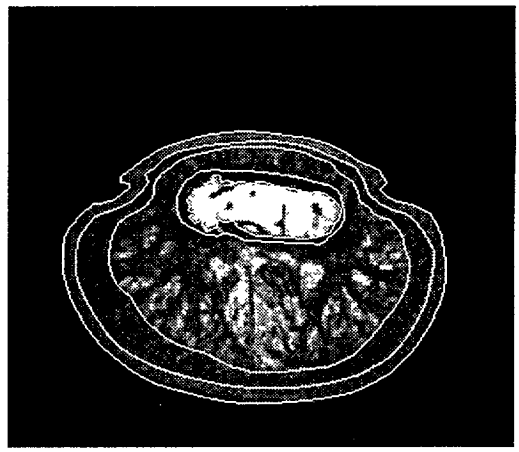

Figure 7.4.2: Axial section of the fingerpad with no load applied

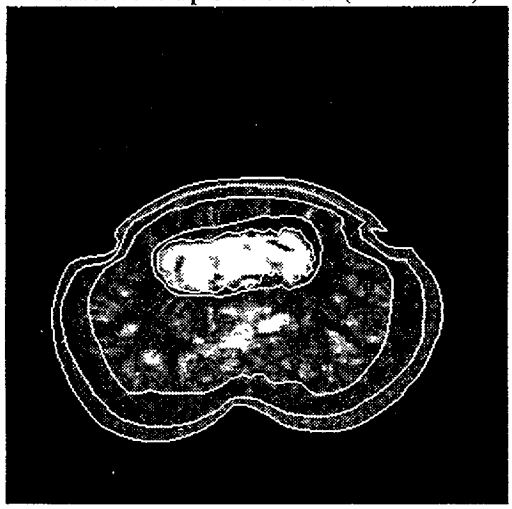

Figure 7.4.3: Fingerpad indented to 1 mm with a line load.

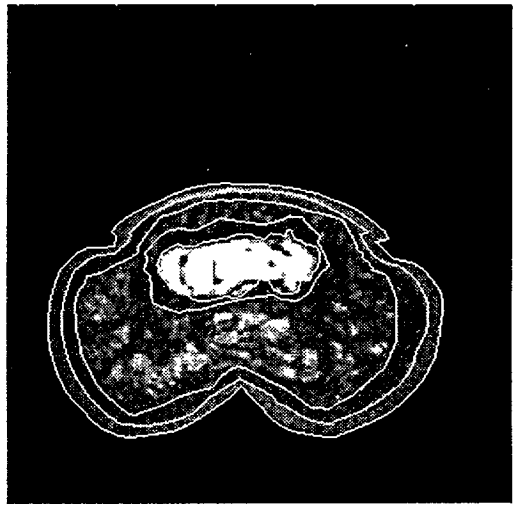

Figure 7.4.4: Fingerpad indented to 2 mm with a line load.

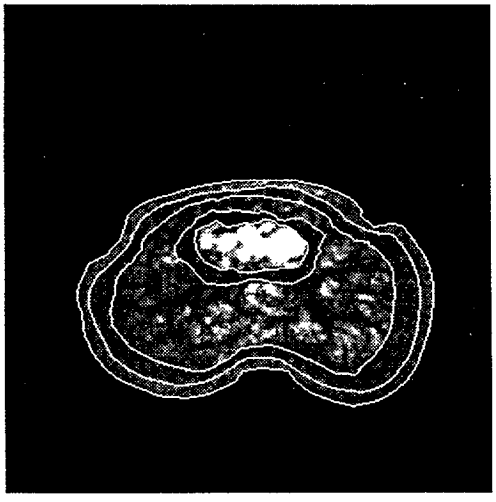

Figure 7.4.5: Fingerpad indented to 1 mm with a 1/16" wide rectangular bar.

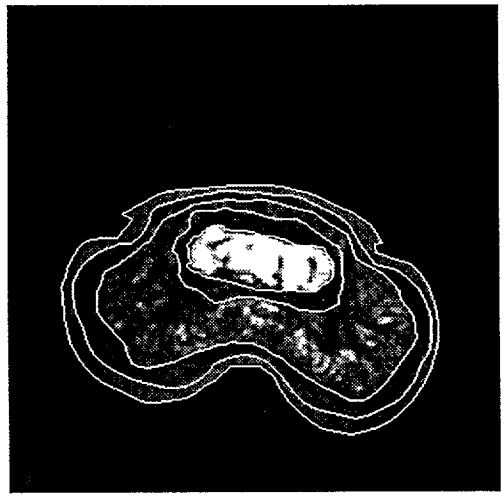

Figure 7.4.6: Fingerpad indented to 2 mm with a 1/16" wide rectangular bar.

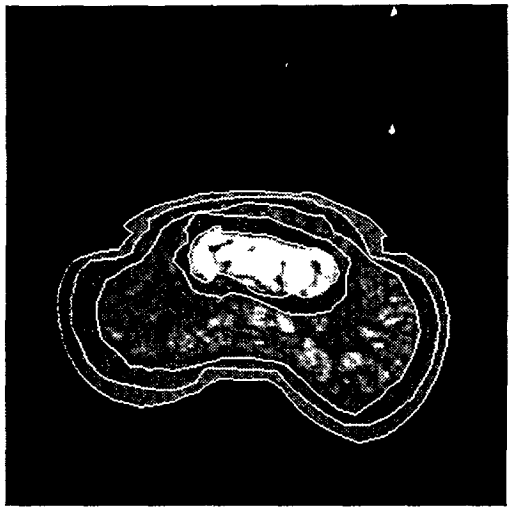

Figure 7.4.7: Fingerpad indented to 1mm with a 1/8" wide rectangular bar.

Figure 7.4.8: Fingerpad indented to 2 mm with a 1/8" wide rectangular bar.

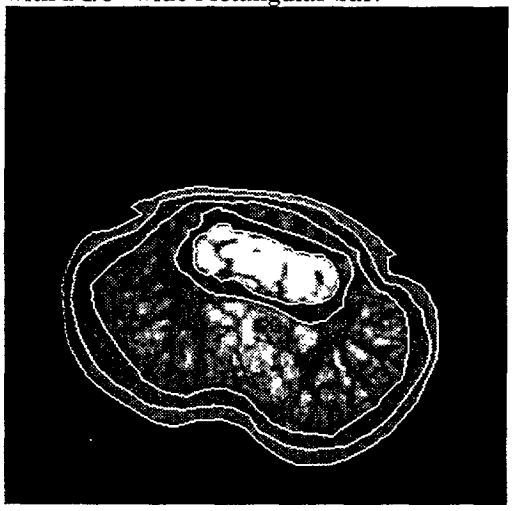

Figure 7.4.9: Fingerpad indented to 1 mm with a 1/8" diameter cylinder.

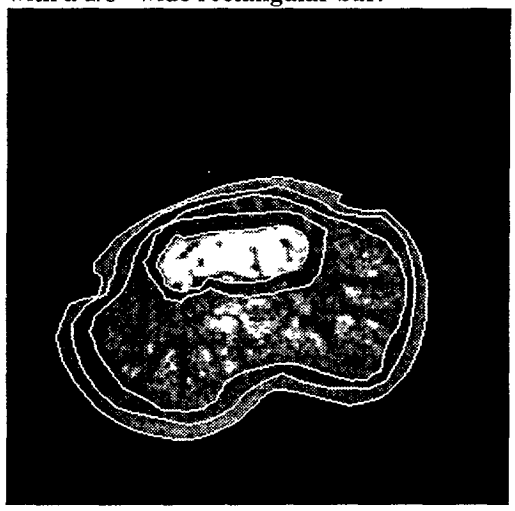

Figure 7.4.10: Fingerpad indented to 2 mm with a 1/8" diameter cylinder.

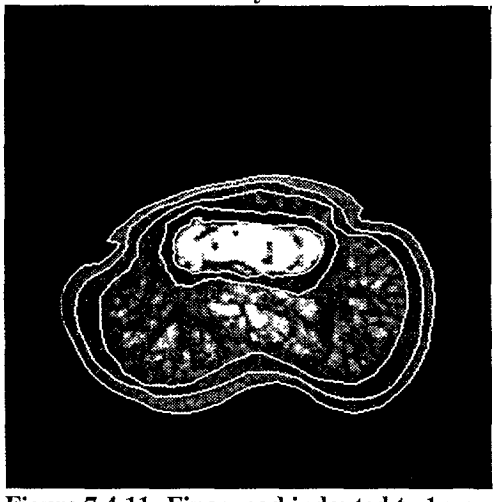

Figure 7.4.11: Fingerpad indented to 1mm with a 1/4" diameter cylinder.

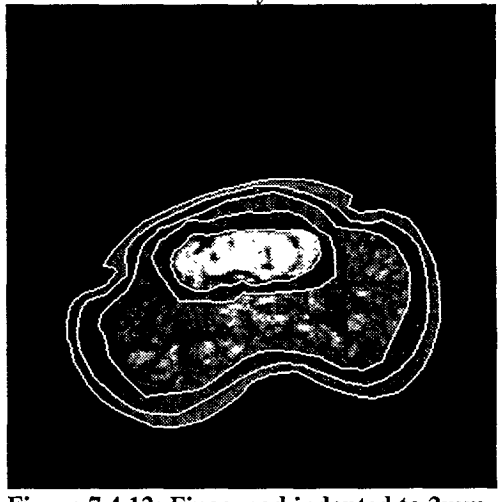

Figure 7.4.12: Fingerpad indented to 2mm with a 1/4" diameter cylinder.

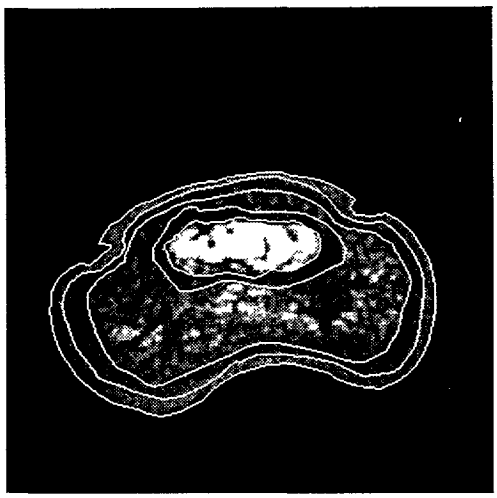

Figure 7.4.13: Fingerpad indented to 1mm with a 1/2" diameter cylinder.

Figure 7.4.14: Fingerpad indented to 2 mm with a 1/2" diameter cylinder.

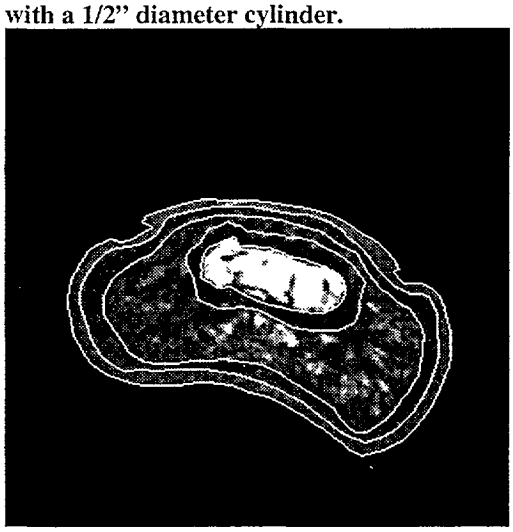

Figure 7.4.15: Fingerpad indented to 1 mm with a 1" diameter cylinder.

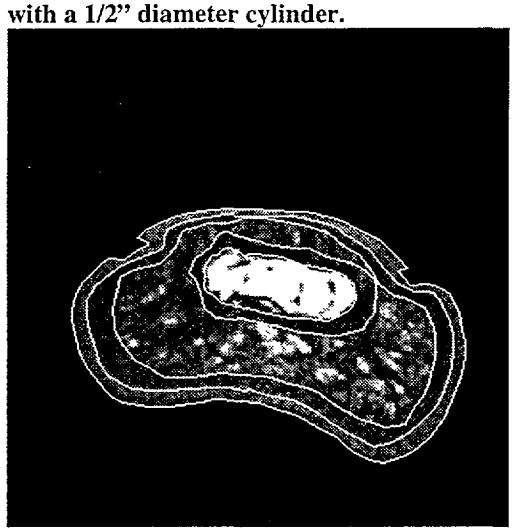

Figure 7.4.16: Fingerpad indented to 2 mm with a 1" diameter cylinder.

Figure 7.4: Cross sectional images located 2mm proximal to the tip of the bone of the human fingerpad. The resolution of each image is 125 x 125 x500μm with a field of view of 2.0 cm. Each image indicates the type of load and depth of indentation.

It can be seen that the inner layers have approximately the same shapes as those of the surface profiles. It can also be noted that sharp corners due to edges are reduced in the inner layers. This indicates that the inner layers filter out the higher spatial frequencies of the sharp corners, acting like low pass filters.

7.2 Effect of Depth

Each finger was loaded to the three depths of 0mm, 1mm and 2mm with the assumption that a majority of tasks completed in typical manual tasks do not deform the finger to greater depths. This was completed for each shape to examine skin profiles as well as layers below. Figure 7.5 shows the surface profiles for each indentor for the three subjects.

Subject 1

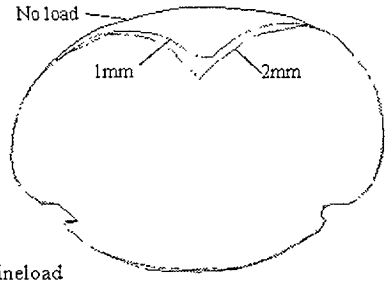

Lineload

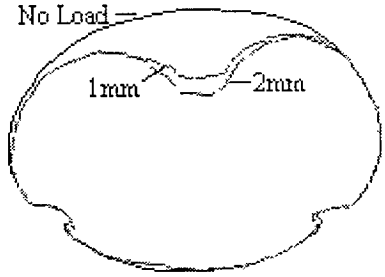

1/16" Rectangular Bar

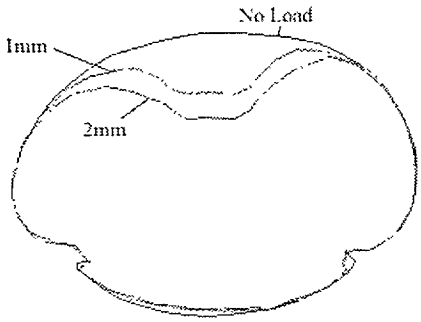

1/8" rectangular bar

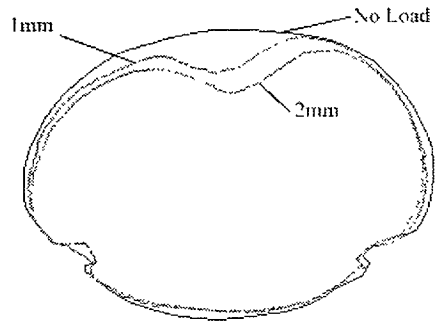

1/8" Cylinder

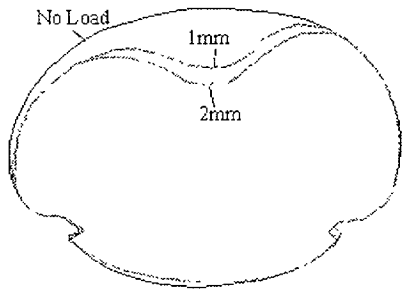

1/4" Cylinder

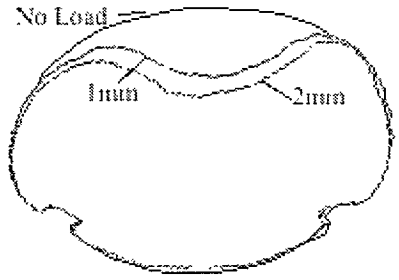

1/2" Cylinder

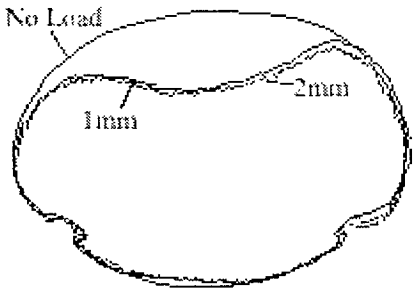

1" Cylinder

Subject 2

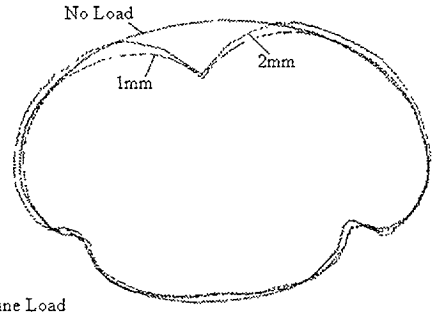

Line Load

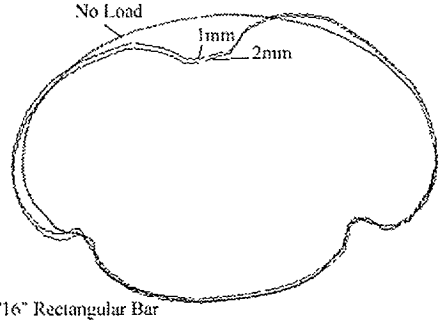

1/16" Rectangular Bar

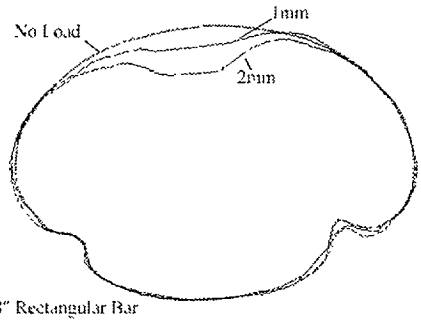

1/8" Rectangular Bar

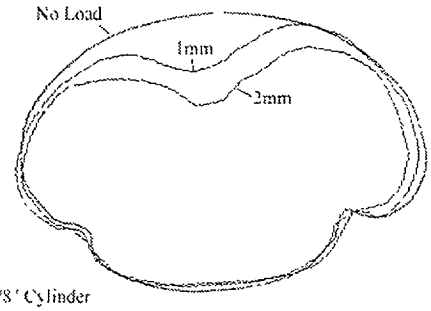

1/8 ' Cylinder

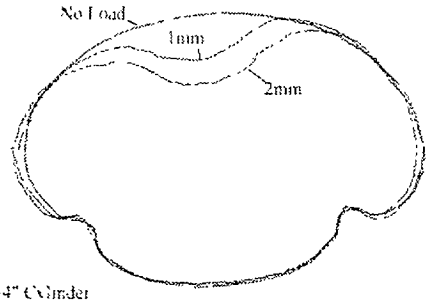

1/4" Cylinder

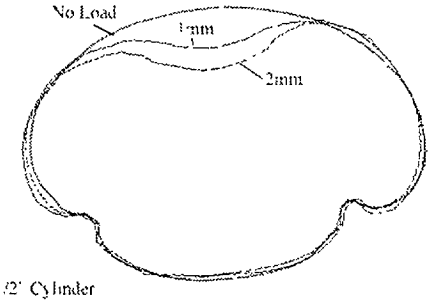

1/2' Cylinder

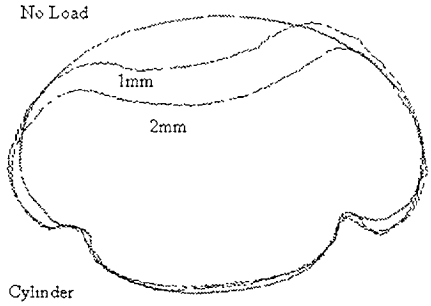

1" Cylinder

Subject 3

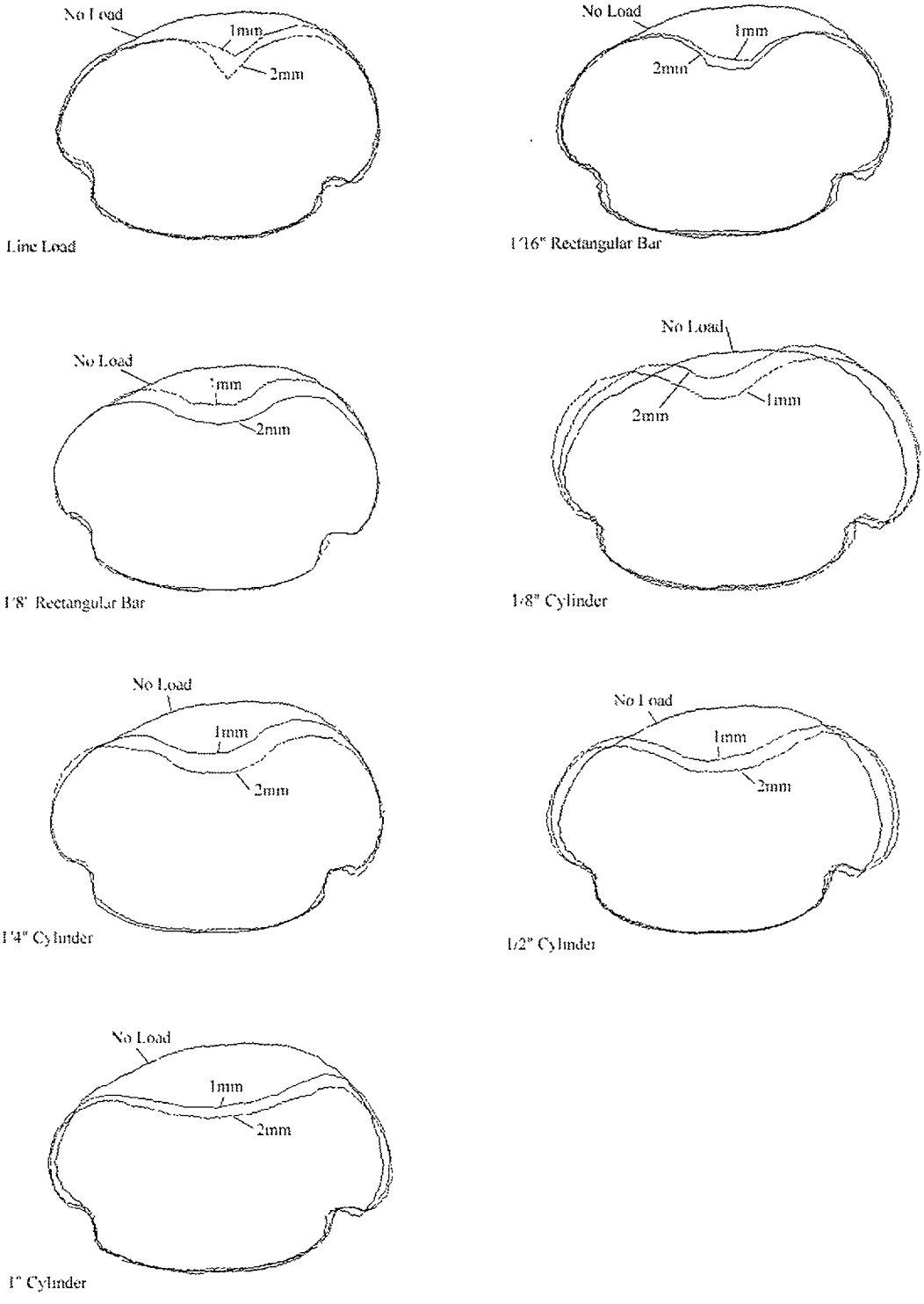

Figure 7.5: The contours illustrate the change in surface profiles according to indentor depth for each indentor and subject.

It can be seen that the tissue in the center compresses more with increasing loads with minimal expansion laterally. Also, the outer skin profile more dramatically takes on the shape of the indentor at higher loads.

It should be noted that the several surface profiles under load do not match with the unloaded profile (size appears incorrect). This is mainly because of the difficulties in locating the same slice each time. Subject 1's data was collected in two experimental sessions and the finger was only removed from the finger holder once. This data appears to have less error in matching profiles and the depth of indentation. Subject 2 & 3's data were collect over 5 sessions and the fingers were removed four times from the finger holder which allowed for more potential for error in slice selection. In some of the cross sections, the difference between the 1mm and 2mm indentations does not appear to be 1mm. This may be a result of the finger holder flexing (see Section 7.4 for further discussion of this error).

7.3 Effect of Shape

To investigate the effect of shape on fingerpad deformation, each finger was loaded with either a rectangular bar or a cylinder. These indentors varied in size from 1/8" and 1/16" for the rectangular bar and 1/8", ¼", ½" and 1" diameter for the cylinders. Figure 7.6 shows the

Subject 1

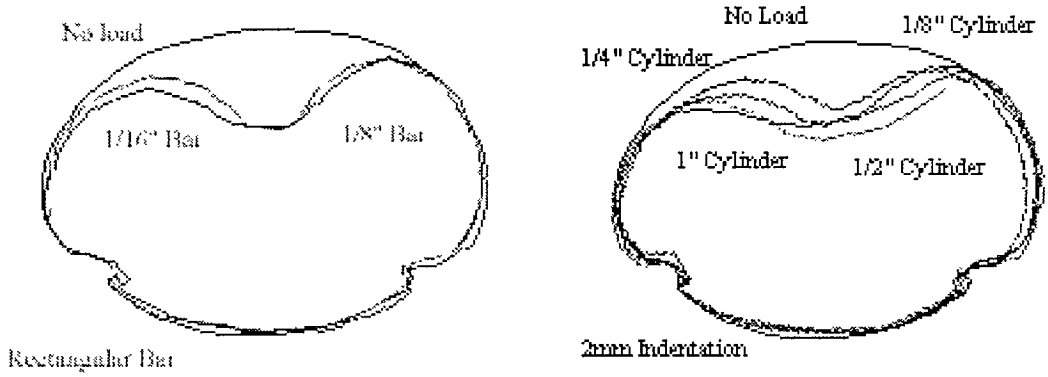

(a) (b)

Subject 2

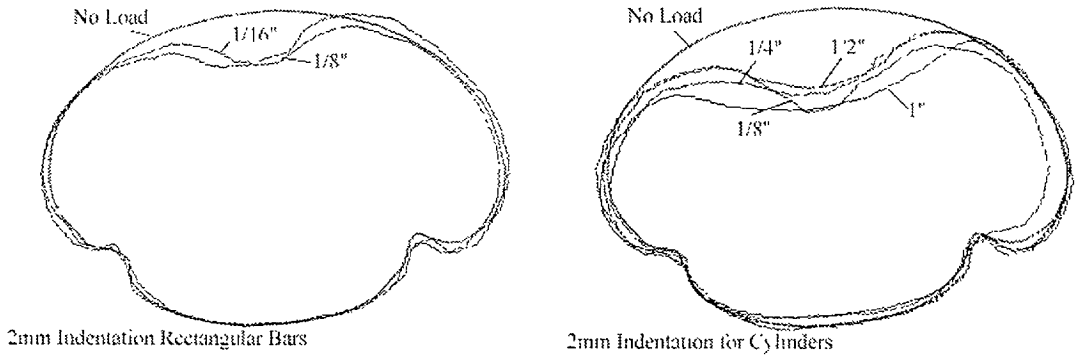

(a) (b)

Subject 3

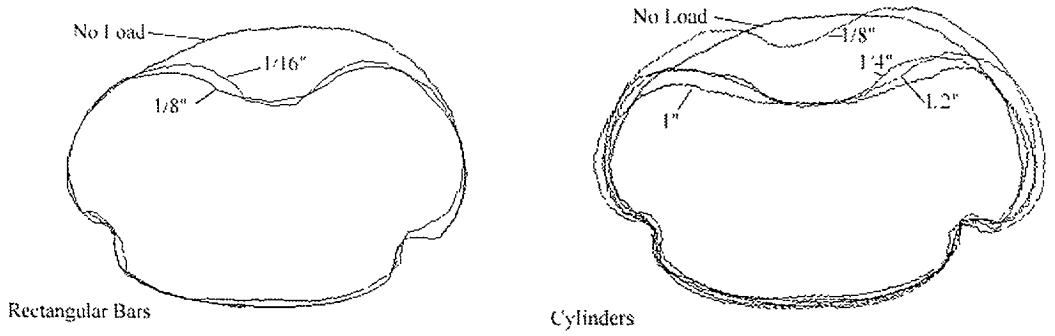

(a) (b)

Figure 7.6: (a) Superimposed surface plots of the finger under no load as well as indented to 2mm with 1/16" and 1/8" rectangular bars. (b) Superimposed surface plots of the finger indented to 2mm with 1/8", ¼", ½" and 1" diameter cylinders.

outer finger deformation profiles for both the rectangular bars superimposed and the four cylinders superimposed at a 2mm depth. It can be seen that little displacement occurred laterally despite increased surface area of the indentor.

It should be noted, especially with the cylindrical indentors, that the middle point of indentation did not seem to be indented to the same location for each image. Suggested causes for this maybe due to the finger holder flexing under load, the slice selection not being coincident each time (as suggested by the 1/8" cylinder in Subject 3) and/or additional compression added accidentally as it was placed inside the 1 inch magnetic bore. Since it also seems to be more problematic with the cylindrical probes, this suggests that the extra surface area may have caused higher forces for the same depth of indentation, which resulted in the probe flexing at the nylon screws which held the probe and the end cap in place.

7.4 Fingerpad Compressibility

The superimposed images indicate some compression of the finger in the indentation direction. To examine whether the tissue under the stimuli compresses or gets displaced along the axis of the bone, images were taken along the longitudinal axis for the unindented finger and the finger indented to 2mm with the $1/8^{th}$ inch rectangular bar indentor. Longitudinal image slices were located at the center of the finger, and at 3.0 mm from the center. Cross sectional images were located at ~2mm distal to the end of the bone and at the point of separation of the indentor with the skin. Figure 7.7 shows the unindented finger superimposed with the indented finger for two of the subjects.

Subject 1

Figure 7.1: Longitudinal-section of the unindented vs. the indented finger at the center of the finger along the axis of the bone. The lighter image indicates the unindented finger. These images indicate that the finger does not bulge longitudinally under indentation.

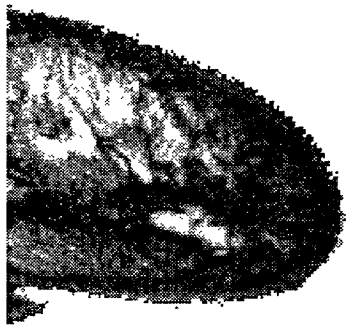

Figure 7.2: Longitudinal sections of the finger at 3mm from the center line of both the indented and unindented finger. The sections appear to be exactly the same shape.

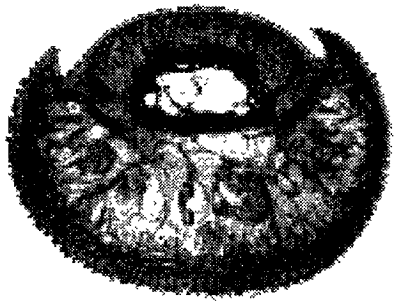

Figure 7.3: Cross sections of the finger at the point the indentor separated from the finger of the unindented and indented superimposed on each other. These images also show no displacement of tissue in any direction.

Subject 3

Figure 7.4: Longitudinal sections of the finger located at the center for the indented and unindented case superimposed on each other. This image also indicates no expansion of tissue at the end where the indentor separates from the finger.

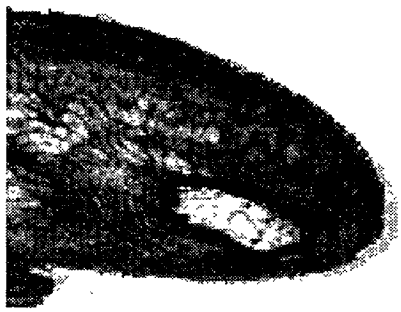

Figure7.5: Longitudinal sections superimposed for the indented and unindented finger at 3mm from center line. Image shows some expansion at the tip of the finger for the indented finger.

Figure 7.6: Cross sections of the indented and unindented finger at the point of separation of the indentor from the skin. This image illustrates almost no difference in shape between the two cases.

Figure7.7: Cross sections of the indented and unindented finger at 2mm distal to the tip of the bone superimposed. These images show no lateral expansion of tissue just as seen in previous cross sections located at 1mm proximal from the tip of the bone. The above images were taken with a resolution of 118x 118μm with an image slice thickness of 1mm.

The cross sectional images located at the center of the finger show little to no lateral displacement laterally of the finger tissue. The tissue volume displaced by the indentor cannot be seen at either end of the indentor or along the axis of the bone. This would imply that the finger tissue gets compressed at this location. This appears to be true for both subjects, except that subject 3 did have a small amount of tissue bulge at the tip of the finger, but not enough to balance the amount of tissue compressed by the indentor. These results are consistent with the findings by Gulati (1992) where he found that the fingerpad compresses up to 5% at a depth of indentation of 3mm by a flat plate.

To confirm the above visual observations, the cross sectional areas of each of the tissue layers and lengths of the tissue boundaries were calculated using the fitted contours. See Appendix G for the calculations of length and area for the three subjects and Appendix H for the program source code for calculations. The percent change in area and length between the deformed and undeformed finger, gives insight into whether the fingerpad is

compressing. Figure 7.8 shows the mean percent change (over three subjects) in length and area for each indentor, depth of indentation and tissue layer. See Appendix I for the percent change in length and area for each subject. For the graphs on length, a positive value indicates that the deformed surface profile is smaller in length than the undeformed surface profile. A negative value means that the deformed profile had stretched as compared to the undeformed or resting length. In general, the mean percent change in length is negative for each indentor, especially the line load which indicates surface profile expansion. However, percent changes less than about 5 percent may be attributed to error due to variability in slice selection and are not expected to be significant.

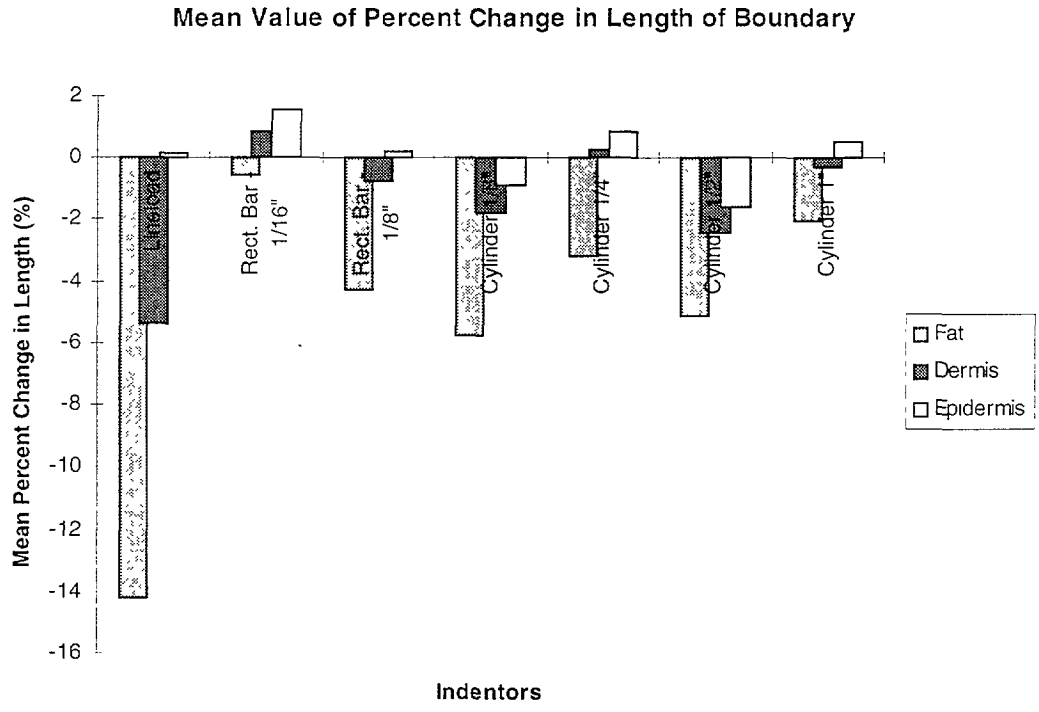

Figure 7.8.1: Bar chart illustrates the mean percent change in the length of each tissue boundary for three subjects. These values were for the finger indented to 1mm in depth. A positive value indicates contraction of the boundary and a negative value implies stretch of the boundary profile.

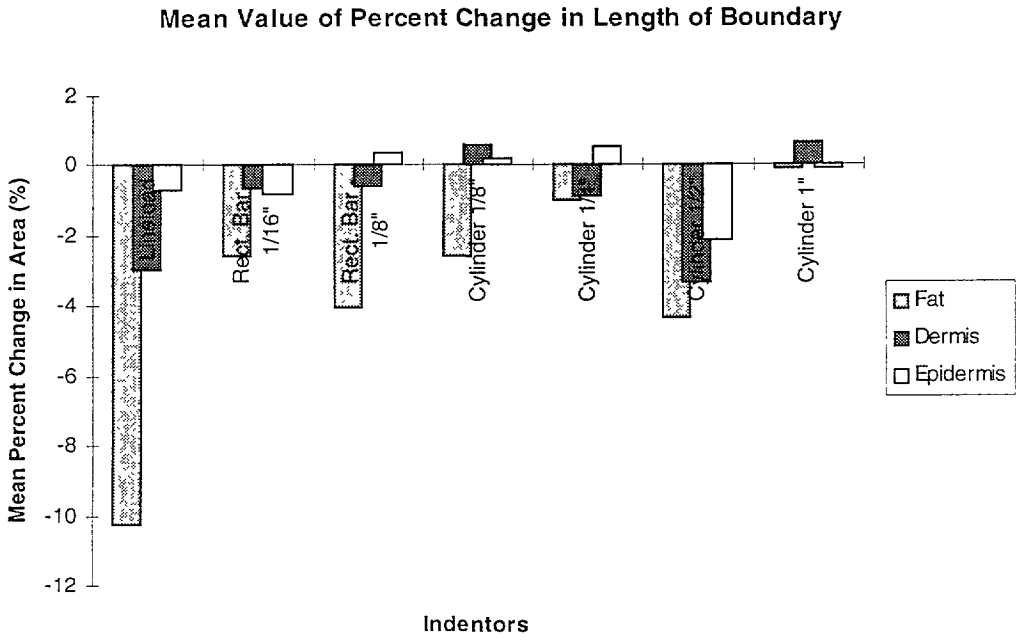

Figure 7.8.2: Bar chart illustrates the mean percent change in the length of each tissue boundary for three subjects. These values were for the finger indented to 2mm in depth. A positive value indicates contraction of the boundary and a negative value implies stretch of the boundary.

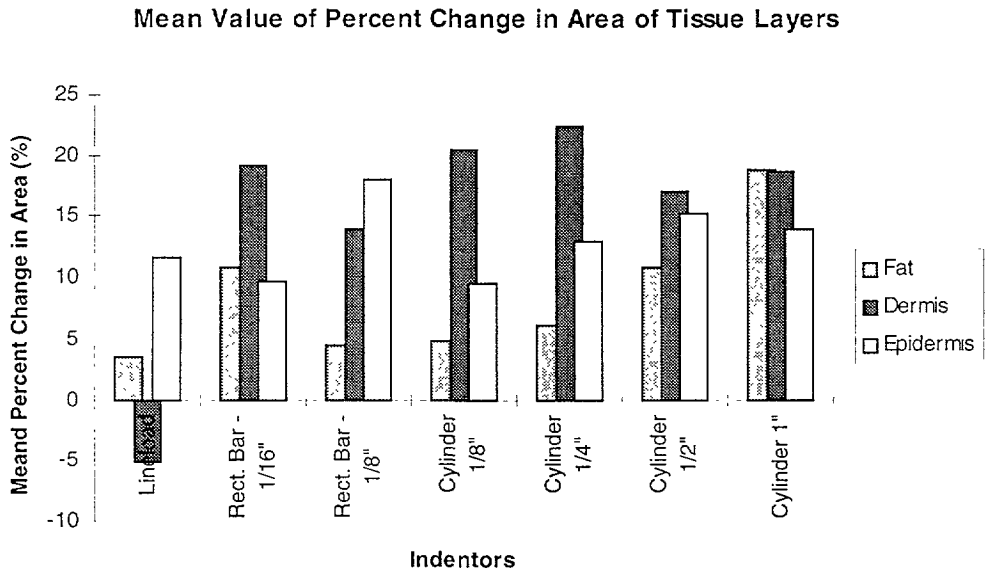

Figure 7.8.3: Bar chart illustrates the mean percent change in the area of each tissue layer for three subjects. These values were for the finger indented to 1mm in depth. A positive value indicates compression of the tissues and a negative value implies expansion of the tissue.

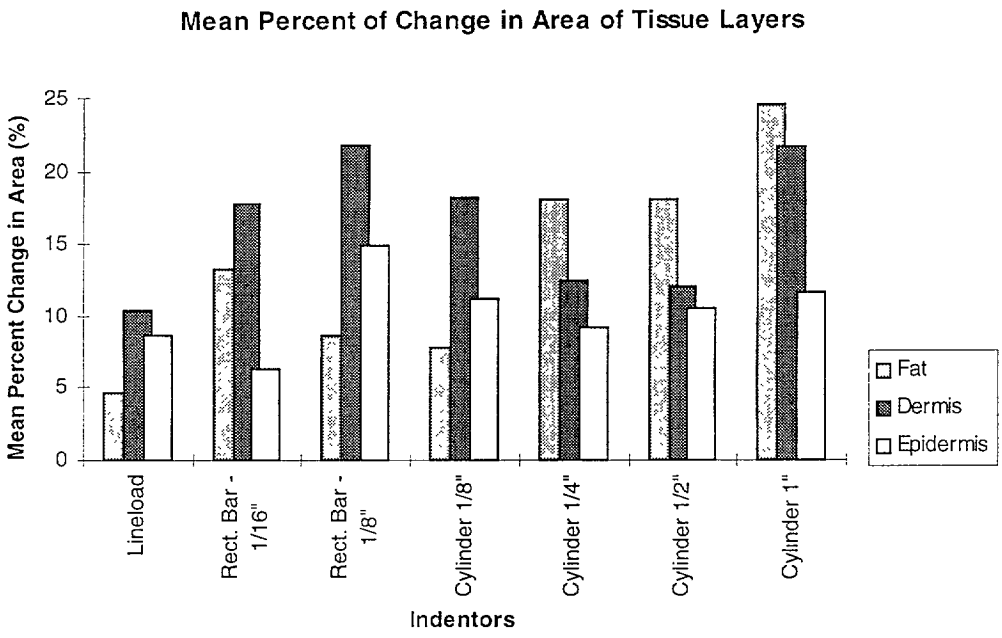

Figure 7.8.4: Bar chart illustrates the mean percent change in the area of each tissue layer for three subjects. These values were for the finger indented to 2mm in depth. A positive value indicates compression of the tissues and a negative value implies expansion of the tissue.

The area profiles seen in Figure 7.8 also suggest that the tissues get compressed under load. A positive value means that the area of the undeformed finger layer is greater than the deformed one which implies tissue compression within the cross section. A negative value would mean that the tissue layer expanded. Because of the difficulties in exact location of the slice, small changes in percent length or area can be ignored. However, values larger than about 5% are expected to be valid. Except for the line load at 1mm depth indentation, the data suggests that each tissue layer compresses with application of a load. The variance seen for the line load may be due to the difficulty of the snake finding the dermal-adipose (fat) border.

Chapter 8

Summary and Future Work

8.1 Summary

MRI proved to be a useful method in obtaining internal geometry and observing the biomechanical behavior of the *in vivo* human fingerpad. Images acquired represent almost the highest resolution possible, while maintaining adequate contrast and reasonable imaging time. Image segmentation techniques provided a method to analyze the behavior of each tissue layer under load. Techniques such as "active contours" proved to be accurate as compared to judging by eye and reproducible in the segmenting tissue layers. Image registration allowed for comparison in tissues and identifying tissue behavior. It was found that under load, each tissue layer of the fingerpad compresses both

longitudinally and axially. The data suggests that the inner layers of the finger act as low pass filters smoothing the effects of high spatial frequencies such as sharp corners.

The methods used in this study did not provide a way to measure stress or strain in the tissues. Although initially it was thought that strain might be measured from the data, the image resolution and errors in locating image slices prevented accurate measurement of tissue displacement. The use of blood vessels as locators also proved to be of limited use as a result of motion artifacts, pulse and MRI machine difficulties.

8.2 Suggestions for Future Work

Continued research in the field of the biomechanics of the *in vivo* fingerpad can be done in several forms. First, the data obtained from this research project can be used to improve computational models of the fingerpad by comparing biomechanical behavior the between human and model data. The data can be used to verify mathematical models of the fingerpad for simulations of tissue mechanics.

MRI resolution and motion artifacts due to long imaging times prevented analysis of the fingerpad at the level of the finger ridges. Studies using methods such as Ultrasound Backscatter Microscope allow for visualization of the finger ridges at the surface and several millimeters below the skin. Resolution of 10 μm can be achieved with such methods.

The finger holder significantly improved the signal to noise ratio by eliminating motion artifacts. However, it often flexed under load, which resulted in errors of indentation depth. The holder could be also be redesigned to increase the load without removing the finger from the magnet. This would decrease errors in relocating the image slice and improve the chances of measuring tissue relocation needed for strain measurements. The addition of a force sensor would also allow for estimation of surface stresses.

At this time, real time MRI imaging does not have sufficient resolution to measure the fingerpad biomechanical behavior under dynamic loads. However, the precision and methods of these machines are improving at a fast rate and the tools for dynamic measurements maybe available within the next five years.

Appendix A

Raw Data: Subject 2

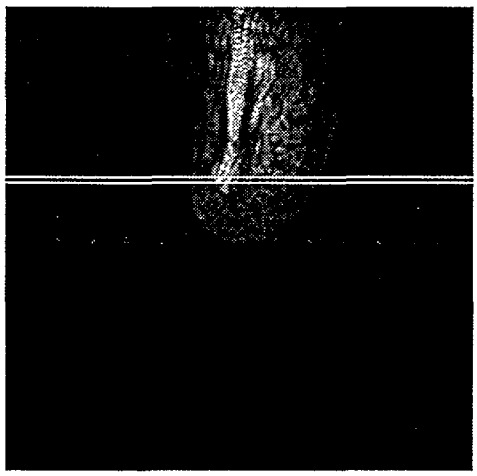

Figure A.1: Longitudinal cross section of the finger pad used to locate axial image at 1mm from the tip of the bone (white lines).

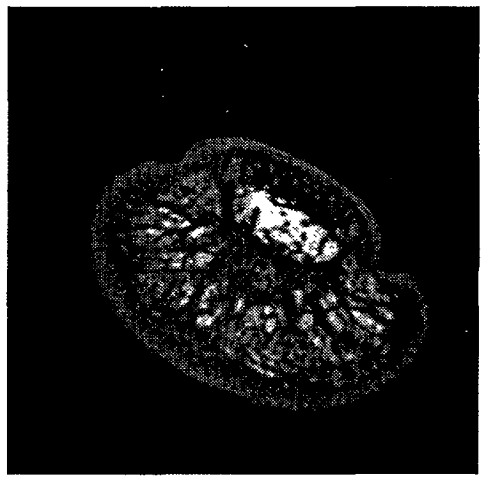

Figure A.2: Axial section of the fingerpad with no load applied

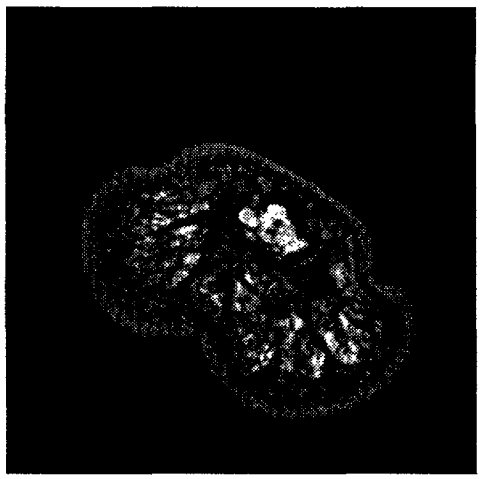

Figure A.3: Fingerpad indented to 1 mm with a lineload.

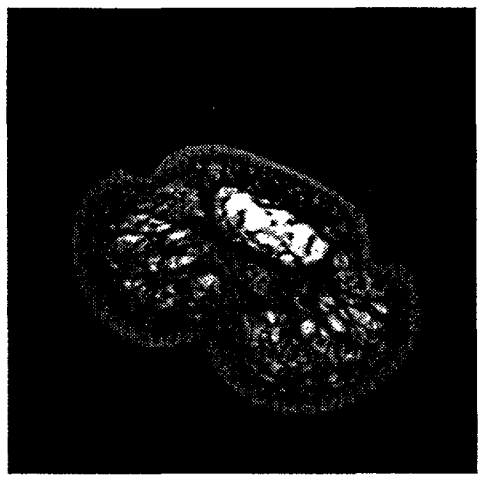

Figure A.4: Fingerpad indented to 2 mm with a lineload.

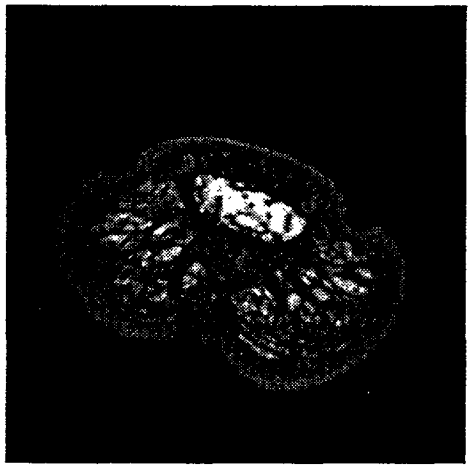

Figure A.5: Fingerpad indented to 1 mm with a 1/16" wide rectangular bar.

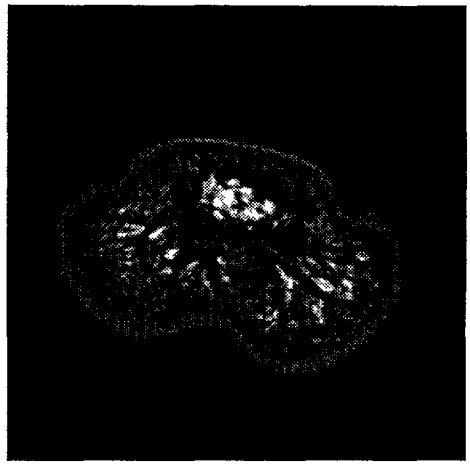

Figure A.6: Fingerpad indented to 2 mm with a 1/16" wide rectangular bar.

Figure A.7: Fingerpad indented to 1mm with a 1/8" wide rectangular bar.

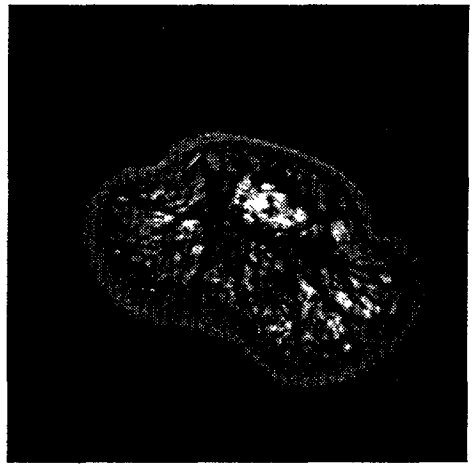

Figure A.8: Fingerpad indented to 2 mm with a 1/8" wide rectangular bar.

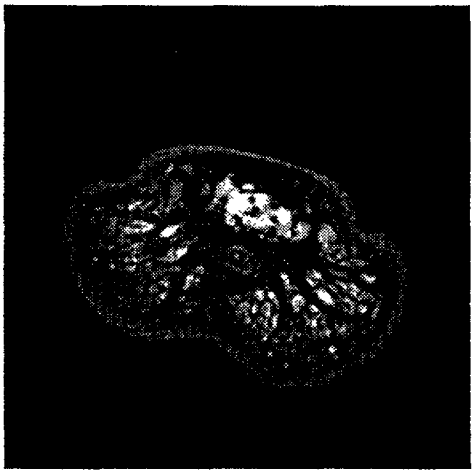

Figure A.9: Fingerpad indented to 1 mm with a 1/8" diameter cylinder.

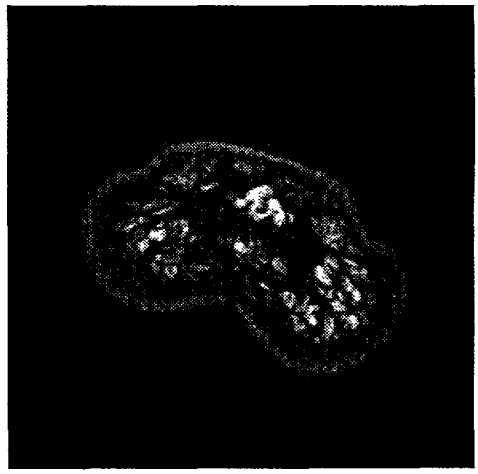

Figure A.10: Fingerpad indented to 2 mm with a 1/8" diameter cylinder.

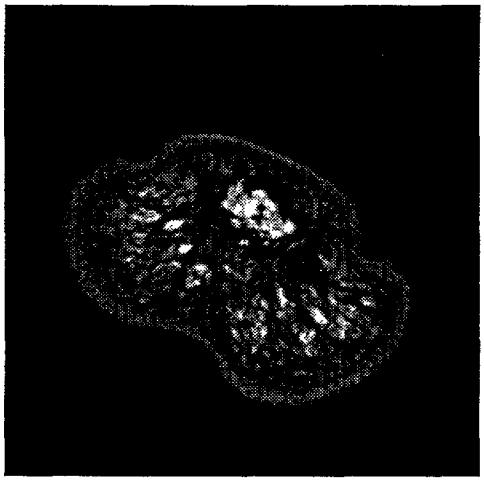

Figure A.11: Fingerpad indented to 1mm with a 1/4" diameter cylinder.

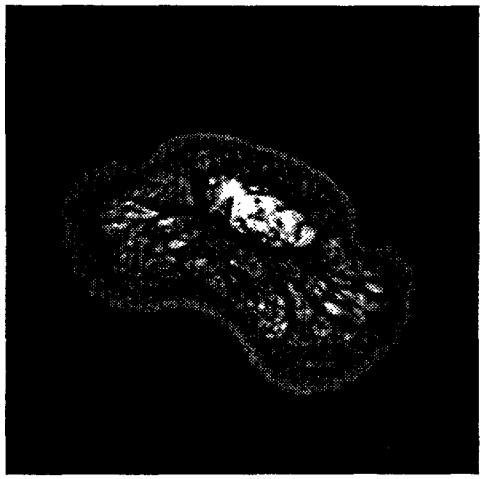

Figure A.12: Fingerpad indented to 2mm with a 1/4" diameter cylinder.

Figure A.13: Fingerpad indented to 1mm with a 1/2" diameter cylinder.

Figure A.14: Fingerpad indented to 2 mm with a 1/2" diameter cylinder.

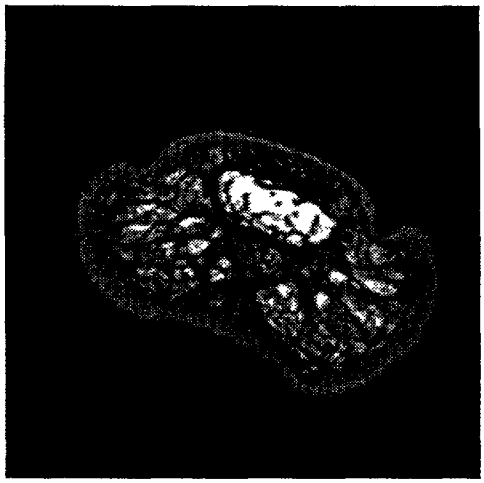

Figure A.15: Fingerpad indented to 1 mm with a 1" diameter cylinder.

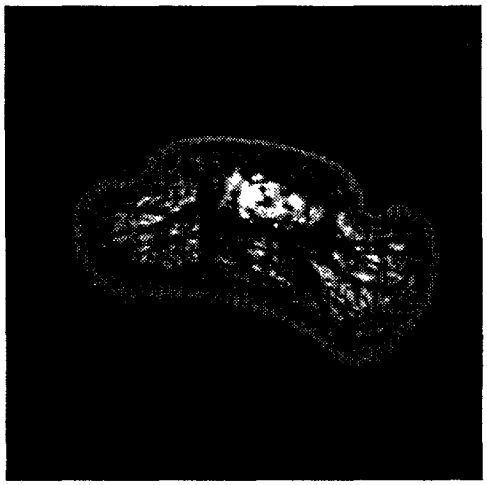

Figure A.16: Fingerpad indented to 2 mm with a 1" diameter cylinder.

Appendix B

Raw Data: Subject 3

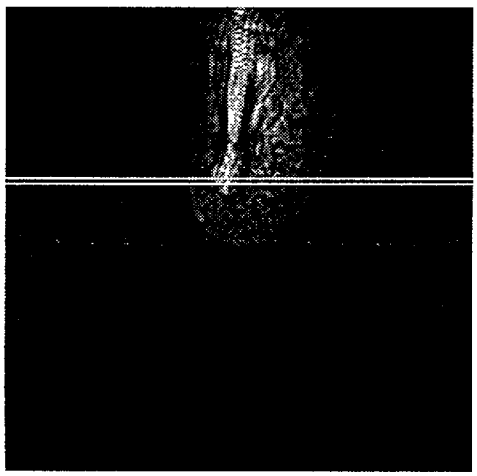

Figure B.1: Longitudinal cross section of the finger pad used to locate axial image at 1mm from the tip of the bone (white lines).

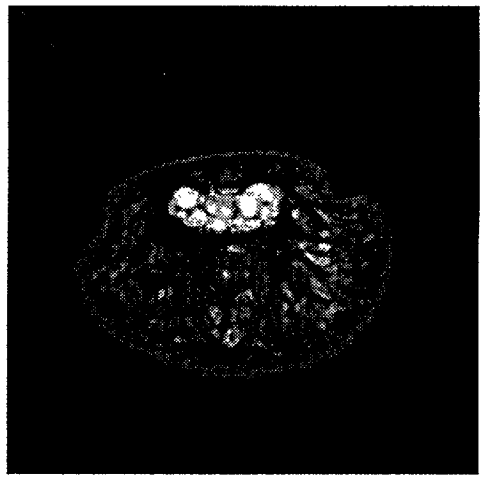

Figure B.2: Axial section of the fingerpad with no load applied

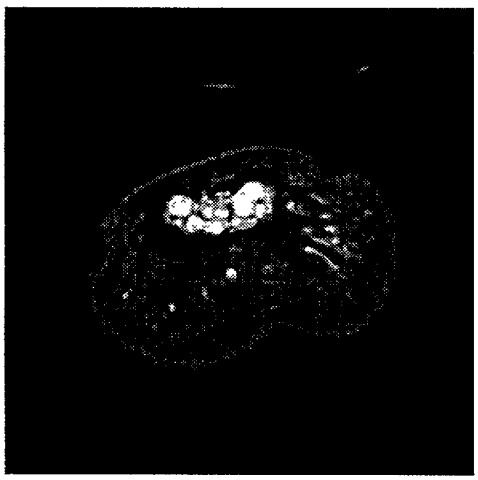

Figure B.3: Fingerpad indented to 1 mm with a line load.

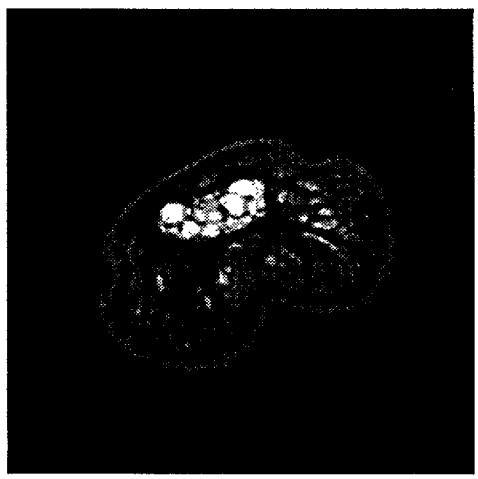

Figure B.4: Fingerpad indented to 2 mm with a line load.

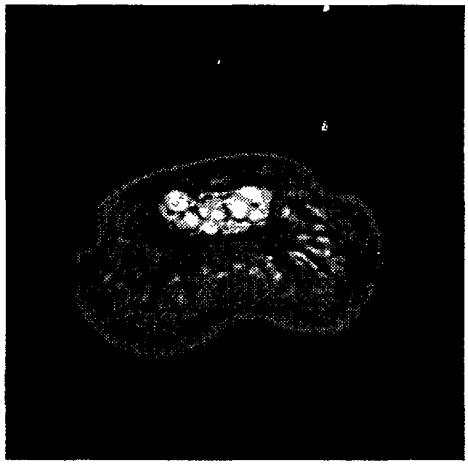

Figure B.5: Fingerpad indented to 1 mm with a 1/16" wide rectangular bar.

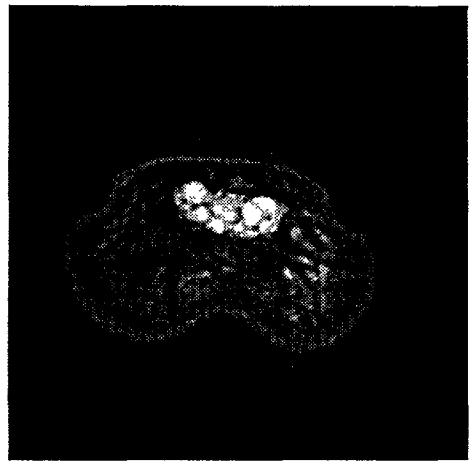

Figure B.6: Fingerpad indented to 2 mm with a 1/16" wide rectangular bar.

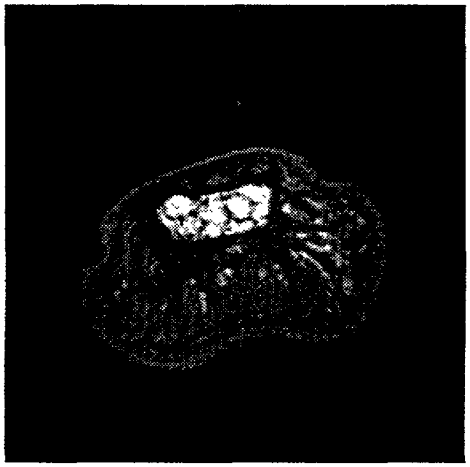

Figure B.7: Fingerpad indented to 1mm with a 1/8" wide rectangular bar.

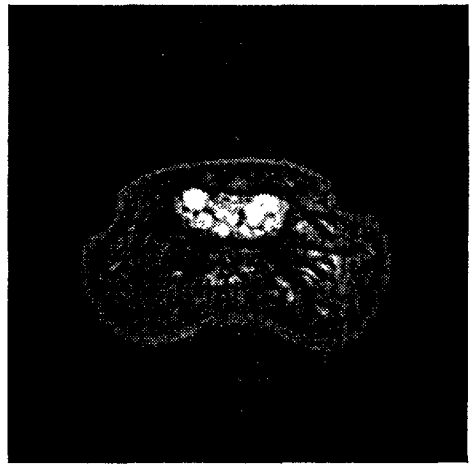

Figure B.8: Fingerpad indented to 2 mm with a 1/8" wide rectangular bar.

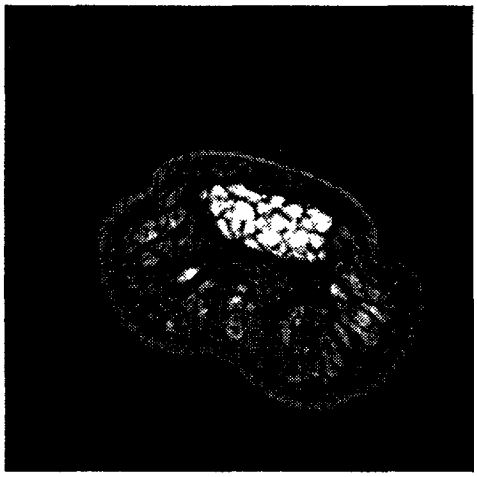

Figure B.9: Fingerpad indented to 1 mm with a 1/8" diameter cylinder.

Figure B.10: Fingerpad indented to 2 mm with a 1/8" diameter cylinder.

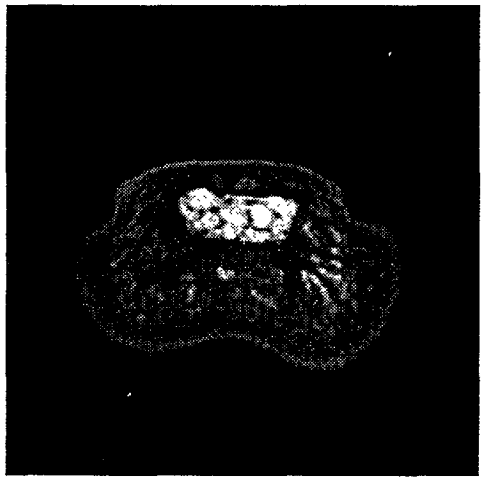

Figure B.11: Fingerpad indented to 1mm with a 1/4" diameter cylinder.

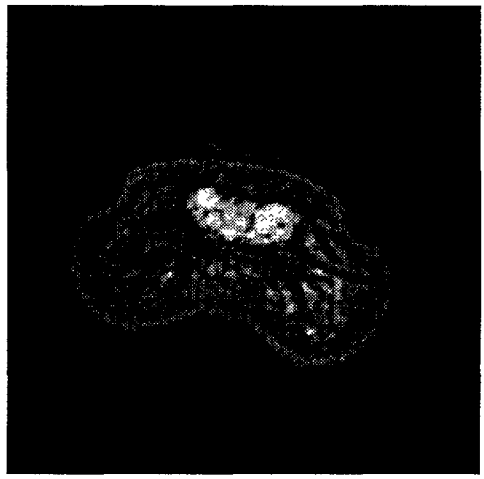

Figure B.12: Fingerpad indented to 2mm with a 1/4" diameter cylinder.

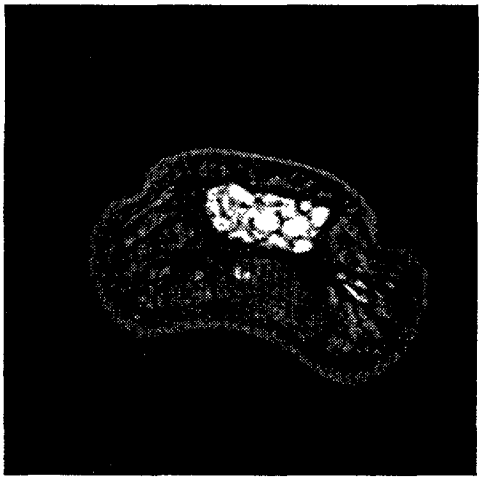

Figure B.13: Fingerpad indented to 1mm with a 1/2" diameter cylinder.

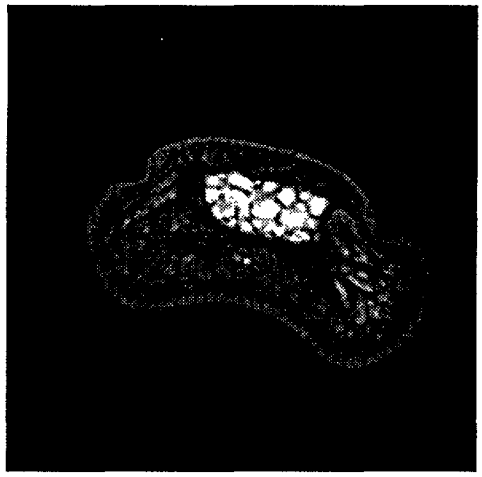

Figure B.14: Fingerpad indented to 2 mm with a 1/2" diameter cylinder.

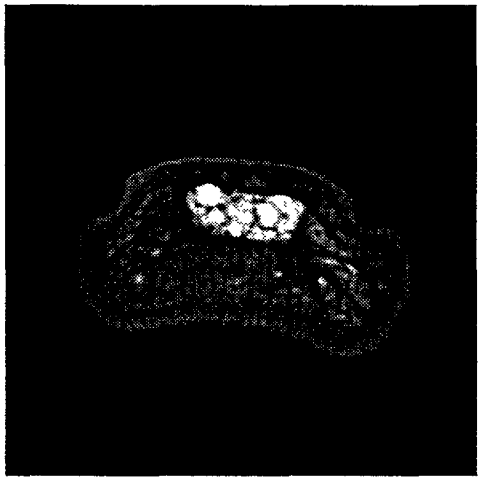

Figure B.15: Fingerpad indented to 1 mm with a 1" diameter cylinder.

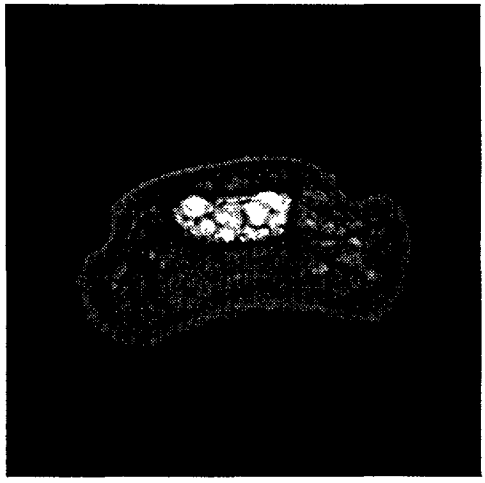

Figure B.16: Fingerpad indented to 2 mm with a 1" diameter cylinder.

Appendix C

Active Contour Model

The following derivation expands on the work completed by Michael Kass, Andrew Witkin and Demetri Terzopoulos in the article ***Snakes: Active Contour Models*** (Kass, et al, 1987). Refer to the article for further explanations of the algorithm.

The snake is an energy minimizing continuity spline directly influenced by internal and external image forces. The snake can be represented parametrically as an energy functional as follows:

$$E^{*}_{snake} = \int_0^1 E_{\text{int}} V(s) + E_{image} V(s) + E_{con} V(s) ds \qquad \text{(C.1)}$$

where E_{int} represents the internal energy due bending, E_{image} attracts the snake towards image features like lines and edges, and E_{con} produces external forces.

The internal energy consists of a first order term controlled by $\alpha(s)$ and a second order term controlled by $\beta(s)$. This energy functional can be written as

$$E_{\text{int}} = \left(\alpha(s) \left| V_s(s) \right|^2 + \beta(s) \left| V_{ss}(s) \right|^2 \right) / 2 \qquad \text{(C.2)}$$

The first order term acts like a membrane and the second order term like a plate. The external constraint term, E_{con}, contains forces such as $-k(x_1-x_2)^2$ or a $1/r^2$ that push the snake towards a projecting feature or repulses the snake. For the purpose of this research project, $E_{con} = 0$. Instead, the program was designed with a interactive user interface that allowed the user to move a node from one local minimum into another. Additionally, the program allowed the user to fix points around image features that had dramatic changes in direction, such as the areas around the corners of the nailbed. E_{image} term consists of three energy functionals to attract the snake to lines, edges and terminations.

$$E_{image} = w_{line}E_{line} + w_{edge}E_{edge} + w_{term}E_{term}$$

where

$$E_{line} = -\left(G_o \nabla^2 I\right)^2$$

$$E_{edge} = -\left|\nabla I(x,y)\right|^2$$

$$E_{term} = \frac{\partial\theta}{\partial n_\perp} = \frac{C_{yy}C_x^{\,2} - 2C_{xy}C_xC_y + C_{xx}C_y^{\,2}}{\left(C_x^{\,2} + C_y^{\,2}\right)^2}$$

where

$$C(x,y) = G_\sigma(x,y)I(x,y)$$

$$\theta = \tan^{-1}\left(\frac{C_y}{C_x}\right)$$

$$n = (\cos\theta, \sin\theta)$$

$$n_\perp = (-\sin\theta, \cos\theta)$$

Combining terms E_{edge} and E_{term} results in a snake that is attracted to edges and terminations.

Now, let

$$E_{ext}=E_{image}+E_{con}$$

For this application, $\alpha(s)=\alpha$ and $\beta(s)=\beta$ are constants which gives rise to the following Euler equations.

$$(\alpha x_s)_s+(\beta(x_{ss}))_{ss}+\frac{\partial E_{ext}}{\partial x}=0$$

$$(\alpha y_s)_s+(\beta(y_{ss}))_{ss}+\frac{\partial E_{ext}}{\partial y}=0$$

Letting $f_x(i)=\frac{\partial E_{ext}}{\partial x_i}$, $f_y(i)=\frac{\partial E_{ext}}{\partial y_i}$, $v_i=(x_i, y_i)$ and $\mathbf{v}(0)=\mathbf{v}(n)$, the derivatives can be approximated by finite differences. The Euler equations can then be written as follows.

$$\alpha_i(x_i-x_{i-1})-\alpha_{i+1}(x_{i+1}-x_i)+\beta_{i-1}(x_{i-2}-2x_{i-1}+x_i)-2\beta_i(x_{i-1}-2x_i+x_{i+1})$$
$$+\beta_{i+1}(x_i-2x_{i+1}+x_{i+2})+f_x(i)=0$$

$$\alpha_i(y_i-y_{i-1})-\alpha_{i+1}(y_{i+1}-y_i)+\beta_{i-1}(y_{i-2}-2y_{i-1}+y_i)-2\beta_i(y_{i-1}-2y_i+y_{i+1})$$
$$+\beta_{i+1}(y_i-2y_{i+1}+y_{i+2})+f_y(i)=0$$

Rewriting, these equations can represented in a matrix form as

$$\mathbf{Ax}+\mathbf{f_x}(\mathbf{x},\mathbf{y})=0$$

$$\mathbf{Ay}+\mathbf{f_y}(\mathbf{x},\mathbf{y})=0$$

where **A** is a pentadiagonal banded matrix.

$$A=\begin{bmatrix} 2(\alpha+3\beta) & -(\alpha+4\beta) & \beta & \dots & 0 & \beta & -(\alpha+4\beta) \\ -(\alpha+4\beta) & 2(\alpha+3\beta) & -(\alpha+4\beta) & \beta & \dots & 0 & \beta \\ \beta & -(\alpha+4\beta) & 2(\alpha+3\beta) & -(\alpha+4\beta) & \beta & \dots & 0 \\ \ddots & \ddots & \ddots & \ddots & \ddots & \ddots & \ddots \\ \ddots & \ddots & \ddots & \ddots & \ddots & \ddots & \ddots \\ \beta & 0 & \dots & \beta & -(\alpha+4\beta) & 2(\alpha+3\beta) & -(\alpha+4\beta) \\ -(\alpha+4\beta) & \beta & 0 & \dots & \beta & -(\alpha+4\beta) & 2(\alpha+3\beta) \end{bmatrix}$$

By setting the right sides of the two equations equal to the product of the step size and the negative time derivatives of the left hand sides, a solution can be found. Assuming that $\mathbf{f}_x$ and $\mathbf{f}_y$ are constant during each step, **A** can be calculated faster for each iteration of external forces.

The external forces can be found by an explicit Euler method. The internal forces are specified by the banded **A** matrix and evaluated at the time derivative at t rather than t-1. This results in and implicit Euler step for the internal forces. The equations are as follows.

$$Ax_t + f_x\left(x_{t-1}, y_{t-1}\right) = -\gamma\left(x_t - x_{t-1}\right)$$

$$Ay_t + f_y\left(x_{t-1}, y_{t-1}\right) = -\gamma\left(y_t - y_{t-1}\right)$$

where γ = the step size.

By inverting the matrix, the equations can be solved.

$$x_t = \left(A + \gamma I\right)^{-1}\left(\gamma x_{t-1} - f_x\left(x_{t-1}, y_{t-1}\right)\right)$$

$$y_t = \left(A + \gamma I\right)^{-1}\left(\gamma y_{t-1} - f_x\left(x_{t-1}, y_{t-1}\right)\right)$$

Utilizing the above equations, a program in Maltab was written to converge on the edges of a tissue. See Appendix D for the program code.

Appendix D

Active Contour Matlab Program

```
%%%%%%%%%%%%%%%%%%%%%%%%%%%%%%%%%%%%%%%%%%%%
% Program to read in MRI images, filter the image
% and fit a specific snake to locate a specific edge.
%
% Program was modified according to quality of image
%
%  Kimberly Voss
%  Original Program developed on 9/7/96
%  Updated on 1/8/97; 4/10/97
%%%%%%%%%%%%%%%%%%%%%%%%%%%%%%%%%%%%%%%%%%%%

clear;
close;
close;
close;
close;
close;
close;

%%%%%%%%%%%%%%%%%%%%%%%%%%%%%%%%%
% Open data file :
% file is in binary form
%%%%%%%%%%%%%%%%%%%%%%%%%%%%%%%%%

disp('read data file ..');
[filename, pathname]=uigetfile('*.*', 'File to open', 10,10)
fid=fopen(filename, 'r');

%%%%%%%%%%%%%%%%%%%%%%%%%%%%%%%%%%
% Create image matrix
%%%%%%%%%%%%%%%%%%%%%%%%%%%%%%%%%%
```

```
numPixel = 256*256;
numByte = numPixel * 4;
numBegin = 1;
numEnd = numBegin + numByte -1;
xPixel = 256;
yPixel = 256;

%%%%%%%%%%%%%%%%%%%%%%%%%%%%%%%%%%%%%%%%
% Read in data and assign it as
% an interger
%%%%%%%%%%%%%%%%%%%%%%%%%%%%%%%%%%%%%%%%

[data1, count]=fread(fid, 'uint8');
data=data1(numBegin:numEnd);
disp('number of elements read..')
count
fclose(fid);

%%%%%%%%%%%%%%%%%%%%%%%%%%%%%%%%%%%%%%%%
% Initialize image array
%%%%%%%%%%%%%%%%%%%%%%%%%%%%%%%%%%%%%%%%

byte1(xPixel, yPixel)=0;
byte2(xPixel, yPixel)=0;
byte3(xPixel, yPixel)=0;
byte4(xPixel, yPixel)=0;

%%%%%%%%%%%%%%%%%%%%%%%%%%%%%%%%%%%%%%%%
% Assigning each 8 bit integer to a
% single byte
%%%%%%%%%%%%%%%%%%%%%%%%%%%%%%%%%%%%%%%%

k=1;
for i=1:xPixel
  for j=1:yPixel
    byte1(i,j)=data(k);
    k=k+1;
    byte2(i,j)=data(k);
    k=k+1;
    byte3(i,j)=data(k);
    k=k+1;
    byte4(i,j)=data(k);
    k=k+1;
  end
end

%%%%%%%%%%%%%%%%%%%%%%%%%%%%%%%%%%%%%%%%
% Set colormap to grayscale
%%%%%%%%%%%%%%%%%%%%%%%%%%%%%%%%%%%%%%%%

graymap = gray(256);
colormap(graymap);

%%%%%%%%%%%%%%%%%%%%%%%%%%%%%%%%%%%%%%%%
```

```
% Reconstruct the bits to form the image
%%%%%%%%%%%%%%%%%%%%%%%%%%%%%%%%%%%%%%%%

byte12(xPixel,yPixel)=0;
for i=1:xPixel
  for j=1:yPixel
    temp=byte1(i,j)*256^3+byte2(i,j)*256^2+byte3(i,j)*(256)+byte4(i,j);
    byte12(i,j)=temp;
  end
end

%%%%%%%%%%%%%%%%%%%%%%%%%%%%%%%%%%%%%%%%%
% Free up memory
%%%%%%%%%%%%%%%%%%%%%%%%%%%%%%%%%%%%%%%%%

clear data
clear data12
clear byte1
clear byte2
clear byte3
clear byte4

%%%%%%%%%%%%%%%%%%%%%%%%%%%%%%%%%%%%%%%%
% Find max and min values for byte 12
%%%%%%%%%%%%%%%%%%%%%%%%%%%%%%%%%%%%%%%%

maxGray = max(max(byte12));
minGray = min(min(byte12));
rang=maxGray-minGray;

%%%%%%%%%%%%%%%%%%%%%%%%%%%%%%%%%%%%%%%%
% Display data so that the grayscales
% are maximized for the given range
%%%%%%%%%%%%%%%%%%%%%%%%%%%%%%%%%%%%%%%%

data12=(byte12-minGray+1)/rang*256;

%%%%%%%%%%%%%%%%%%%%%%%%%%%%%%%%%%%%%%%%
% Eliminate background noise through
% thresholding
%%%%%%%%%%%%%%%%%%%%%%%%%%%%%%%%%%%%%%%%

for i=1:256
        for j=1:256
                if data12(i,j)<=5
                data12(i,j)=1;
                end;
        end;
end;

imshow(data12);

%%%%%%%%%%%%%%%%%%%%%%%%%%%%%%%%%%%%%%%
% Highpass filter to remove non-uniform
% intensities due to low frequency
```

```
% variations from the non-uniform
% magnetic field
%%%%%%%%%%%%%%%%%%%%%%%%%%%%%%%%%%%%%

F=[0 0.01 0.02 0.02 0.04 0.1 0.2 0.4 0.8 1.0];
M=[0 0 0 0 1 1 1 1 1 1];

N=7;
[B,A]=yulewalk(N,F,M);
fim=data12;

        for i=1:256
         fim(i,:)=exp(filtfilt(B,A,log(data12(i,:))));
        end;

fim=fim/max(max(fim))*255;

figure(2)
colormap('gray');
imshow(data12);

%%%%%%%%%%%%%%%%%%%%%%%%%%%%%%%%%%%%%%%%%%%%
% Utilize a median filter on image to remove
% spurous noise
%%%%%%%%%%%%%%%%%%%%%%%%%%%%%%%%%%%%%%%%%%%%

figure(3)
colormap('gray');
mri_filter=medfilt2(fim,[3 3]);
imshow(mri_filter);

%%%%%%%%%%%%%%%%%%%%%%%%%%%%%%%%%%%%%%%%%
% Snake program to find an edge
%%%%%%%%%%%%%%%%%%%%%%%%%%%%%%%%%%%%%%%%%

%%%%%%%%%%%%%%%%%%%%%%%%%%%%%%%%%%%%%%%%%
% Calculate the partial derivatives of image
%%%%%%%%%%%%%%%%%%%%%%%%%%%%%%%%%%%%%%%%%

h=1/9*ones(3,3);
fmri_filter=filter2(h,mri_filter,'same');
[ffx ffy]=gradient(mri_filter);


%%%%%%%%%%%%%%%%%%%%%%%%%%%%%%%%%%%%%%%%%
% Set number of nodes, stiffness and
% flexibility of snake
%%%%%%%%%%%%%%%%%%%%%%%%%%%%%%%%%%%%%%%%%

n=80;                   % Number of nodes
b=2.5;              % Increases stiffness of snake
a=5.0;                  % Increases flexibility of snake

ga=.4;                  % Set the step size
Ax=pent(n,a,b);         % Build the A matrix
```

```
%%%%%%%%%%%%%%%%%%%%%%%%%%%%%%%%%%%%%%
% Create initial shape of the conformable
% contour
%%%%%%%%%%%%%%%%%%%%%%%%%%%%%%%%%%%%%%

par=1:n;
r0=109;                       % Radius of ellipse in x direction
r1=92;                        % Radius of ellipse in y direction
x=140+r0*cos(-pi/2-(par-1)/n*2*pi);
y=145+r1*sin(-pi/2-(par-1)/n*2*pi);

%%%%%%%%%%%%%%%%%%%%%%%%%%%%%%%%%%%%%%
% Obtain input from user through the mouse
% to fix difficult points
%%%%%%%%%%%%%%%%%%%%%%%%%%%%%%%%%%%%%%

[xfix,yfix] = ginput(20);
nfix=[5,6,7,8,9,72,73,74,75,76];

%%%%%%%%%%%%%%%%%%%%%%%%%%%%%%%%%%%%%%
% Background image for snake
%%%%%%%%%%%%%%%%%%%%%%%%%%%%%%%%%%%%%%

figure(4)
colormap('gray');
image(data12);
hold on;

xt_1=x';yt_1=y';
xt_1(nfix)=xfix;
yt_1(nfix)=yfix;

%%%%%%%%%%%%%%%%%%%%%%%%%%%%%%%%%%%%%
% Iterate conformable contour
%%%%%%%%%%%%%%%%%%%%%%%%%%%%%%%%%%%%%

%%%%%%%%%%%%%%%%%%%%%%%%%%%%%%%%%%%%%
% Timevarying gamma (gat) gain to simulate damping
% to help the snake converge on the edge
%%%%%%%%%%%%%%%%%%%%%%%%%%%%%%%%%%%%%

for i=1:400
        xt_1n=xt_1;
        yt_1n=yt_1;
        gat=19*ga*log(n+1);
        xt=inv(Ax+gat*eye(size(Ax)))*(gat*xt_1n -fx(ffx,xt_1n,yt_1n));
        yt=inv(Ax+gat*eye(size(Ax)))*(gat*yt_1n -fy(ffy,xt_1n,yt_1n));

%%%%%%%%%%%%%%%%%%%%%%%%%%%%%%%%%%%%%
% Fix points input from the user
%%%%%%%%%%%%%%%%%%%%%%%%%%%%%%%%%%%%%

        xt(nfix)=xt_1(nfix);
        yt(nfix)=yt_1(nfix);
```

```
%%%%%%%%%%%%%%%%%%%%%%%%%%%%%%%%%%%%%%%%%%%%%%%%%%%%%%%%%%%%%%%%%%%%%%%%%%%%
% Plot nodes for each each step
%%%%%%%%%%%%%%%%%%%%%%%%%%%%%%%%%%%%%%%%%%%%%%%%%%%%%%%%%%%%%%%%%%%%%%%%%%%%

  norm(xt-xt_1);
  norm(yt-yt_1);

          xt_1=xt;
          yt_1=yt;


          if rem(i,10)==0
          li=plot(xt, yt, 'g.');
          end;
end;

%%%%%%%%%%%%%%%%%%%%%%%%%%%%%%%%%%%%%%%%%%%%%%%%%%%%%%%%%%%%%%%%%%%%%%%%%%%%
% Clear upmemory
%%%%%%%%%%%%%%%%%%%%%%%%%%%%%%%%%%%%%%%%%%%%%%%%%%%%%%%%%%%%%%%%%%%%%%%%%%%%

clear xt_1n
clear yt_1n
clear ypixel
clear xpixel

%%%%%%%%%%%%%%%%%%%%%%%%%%%%%%%%%%%%%%%%%%%%%%%%%%%%%%%%%%%%%%%%%%%%%%%%%%%%
% Plot initial resting place of snake
%%%%%%%%%%%%%%%%%%%%%%%%%%%%%%%%%%%%%%%%%%%%%%%%%%%%%%%%%%%%%%%%%%%%%%%%%%%%

snake=plot([xt;xt(1)],[yt;yt(1)],'r');
          set(snake,'linewidth',1);
circle=plot([x';x(1)],[y';y(1)],'b');
          set(circle,'linewidth',1);
title(['Nodes = ',num2str(n),', g = ' ,num2str(ga), ', a = ', num2str(a),', b = ',num2str(b)]);


%%%%%%%%%%%%%%%%%%%%%%%%%%%%%%%%%%%%%%%%%%%%%%%%%%%%%%%%%%%%%%%%%%%%%%%%%%%%
%  Reiterate Program
%  Push contours to right location
%%%%%%%%%%%%%%%%%%%%%%%%%%%%%%%%%%%%%%%%%%%%%%%%%%%%%%%%%%%%%%%%%%%%%%%%%%%%

hold off;

%%%%%%%%%%%%%%%%%%%%%%%%%%%%%%%%%%%%%%%%%%%%%%%%%%%%%%%%%%%%%%%%%%%%%%%%%%%%
% Menu to allow user to choose whether or not
% to reiterate the contour
%%%%%%%%%%%%%%%%%%%%%%%%%%%%%%%%%%%%%%%%%%%%%%%%%%%%%%%%%%%%%%%%%%%%%%%%%%%%

select=0;
repeat=1;
while repeat < 100,
          k=menu('Snake', 'Iterate', 'Stop');
          if (k==1)
          repeat=repeat+1;
```

```
disp('Iterate snake..')

%%%%%%%%%%%%%%%%%%%%%%%%%%%%%%%%%%%%%%%%%%%%%%%%%%%%%%%%%%%%%%%%%%%%%%%
% Setup background image for contour
%%%%%%%%%%%%%%%%%%%%%%%%%%%%%%%%%%%%%%%%%%%%%%%%%%%%%%%%%%%%%%%%%%%%%%%

figure(5)
colormap('gray');
image(mri_filter);

%%%%%%%%%%%%%%%%%%%%%%%%%%%%%%%%%%%%%%%%%%%%%%%%%%%%%%%%%%%%%%%%%%%%%%%
% Find the desired node of contour to move
%%%%%%%%%%%%%%%%%%%%%%%%%%%%%%%%%%%%%%%%%%%%%%%%%%%%%%%%%%%%%%%%%%%%%%%

j=0;
[xmove,ymove] = ginput(1);          % select point near node

for i=1:n                           % Find all nodes in that region
        if ((xmove-10<=xt(i))&(xt(i)<=xmove+10)&(ymove-10<=yt(i))&(yt(i)<= ymove+10))
        j=j+1;
        collect(j)=i;
        end;
end;

%%%%%%%%%%%%%%%%%%%%%%%%%%%%%%%%%%%%%%%%%%%%%%%%%%%%%%%%%%%%%%%%%%%%%%%
% Find closest node to selected point
%%%%%%%%%%%%%%%%%%%%%%%%%%%%%%%%%%%%%%%%%%%%%%%%%%%%%%%%%%%%%%%%%%%%%%%

distance=100;
small=collect(1);
for p=1:j
        tempdistance=sqrt((xmove-xt(collect(p)))^2 +(ymove-yt(collect(p)))^2);
                if tempdistance<distance
                        small=collect(p);
                        distance=tempdistance;
                end ;
end;

%%%%%%%%%%%%%%%%%%%%%%%%%%%%%%%%%%%%%%%%%%%%%%%%%%%%%%%%%%%%%%%%%%%%%%%
% Select desired location to move node
%%%%%%%%%%%%%%%%%%%%%%%%%%%%%%%%%%%%%%%%%%%%%%%%%%%%%%%%%%%%%%%%%%%%%%%

[xmove,ymove] = ginput(1);
xt(small)=xmove;
yt(small)=ymove;

%%%%%%%%%%%%%%%%%%%%%%%%%%%%%%%%%%%%%%%%%%%%%%%%%%%%%%%%%%%%%%%%%%%%%%%
% Repeat Iteration
%%%%%%%%%%%%%%%%%%%%%%%%%%%%%%%%%%%%%%%%%%%%%%%%%%%%%%%%%%%%%%%%%%%%%%%

for i=1:20

        xt_1=xt;
        yt_1=yt;
        gat=19*ga*log(n+1);     %Timevarying gamma gain to simulate damping
```

```
        xt=inv(Ax+gat* eye(size(Ax)))*(gat*xt_1 -fx(ffx,xt_1,yt_1));
        yt=inv(Ax+gat* eye(size(Ax)))*(gat*yt_1 -fy(ffy,xt_1,yt_1));

        % fix points
        xt(nfix)=xt_1(nfix);
        yt(nfix)=yt_1(nfix);
        xt(small)=xt_1(small);
        yt(small)=yt_1(small);

        if rem(i,10)==0
        li=plot(xt, yt, 'w.');
        end;
end;

%%%%%%%%%%%%%%%%%%%%%%%%%%%%%%%%%%%%%%%%%%%%%%%%%%%%%%%%%%%%%%%%%%%%%%%%%%%%%%%
% Plot final position of the snake
%%%%%%%%%%%%%%%%%%%%%%%%%%%%%%%%%%%%%%%%%%%%%%%%%%%%%%%%%%%%%%%%%%%%%%%%%%%%%%%

image(data12)
hold on;
snake=plot([xt;xt(1)],[yt;yt(1)],'g');
        set(snake,'linewidth',1);
circle=plot([x';x(1)],[y';y(1)],'r');
        set(circle,'linewidth',1);
title(['Nodes = ',num2str(n),', g = ' ,num2str(ga), ', a = ', num2str(a),', b = ',num2str(b)]);

                else
                repeat=100;
                end;
        end;
hold off;
```

```
%%%%%%%%%%%%%%%%%%%%%%%%%%%%%%%%%%%%%%
% Function to create the pentadiagonal
% matrix Ax=pent(n,alfa,beta)
%%%%%%%%%%%%%%%%%%%%%%%%%%%%%%%%%%%%%%

function Ax=pent(n,a,b)

Ax=zeros(n);

        for i=1:n
                if i==1
                        Ax(i,n-1)=b;
                        Ax(i,n)=-(a+4*b);
                        Ax(i,i)=2*(a+3*b);
                        Ax(i,i+1)=-(a+4*b);
                        Ax(i,i+2)=b;
                elseif i==2
                        Ax(i,n)=b;
                        Ax(i,i-1)=-(a+4*b);
                        Ax(i,i)=2*(a+3*b);
                        Ax(i,i+1)=-(a+4*b);
                        Ax(i,i+2)=b;
                elseif i==n-1
                        Ax(i,i-2)=b;
                        Ax(i,i-1)=-(a+4*b);
                        Ax(i,i)=2*(a+3*b);
                        Ax(i,i+1)=-(a+4*b);
                        Ax(i,1)=b;
                elseif i==n
                        Ax(i,i-2)=b;
                        Ax(i,i-1)=-(a+4*b);
                        Ax(i,i)=2*(a+3*b);
                        Ax(i,1)=-(a+4*b);
                        Ax(i,2)=b;
                else
                        Ax(i,i-2)=b;
                        Ax(i,i-1)=-(a+4*b);
                        Ax(i,i)=2*(a+3*b);
                        Ax(i,i+1)=-(a+4*b);
                        Ax(i,i+2)=b;
                end;
        end;
```

```
%%%%%%%%%%%%%%%%%%%%%%%%%%%%%%%%%%%%%%%%%%%
% Functions to calculate the gradient
% in the x and y directions
%%%%%%%%%%%%%%%%%%%%%%%%%%%%%%%%%%%%%%%%%%%

function fx=fx(fxx,x,y)

imsz=max(size(fxx));

    for i=1:length(x)
        row=round(y(i));
        col=round(x(i));
            if row>imsz
              row=imsz ;
            elseif row <1
              row=1;
            end;

            if col>imsz
              col=imsz ;
            elseif col <1
              col=1;
            end;
        fx(i)=fxx(row,col);
    end;
fx=fx';


function fy=fy(fyy,x,y)

imsz=max(size(fyy));

    for i=1:length(x)
        row=round(y(i));
        col=round(x(i));
            if row>imsz
             row=imsz;
            elseif row <1
             row=1;
            end;

            if col>imsz
              col=imsz ;
            elseif col <1
             col=1;
            end;
        fy(i)=fyy(row,col);
     end;
fy=fy';
```

Appendix E

Raw Data: Subject 2

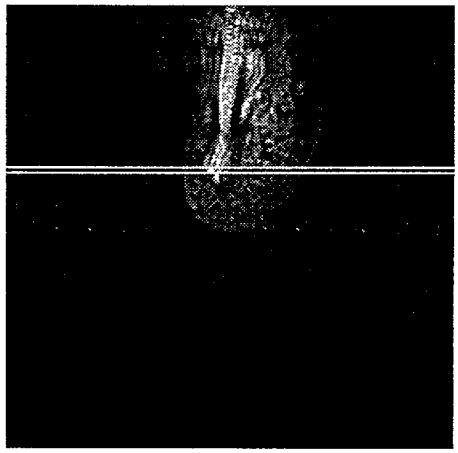

Figure E.1: Longitudinal cross section of the finger pad used to locate axial image at 1mm from the tip of the bone (white lines).

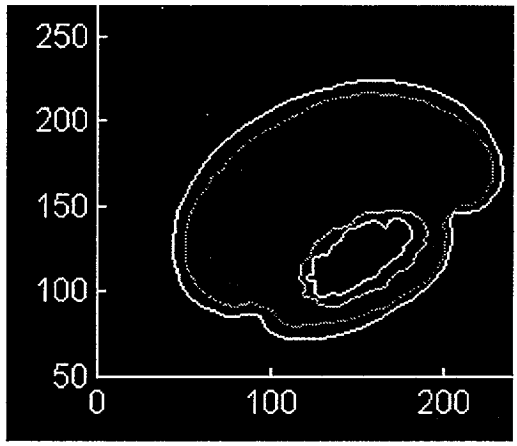

Figure E.2: Contours of the fingerpad with no load applied.

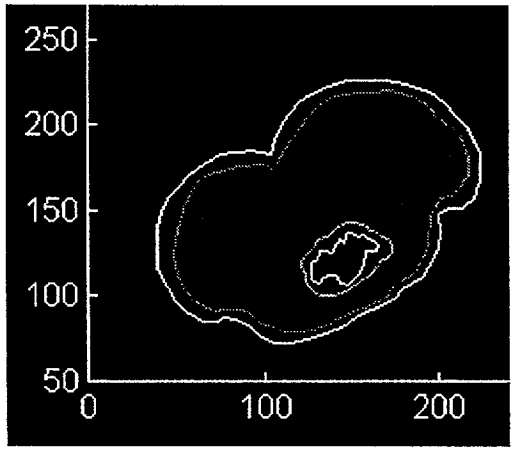

Figure E.3: Contours of fingerpad indented to 1 mm with a line load.

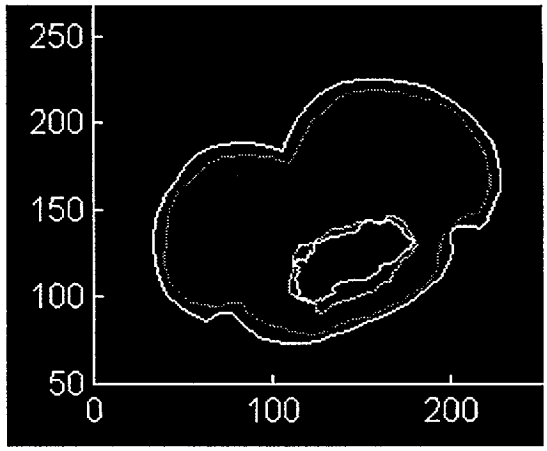

Figure E.4: Contours of fingerpad indented to 2 mm with a line load.

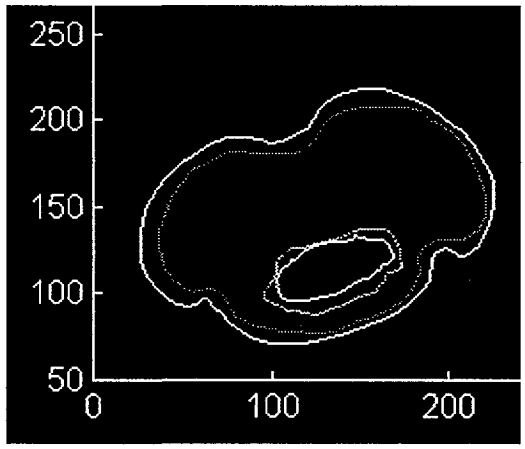

Figure E.5: Contours of fingerpad indented to 1 mm with a 1/16" wide rectangular bar.

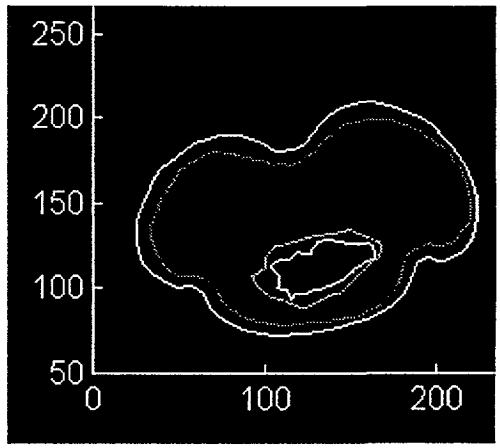

Figure E.6: Contours of fingerpad indented to 2 mm with a 1/16" wide rectangular bar.

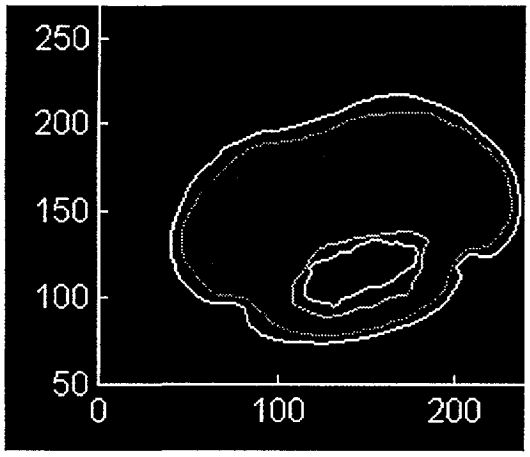

Figure E.7: Fingerpad indented to 1mm with a 1/8" wide rectangular bar.

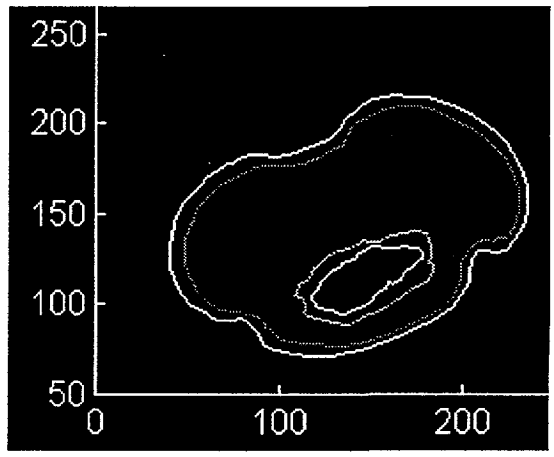

Figure E.8: Fingerpad indented to 2 mm with a 1/8" wide rectangular bar.

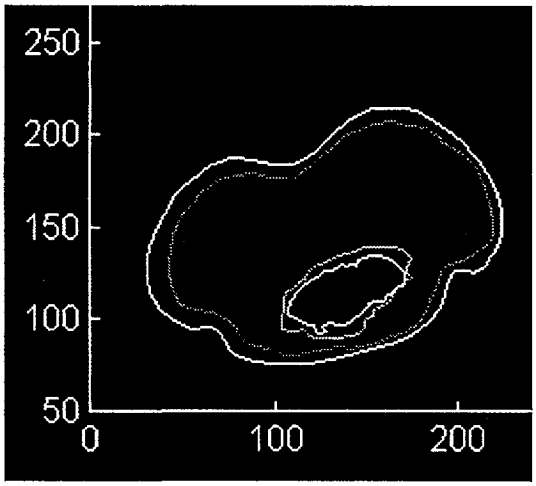

Figure E.9: Contours of fingerpad indented to 1 mm by a 1/8" cylinder.

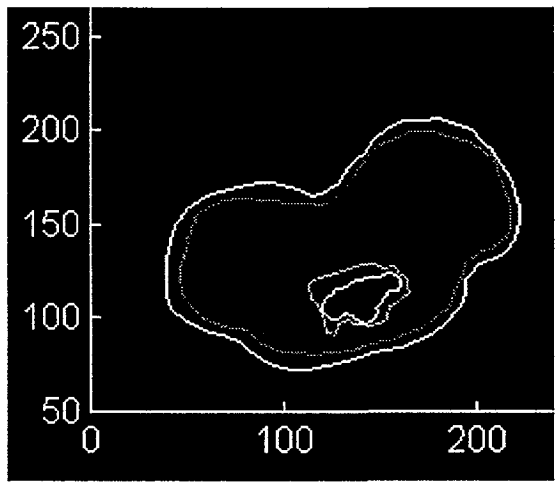

Figure E.10: Contours of fingerpad indented to 2 mm by a 1/8" cylinder.

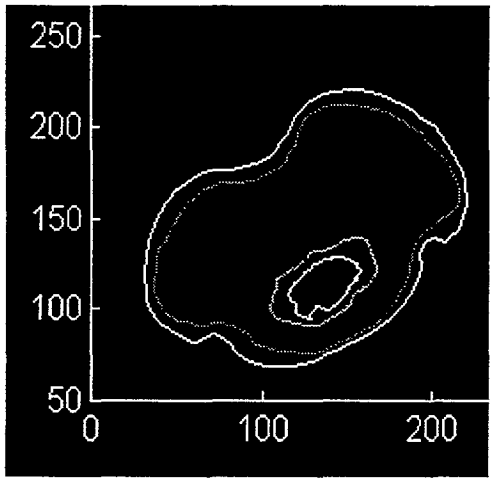

Figure E.11: Contours of fingerpad indented to 1mm with a 1/4" cylinder.

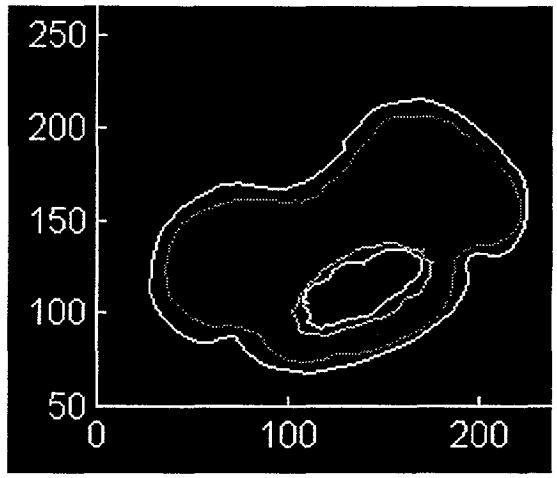

Figure E.12: Contours of fingerpad indented to 2mm with a 1/4" cylinder.

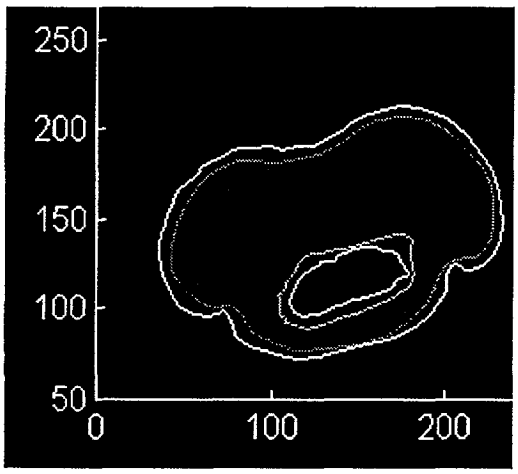

Figure E.13: Contours of fingerpad indented to 1mm with a 1/2" cylinder.

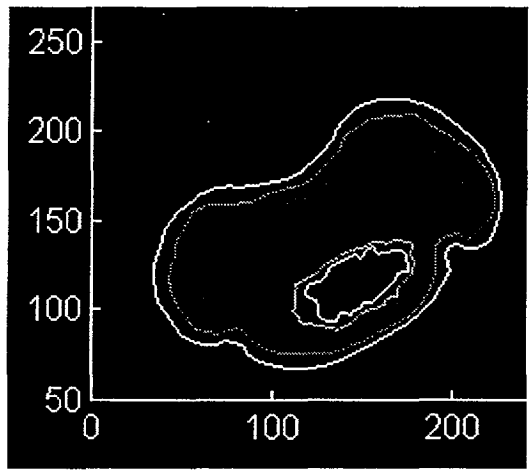

Figure E.14: Contours of fingerpad indented to 2 mm with a 1/2" cylinder.

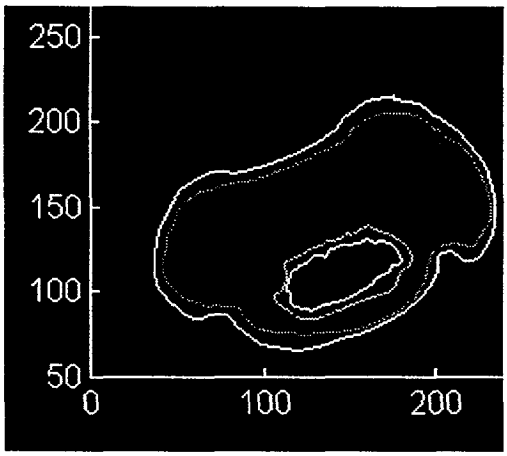

Figure E.15: Contours of fingerpad indented to 1 mm with a 1" cylinder.

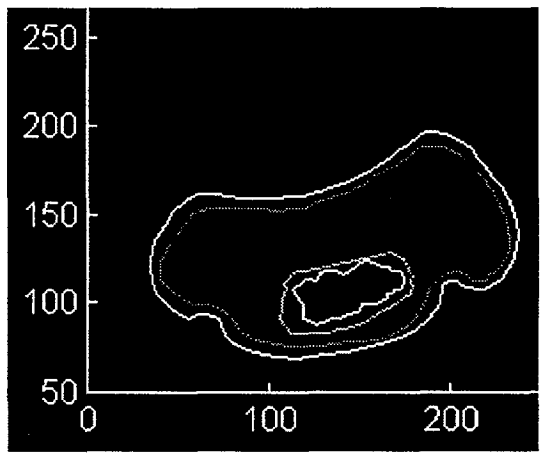

Figure E.16: Contours of fingerpad indented to 2 mm with a 1" cylinder.

Appendix F

Raw Data: Subject 3

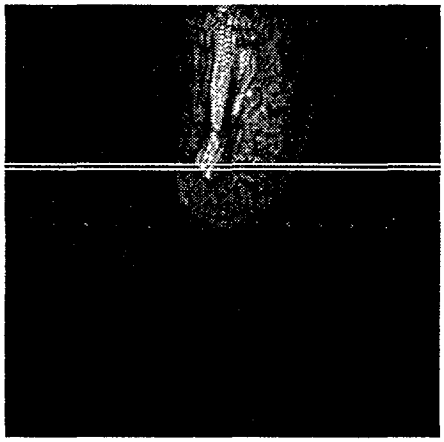

Figure F.1: Longitudinal cross section of the finger pad used to locate axial image at 1mm from the tip of the bone (white lines).

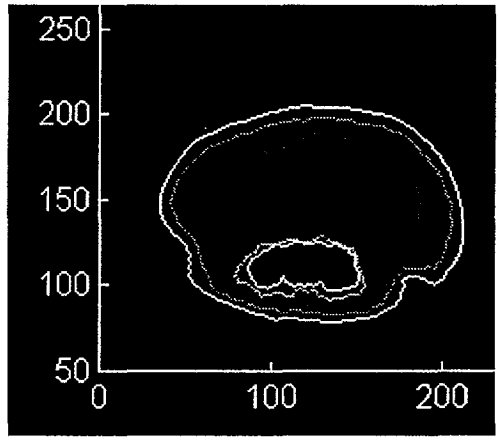

Figure F.2: Contours of the fingerpad with no load applied.

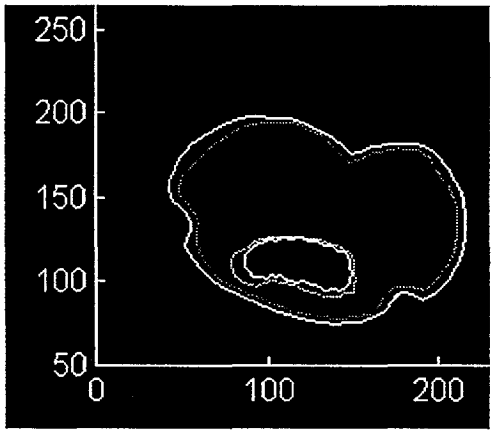

Figure F.3: Contours of fingerpad indented to 1 mm with a line load.

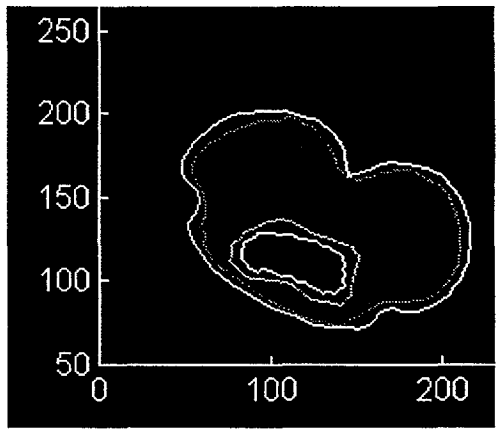

Figure F.4: Contours of fingerpad indented to 2 mm with a line load.

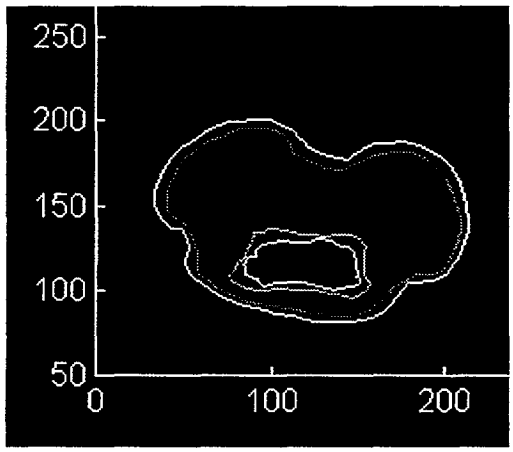

Figure F.5: Contours of fingerpad indented to 1 mm with a 1/16" wide rectangular bar.

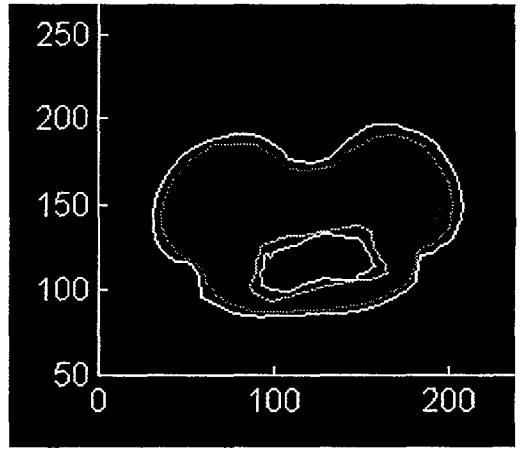

Figure F.6: Contours of fingerpad indented to 2 mm with a 1/16" wide rectangular bar.

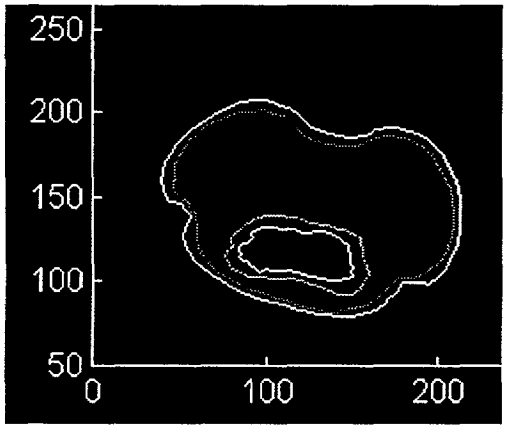

Figure F.7: Fingerpad indented to 1mm with a 1/8" wide rectangular bar.

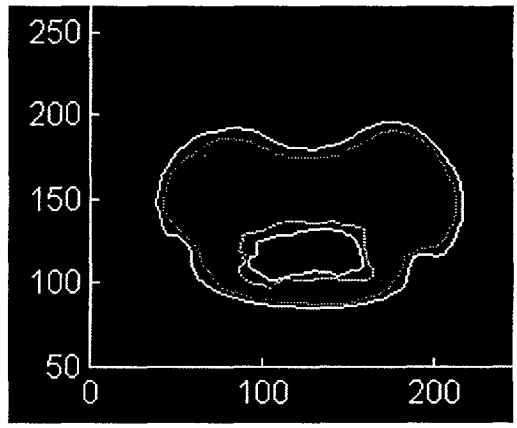

Figure F.8: Fingerpad indented to 2 mm with a 1/8" wide rectangular bar.

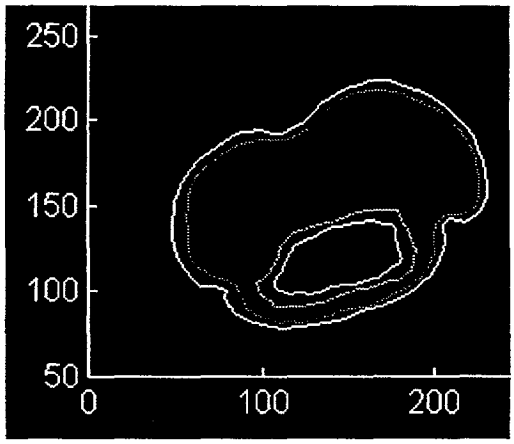

Figure F.9: Contours of fingerpad indented to 1 mm by a 1/8" cylinder.

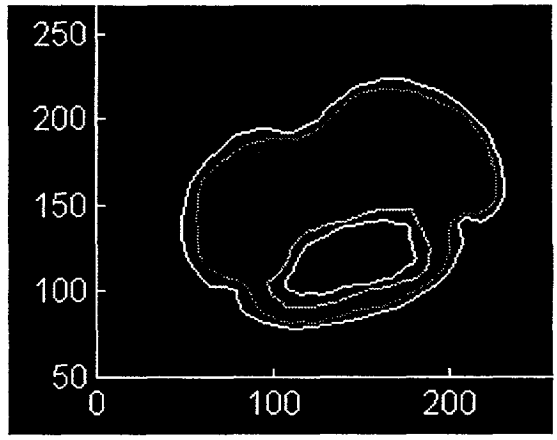

Figure F.10: Contours of fingerpad indented to 2 mm by a 1/8" cylinder.

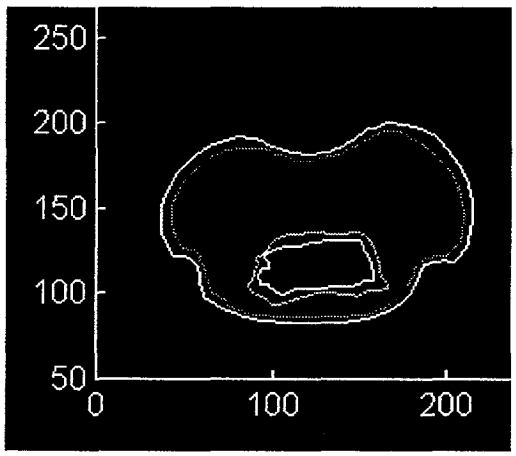

Figure F.11: Contours of fingerpad indented to 1mm with a 1/4" cylinder.

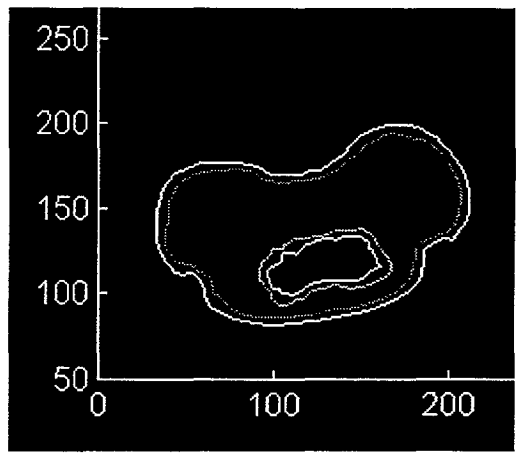

Figure F.12: Contours of fingerpad indented to 2mm with a 1/4" cylinder.

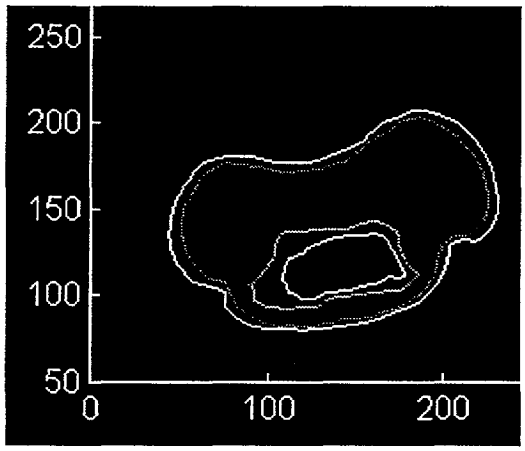

Figure F.13: Contours of fingerpad indented to 1mm with a 1/2" cylinder.

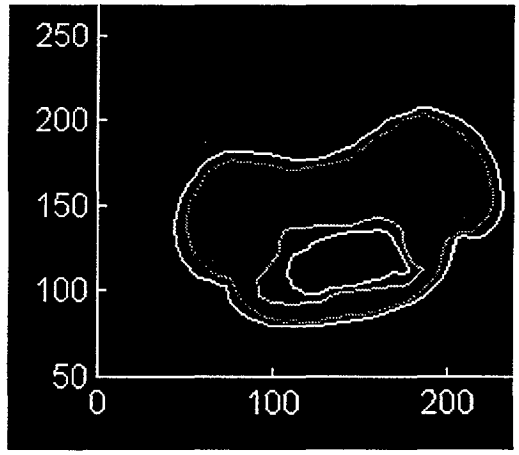

Figure F.14: Contours of fingerpad indented to 2 mm with a 1/2" cylinder.

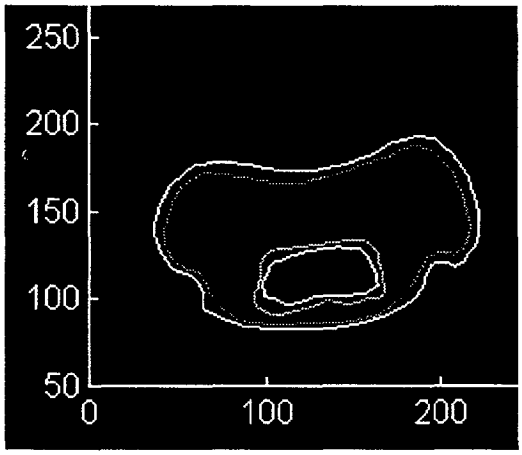

Figure F.15: Contours of fingerpad indented to 1 mm with a 1" cylinder.

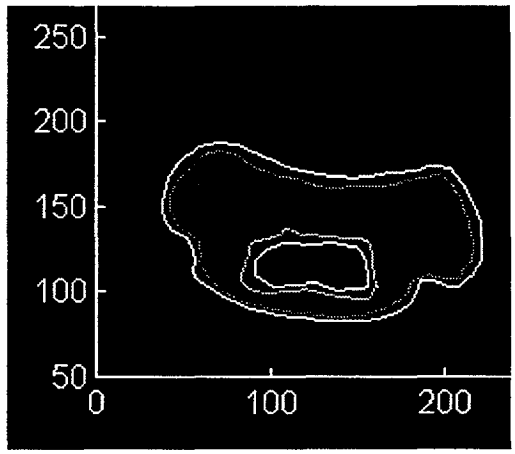

Figure F.16: Contours of fingerpad indented to 2 mm with a 1" cylinder.

Appendix G

Length and Area Calculations

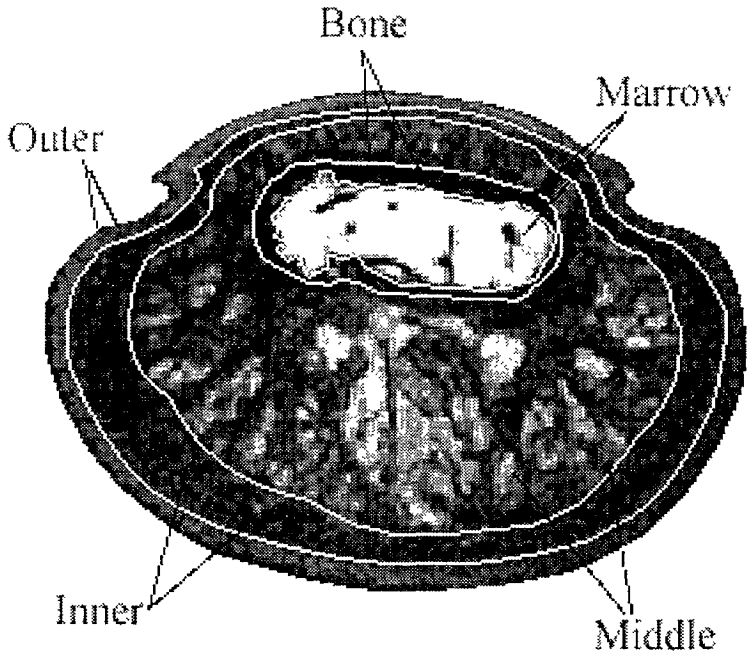

Subject 1

1 mm Indentation	Length Outer (mm)	Length Inner (mm)	Length Middle (mm)	Length Bone (mm)	Length Marrow (mm)
No Load	69.3287	62.785	53.8095	43.5627	42.8407
Lineload	70.5427	63.6106	59.1724	54.0913	53.997
Rectangular Bar - 1/16"	64.5963	58.6583	50.8668	44.0499	37.8318
Rectangular Bar - 1/8"	70.0603	64.102	56.2454	47.1	41.8078
Cylinder 1/8"	68.1862	61.951	55.0137	50.5499	44.9158
Cylinder 1/4"	68.2761	62.1172	56.2019	49.0601	43.8789
Cylinder 1/2"	70.2581	63.55	56.0534	52.632	46.0044
Cylinder 1"	67.1782	60.8292	54.1121	50.9623	44.1739

TableG.1: Table lists values of the length (mm) around a particular tissue boundary at 1 mm indentation.

1 mm Indentation	Area Outer (mm^2)	Area Inner (mm^2)	Area Middle (mm^2)	Area Bone (mm^2)	Area Marrow (mm^2)
No Load	53.7827	71.8576	169.979	14.793	27.9527
Line Load	48.5567	75.3583	150.2554	13.1874	29.5788
Rectangular Bar - 1/16"	45.3287	57.3146	127.2388	17.6341	20.0181
Rectangular Bar - 1/8"	43.5248	68.3136	143.0601	18.7588	31.3825
Cylinder 1/8"	45.0323	58.9572	154.2177	21.4912	28.3672
Cylinder ¼"	45.6382	51.7516	145.8911	20.5398	30.5214
Cylinder 1/2"	48.0106	52.1416	136.5302	23.2072	31.37
Cylinder 1"	44.3584	50.2307	117.7866	26.7441	27.4944

TableG.2: Table lists the calculated area for each tissue layer measured in mm^2 at 1mm indentation.

2 mm Indentation	Length Outer (mm)	Length Inner (mm)	Length Middle (mm)	Length Bone (mm)	Length Marrow (mm)
No Load	69.3287	62.785	53.8095	43.5627	42.8407
Lineload	71.5069	65.0654	58.0929	47.2407	43.4213
Rectangular Bar - 1/16"	70.3432	63.3756	55.4447	52.3089	45.5403
Rectangular Bar - 1/8"	69.7893	63.6879	54.8157	50.3605	45.0655
Cylinder 1/8"	66.7698	60.7078	55.2978	50.7207	44.7445
Cylinder 1/4"	69.3029	62.7013	55.3222	51.0453	44.4874
Cylinder 1/2"	69.7688	63.3461	55.4647	51.2832	46.5654
Cylinder 1"	69.0758	61.7578	54.8279	51.1131	44.577

TableG.3: Table lists values of the length (mm) around a particular tissue boundary at 2 mm indentation.

2 mm Indentation	Area Outer (mm^2)	Area Inner (mm^2)	Area Middle (mm^2)	Area Bone (mm^2)	Area Marrow (mm^2)
No Load	48.5567	75.3583	150.2554	13.1874	29.5788
Line Load	50.4982	55.1396	152.7611	21.1701	31.6903
Rectangular Bar - 1/16"	49.1524	60.446	120.309	27.4028	29.4215
Rectangular Bar - 1/8"	46.899	58.1511	126.8312	23.1947	27.9215
Cylinder 1/8"	46.4764	47.8618	141.0489	23.94	28.3672
Cylinder 1/4"	45.8231	57.0203	129.8363	25.388	30.7305
Cylinder 1/2"	44.0672	58.961	116.5755	19.9934	30.547
Cylinder 1"	48.1947	53.3627	124.0577	24.02049	30.6856

TableG.4: Table lists the calculated area for each tissue layer measured in mm^2 at 2mm indentation.

Subject 2

1 mm Indentation	Length Outer (mm)	Length Inner (mm)	Length Middle (mm)	Length Bone (mm)	Length Marrow (mm)
No Load	67.7822	61.9895	53.0539	38.608	34.4421
Lineload	67.8995	61.2381	52.9383	43.0089	40.2892
Rectangular Bar - 1/16"	70.0461	63.8676	55.8737	41.5719	36.5685
Rectangular Bar - 1/8"	67.681	61.9378	54.2492	43.3375	38.4082
Cylinder 1/8"	66.6279	60.6236	55.8065	41.5203	38.1178
Cylinder 1/4"	67.8555	61.9636	55.3302	36.4552	30.1552
Cylinder 1/2"	68.5115	62.8426	55.9987	44.4989	39.0136
Cylinder 1"	69.8541	64.0954	55.4356	42.795	38.3379

TableG.5: Table lists values of the length (mm) around a particular tissue boundary at 1 mm indentation.

1 mm Indentation	Area Outer (mm^2)	Area Inner (mm^2)	Area Middle (mm^2)	Area Bone (mm^2)	Area Marrow (mm^2)
No Load	54.3954	69.7159	155.3299	17.57378	23.9298
Line Load	56.893	88.4527	132.5226	12.392	10.013
Rectangular Bar - 1/16"	58.4066	61.7183	154.7948	15.1047	18.1709
Rectangular Bar - 1/8"	49.3822	65.7177	159.3894	17.8993	22.228
Cylinder 1/8"	53.6765	39.497	160.9302	13.0406	23.4995
Cylinder 1/4"	55.5101	50.5036	163.6256	16.6881	13.3714
Cylinder 1/2"	45.0117	56.0634	162.5778	17.8131	24.4308
Cylinder 1"	49.5888	64.5482	145.8655	16.135	26.127

TableG.6: Table lists the calculated area for each tissue layer measured in mm^2 at 1mm indentation.

2 mm Indentation	Length Outer (mm)	Length Inner (mm)	Length Middle (mm)	Length Bone (mm)	Length Marrow (mm)
No Load	67.7822	61.9895	53.0539	38.608	34.4421
Lineload	70.3307	65.1862	55.4878	30.9773	29.8217
Rectangular Bar - 1/16"	68.0801	62.6509	55.1321	42.5689	38.7695
Rectangular Bar - 1/8"	67.4616	62.0891	55.2993	39.5206	33.244
Cylinder 1/8"	63.4683	58.612	51.2892	27.476	22.7123
Cylinder 1/4"	68.8914	63.2917	53.1692	40.7055	37.3368
Cylinder 1/2"	68.4163	63.0059	52.6091	42.9406	39.8652
Cylinder 1"	67.3553	62.0668	52.1655	42.7553	38.0632

TableG.7: Table lists values of the length (mm) around a particular tissue boundary at 2 mm indentation.

2 mm Indentation	Area Outer (mm^2)	Area Inner (mm^2)	Area Middle (mm^2)	Area Bone (mm^2)	Area Marrow (mm^2)
No Load	54.3954	69.7159	155.3299	17.57378	23.9298
Line Load	49.8068	73.4995	155.9026	11.7308	25.7563
Rectangular Bar - 1/16"	58.1885	60.8606	143.8974	14.8538	18.1709
Rectangular Bar - 1/8"	47.5857	56.6773	156.7895	19.129	19.1925
Cylinder 1/8"	45.3441	58.3648	126.9911	9.7156	9.6273
Cylinder 1/4"	55.5684	70.0717	125.1908	12.1915	23.746
Cylinder 1/2"	54.2223	71.1232	130.1692	12.5737	20.0756
Cylinder 1"	48.3481	61.1672	110.7277	16.7592	19.885

TableG.8: Table lists the calculated area for each tissue layer measured in mm^2 at 2mm indentation.

Subject 3

1 mm Indentation	Length Outer (mm)	Length Inner (mm)	Length Middle (mm)	Length Bone (mm)	Length Marrow (mm)
No Load	62.5399	56.9485	49.3972	40.6243	46.6487
Lineload	61.0268	66.0174	65.8611	65.9004	63.2921
Rectangular Bar - 1/16"	61.7766	57.4875	50.4694	43.9006	38.9147
Rectangular Bar - 1/8"	61.5614	57.0504	52.5838	44.0541	38.6543
Cylinder 1/8"	66.2774	62.0516	54.4952	51.8348	46.2698
Cylinder 1/4"	61.8254	57.0725	49.9795	45.8616	41.3906
Cylinder 1/2"	64.0338	59.5958	52.3381	48.3679	40.4278
Cylinder 1"	61.6067	57.2929	50.0798	41.1121	36.73

TableG.9: Table lists values of the length (mm) around a particular tissue boundary at 1 mm indentation.

1 mm Indentation	Area Outer (mm^2)	Area Inner (mm^2)	Area Middle (mm^2)	Area Bone (mm^2)	Area Marrow (mm^2)
No Load	46.0645	57.252	135.854	9.2196	21.9053
Lineload	32.4255	47.8996	157.5256	8.2153	21.7503
Rectangular Bar - 1/16"	36.5215	42.6166	126.4334	14.5402	23.2806
Rectangular Bar - 1/8"	34.1615	39.4235	135.7486	18.451	23.9749
Cylinder 1/8"	40.973	57.3763	124.2358	20.1389	34.1509
Cylinder 1/4"	34.1769	50.4616	122.9919	14.3692	24.2097
Cylinder 1/2"	37.9618	54.7955	112.2868	22.8069	27.7249
Cylinder 1"	38.8643	46.6014	109.276	12.9445	24.4294

TableG.10: Table lists the calculated area for each tissue layer measured in mm^2 at 2mm indentation.

2 mm Indentation	Length Outer (mm)	Length Inner (mm)	Length Middle (mm)	Length Bone (mm)	Length Marrow (mm)
No Load	62.5399	56.9485	49.3972	40.6243	46.6487
Lineload	61.782	56.9919	58.6468	56.7722	52.01
Rectangular Bar - 1/16"	61.1272	56.8844	49.9907	44.8649	40.4725
Rectangular Bar - 1/8"	61.0214	56.8866	51.0699	44.5248	39.007
Cylinder 1/8"	65.5406	60.9021	53.7176	51.4146	45.2029
Cylinder 1/4"	61.4507	57.2899	49.5778	43.7941	39.9002
Cylinder 1/2"	65.4758	61.1573	54.9505	47.2469	41.5463
Cylinder 1"	61.0103	56.7231	49.6238	43.8139	38.5002

TableG.11: Table lists values of the length (mm) around a particular tissue boundary at 2 mm indentation.

2 mm Indentation	Area Outer (mm^2)	Area Inner (mm^2)	Area Middle (mm^2)	Area Bone (mm^2)	Area Marrow (mm^2)
No Load	46.0645	57.257	135.854	9.2196	21.9053
Lineload	36.1705	51.5617	113.9975	15.7424	22.0155
Rectangular Bar - 1/16"	33.5666	45.3855	119.0695	12.5199	22.81
Rectangular Bar - 1/8"	32.9153	43.7582	120.807	14.16	23.1189
Cylinder 1/8"	40.251	56.2339	137.0519	21.1017	33.4031
Cylinder 1/4"	34.9781	49.4598	107.2877	12.9179	21.1597
Cylinder 1/2"	35.9644	47.8774	115.0045	18.0564	29.6217
Cylinder 1"	35.4232	43.9772	98.8066	14.4565	23.1449

TableG.12: Table lists the calculated area for each tissue layer measured in mm^2 at 2mm indentation.

Appendix H

Matlab Program to Calculate Area and Length

```
%*************************************************
% Program to calculate area of each contour
% that was found using active contours
%
% created by Kimberly Voss and
% Dylan Birtolo
% created on 5/3/97
%*************************************************

clear
couter='couter';                    % Epidermis Layer
cinner='cinner';                    % Dermis Layer
cmid  ='cmid';                      % Adipose Layer
cbone ='cbone';                     % Bone Layer
cmarow='cmarow';                    % Bone Marrow Layer

% Select which image

snakes = ['couter'; 'cinner'; 'cmid  '; 'cbone '; 'cmarow'];
image = input('What image number would you like to plot? ');

%Fixes the image variable so that the program doesn't crash
%when it tries to look up a file that ends in 0x (i.e. 01, 02, etc.)

if image<=9
        image=['0',int2str(image)];
else
        image=int2str(image);
end;

% Load the contours for all five tissue layers for a given image.
```

```
% Calculate area and lengths for all five tissue layers.

for i=1:5
        eval(['load ',eval(snakes(i,:)),image]);
        points=size(xt,1);                      % Determine size of contour

% Calculate the lengths of the curves

        for j=1:(points-1)
                segment(j)=sqrt((xt(j)-xt(j+1))^2+(yt(j)-yt(j+1))^2);
        end
        segment(points)=sqrt((xt(1)-xt(points))^2+(yt(1)-yt(points))^2);
        length(i)=sum(segment);

% Calculate the area of each tissue layer

% Area is calculated using the trapezium rule
% area=1/2*base*(h1+h2) or area=1/2*h*(a+b)
%
% A trapezium was calculated for each set of
% two points and summed over the entire area.
% Each trapezium had to be determined if it
% added or subtracted from the area of the
% contour.

        areasum(i)=0.0;
        for k=1:points-1                % Calculate each trapezium
                h=abs(xt(k)-xt(k+1));
                a=yt(k);
                b=yt(k+1);
                area1=.5*h*(a+b);

                if xt(k+1)>xt(k)        % Check to see if it needs to be
                                        % added or subtracted from the total area
                        areasum(i)=areasum(i)+area1;
                else
                        areasum(i)=areasum(i)-area1;
                end
        end

        h=abs(xt(points)-xt(1));        %Calculate area between first and last points
        a=yt(points);
        b=yt(1);
        area1=.5*h*(a+b);
```

```
        if xt(1)>xt(points)             % Check to see if area needs to be
                                        % added or subtracted from the total area
                areasum(i)=areasum(i)+area1;
        else
                areasum(i)=areasum(i)-area1;
        end

end

area=areasum*125*125*10^-6              % Total area per contour in mm^2
diff(-area)                             % Differences between contours
l=length*125*10^-3                      % Length around contour in mm
```

Appendix I

Change in Area and Length

Subject 1

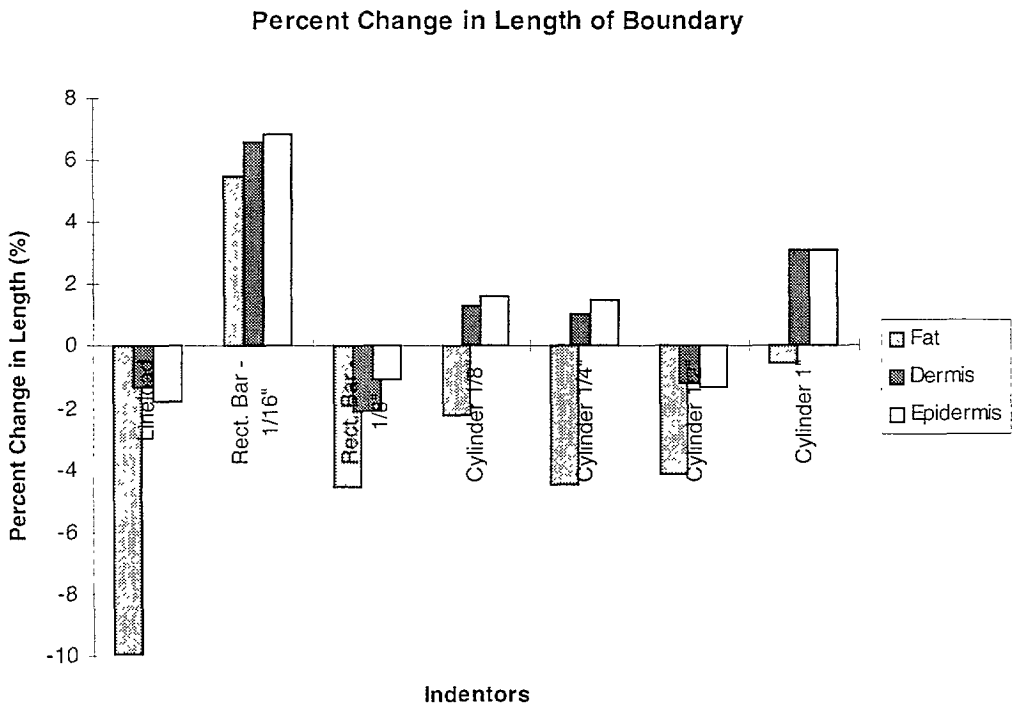

FigureI.1: Bar graph of the percent change in the boundary length of a particular tissue as a function of a particular indentor for a 1mm indentation.

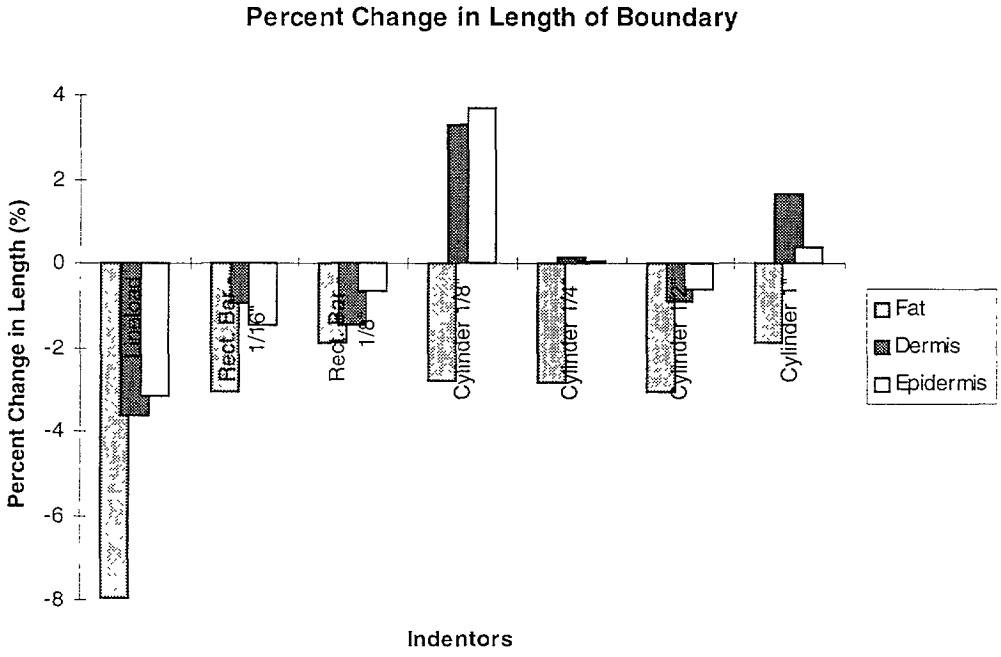

FigureI.2: Bar graph of the percent change in the boundary length of a particular tissue as a function of a particular indentor for a 2mm indentation.

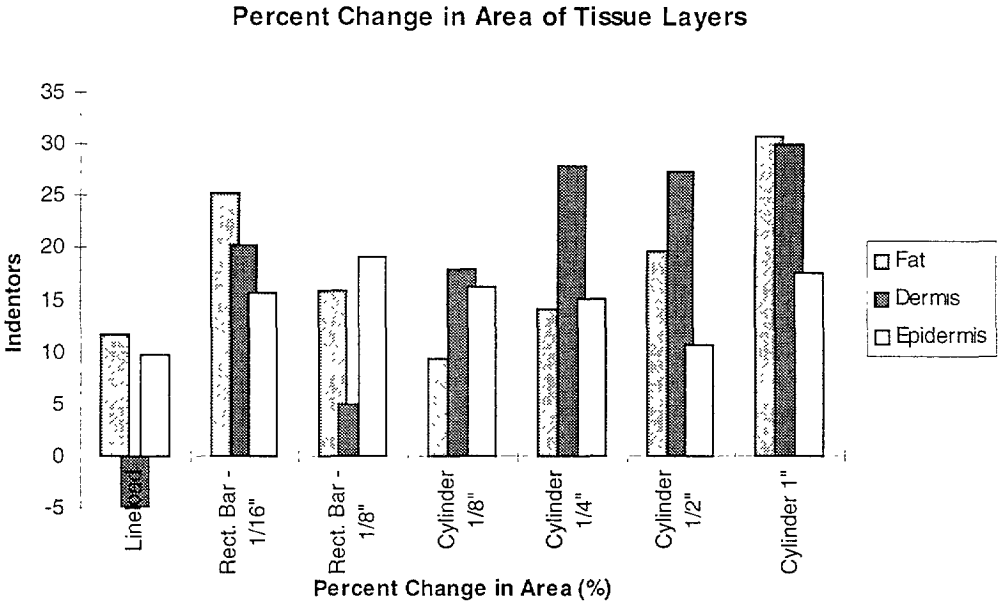

FigureI.3: Bar graph of the percent change in tissue area as a function of a particular indentor for a 1mm indentation.

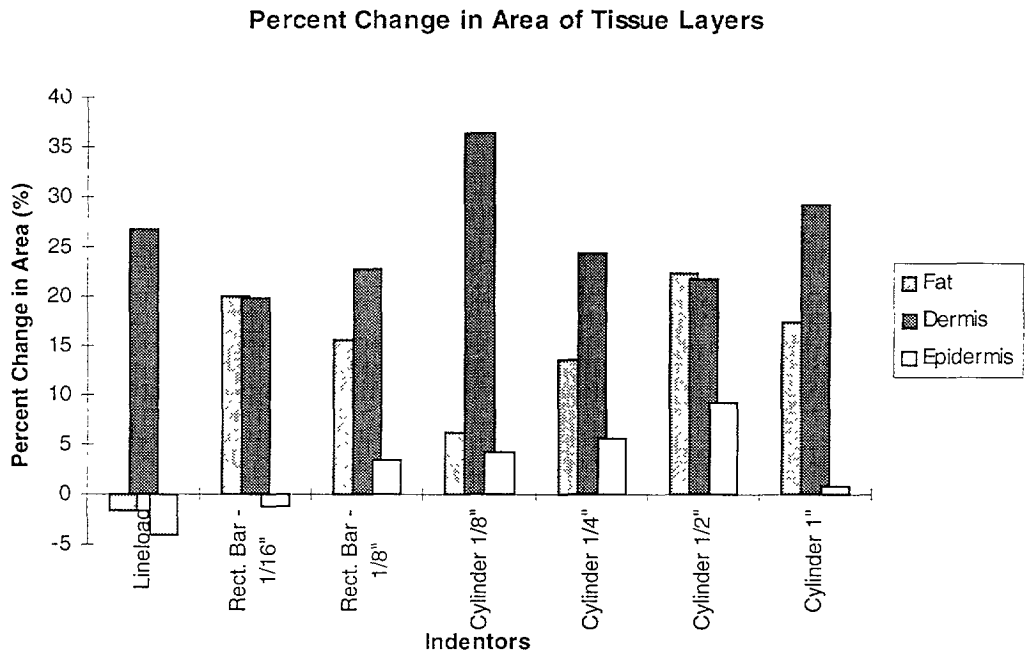

FigureI.4: Bar graph of the percent change in tissue area as a function of a particular indentor for a 2mm indentation.

Subject 2

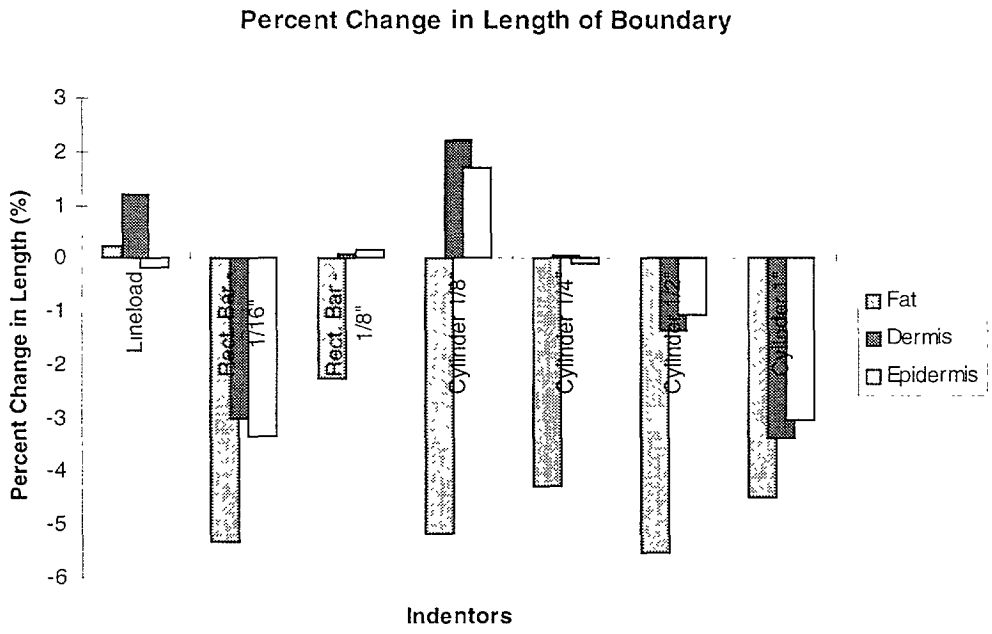

FigureI.5: Bar graph of the percent change in the boundary length of a particular tissue as a function of a particular indentor for a 1mm indentation.

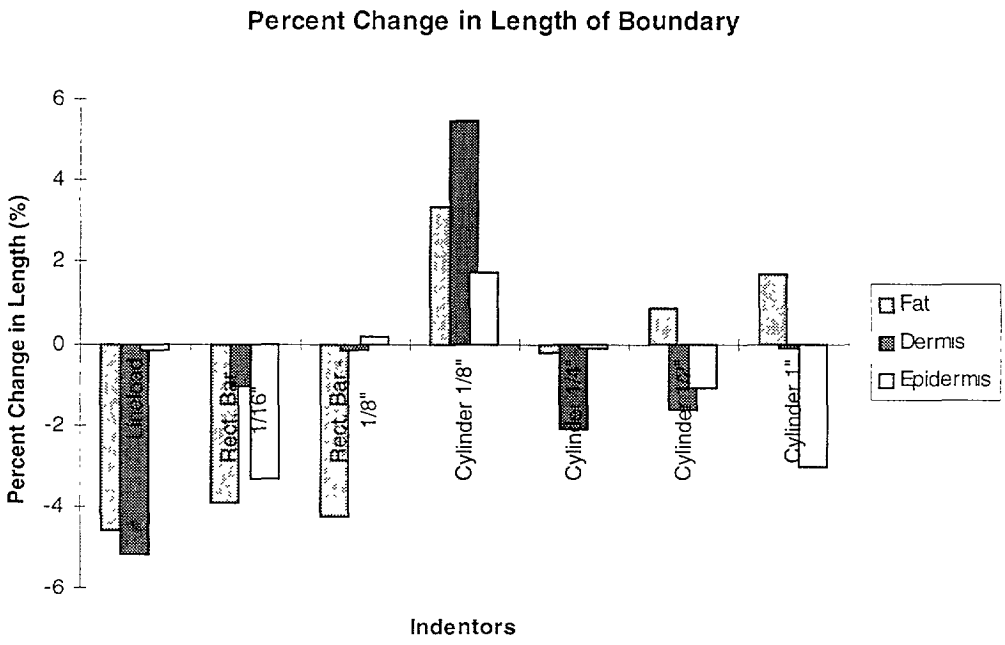

FigureI.6: Bar graph of the percent change in the boundary length of a particular tissue as a function of a particular indentor for a 2mm indentation.

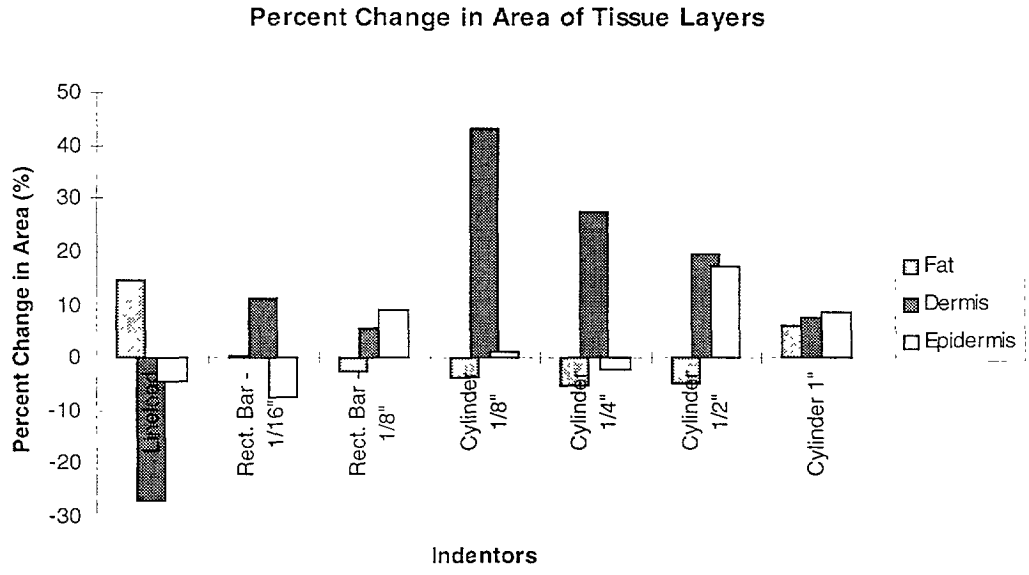

FigureI.7: Bar graph of the percent change in tissue area as a function of a particular indentor for a 1mm indentation.

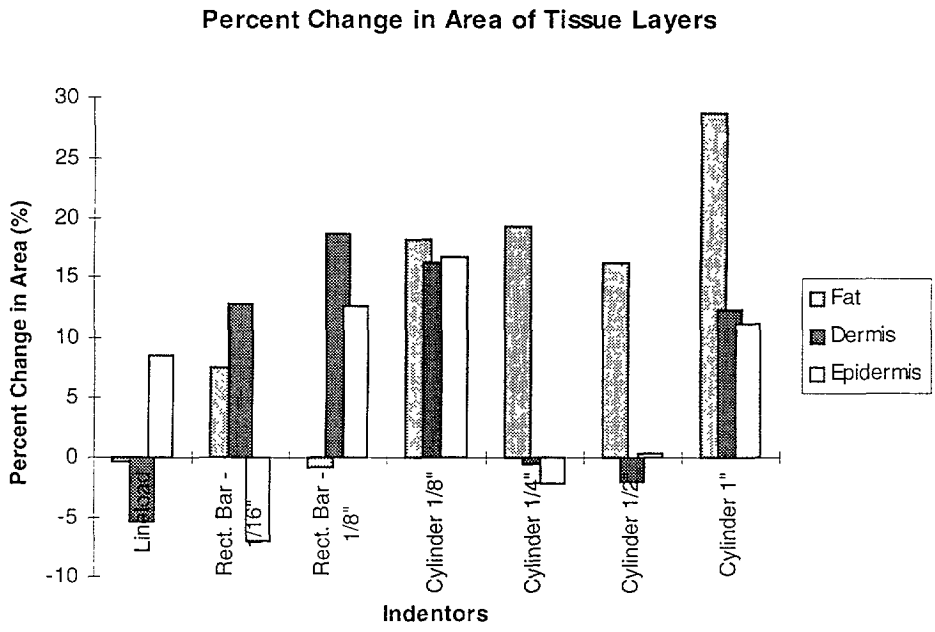

FigureI.8: Bar graph of the percent change in tissue area as a function of a particular indentor for a 2mm indentation.

Subject 3

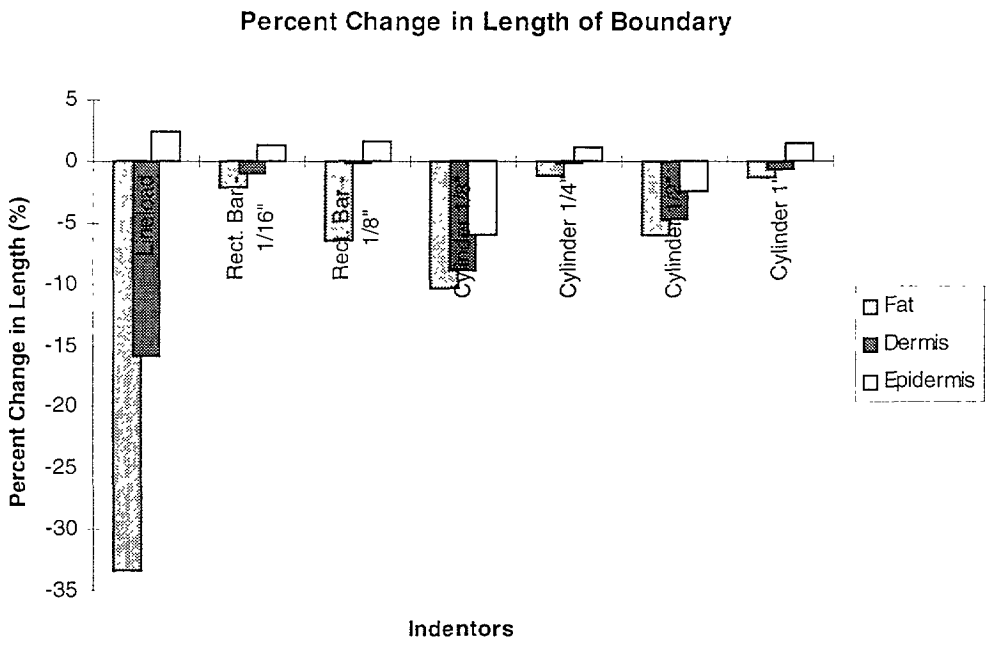

FigureI.9: Bar graph of the percent change in the boundary length of a particular tissue as a function of a particular indentor for a 1mm indentation.

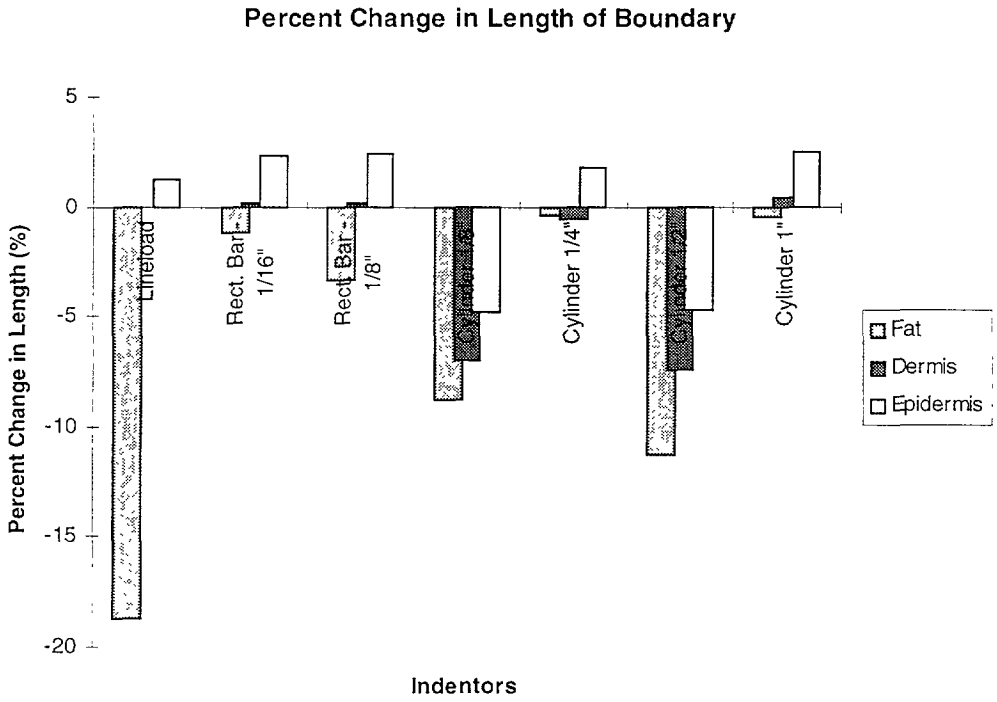

FigureI.10: Bar graph of the percent change in the boundary length of a particular tissue as a function of a particular indentor for a 2mm indentation.

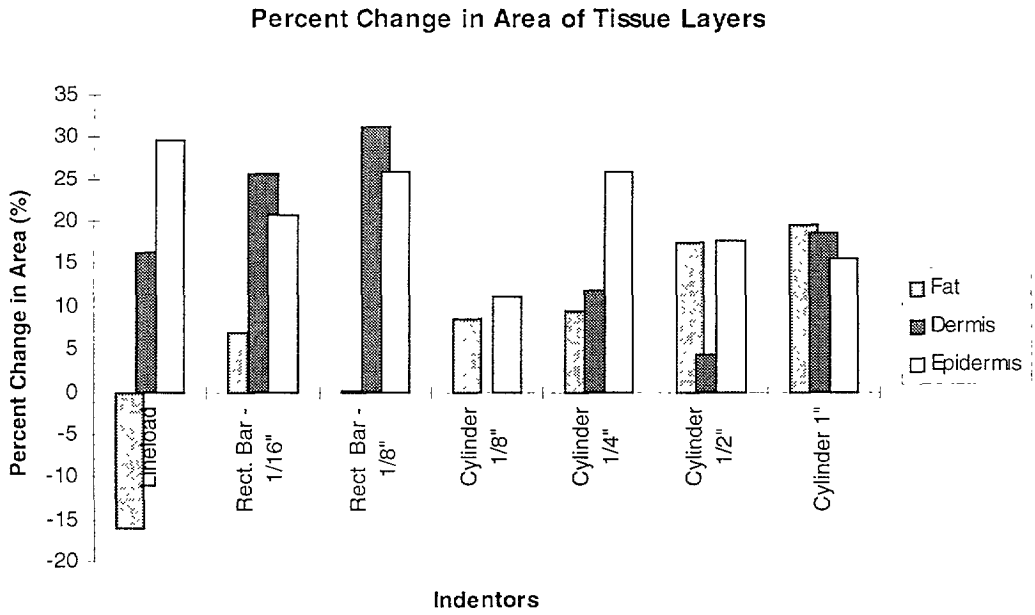

FigureI.11: Bar graph of the percent change in tissue area as a function of a particular indentor for a 1mm indentation.

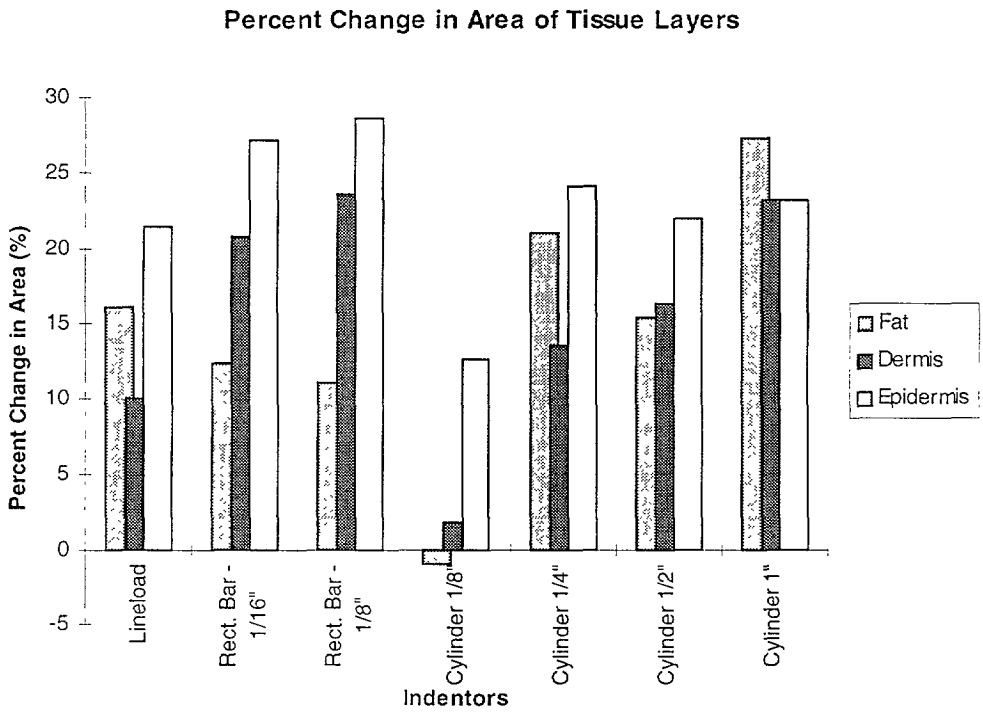

FigureI.12: Bar graph of the percent change in tissue area as a function of a particular indentor for a 2mm indentation.

Bibliography

Ablett, S., Burdett, N.G., Carpenter, A., Hall, L., and Salter, D. C., "Short Echo Time MRI enables Visualization of the Natural State of Human Stratum Corneum Water, *In Vivo*", *Magnetic Resonance Imaging*, Vol. 14, No. 4, 357-360, 1996.

Beltran, Javier, *MRI Musculoskeletal System*, J.B. Lippincott Company, Philadelphia, 1990.

Bittoun, J., Saint-Jalmes, H., Querleux, B.G., Darasse, L., Jolivet, O., Idy-Peretti, I., Wartski, M., Richard, S.B., and Leveque, J.L., "In Vivo High-Resolution MR Imaging of the Skin in a Whole-Body System at 1.5T", *Radiology*, 457-460, 1990.

Burdea, Grigore, *Force and Touch Feedback for Virtual Reality*, John Wiley & Sons, Inc., New York, 1996.

Carlbom, Ingrid, Terzopoulos, and Harris, Kristen, 'Computer-Assisted Registration, Segmentation, and 3D Reconstruction from Images of Neuronal Tissue Sections, *IEEE Transactions on Medical Imaging*, Vol. 13, No. 2, June, 1994.

Dandekar, K., "Role of Mechanics in Tactile Sensing of Shape," Ph.D. Thesis, Massachusetts Institute of Technology, 1995.

Dandekar, K. and Srinivasan, M.A.," *Role of Mechanics in Tactile Sensing of Shape*", RLE TR-604, MIT, 1996.

Dandekar, K. and Srinivasan, M.A., "Tactile Coding of Object Curvature by Slowly Adapting Mechanoreceptors," *Advances in Bioengineering*, Vol. 28, 41-42, 1994.

Danielson, D.A., "Human Skin as an Elastic Membrane," *J. Biomechanics*, Vol. 6, 539-546, 1973.

Darian-Smith, I., "The Sense of Touch: Performance and Peripheral Neural Processes," *Handbook of Physiology - The Nervous System- III*, 739-788, 1984.

Darian-Smtih, I. And Kennis, P., "Innervation Density of Mechanoreceptive Fibers Supplying Glabrous Skin of the Monkey's Index Finger," *Journal of Physiology (London)*, Vol. 309, 147-155, 1980.

Darian-Smith, I., Davidson, I., and Johnson, K. O., " Peripheral Neural Representation of Spatial Dimensions of a Textured Surface Moving Across the Monkey's Fingerpad, " *Journal of Physiology (London)*, 135-146, 1980.

Dellon, A. L., *Evaluation of Sensibility and Re-education of Sensation in the Hand.* Williams and Wilkins, Baltimore, 1981.

Erickson, S. Kneeland, J.B., Middletown W.D., Jesmanowicz, A., Hyde, J., Lawson, T. L., and Foley, W.D., "MR Imaging of the Finger: Correlation with Normal Anatomic Sections", *American Journal of Roentgenology*, Vol. 152, No 5, 1013-1019, 1989.

Fung, Y. C., *Biomechanics.* Springer, New York, 1981.

Fung, Y. C., *Biomechanics: Mechanical Properties of Living Tissues.* Springer-Verlag, Second Ed., 1993.

Gardner, E., Gray, D.J., O'Rahilly, R., *Anatomy: A Regional Study of Human Structure*, 3rd Ed., W. B. Saunders & Co., 55-61, 1969.

Gries, P., Constantinesco, A., Brunot, B., and Facello, A., "MR Imaging of Hand and Wrist with a Dedicated 0.1-T Low-Field Imaging System", *Magnetic Resonance Imaging*, Vol. 9, 949-953, 1991.

Gulati, R. J., "Force Displacement Response of Human Fingertips," Master's Thesis, Boston University, 1995.

Gulati, R.J., "In Vivo Compressibility of the Human Fingerpad", Bachelor's Thesis, Massachusetts Institute of Technology, 1992.

Hazelman, Brian L., MB and Tyler, Jenny A., Tyler, " Magnetic Resonance Imaging Protocol Optimization for Evaluation of Hyaline Cartilage in the Distal Interphalangeal Joint of Fingers", *Investigative Radiology*, Vol. 30, No. 9, 522-531, 1995.

Hennig, J., Nauerth, A. and Friedbur, H., "RARE Imaging: A Fast Imaging Method for Clinical MR", *Magnetic Resonance in Medicine*, Vol. 3, 823-833, 1996.

Hodgson, Richard J., Barry, Maurice A., Carpenter, Adrian, Hall, Laurence, Hall, Hazleman, Brian and Tyler, Jenny A., "Magnetic Resonance Imaging Protocol Optimization for Evaluation of Hyaline Cartilage in the Distal Interphalangeal Joint of Fingers", *Investigative Radiology*, Vol. 30, No. 9, 522-531, 1995.

Johansson, R. S., "Tactile Sensibility in the Human Hand: Receptive Field Characteristics of Mechanoreceptive Units in the Glabrous Skin Area," *Journal of Physiology,* Vol. 281, 101-123, 1978.

Kass, Michael, Witkin, Andrew, and Terzopoulos, Demetri, "Snakes: Active Contour Models", *International Journal of Computer Vision*, 321-331, 1988.

Kean, D.M., and Smith, M.A., *Magnetic Resonance Imaging: Principles and Applications*, Williams & Wilkins, Baltimore, 1986.

Landsmeer, J., *Atlas of Anatomy of the Hand*, Churchill Livingstone, New York, 1976.

Lanir, Y., "Skin Mechanics," *Handbook of Bioengineering*, McGraw-Hill, New York, 11.1-11.25, 1987.

Lanir, Y., Dikstein, S., Hartzshtark, A., and Manny, V., "*In Vivo* Indentation of Human Skin," *Journal of Biomechanics,* Vol. 112, 63-69, 1990.

Lockhart, R.D., Fyfe, F.W., and Hamilton, G.F., "The Skin", *Anatomy of the human body*, J.P. Lippincott Company, Philadelphia, 3-6, 1965.

Lufkin, Robert, *The MRI Manual*, Year Book Medical Publishers, Inc., Littleton, Mass., 1990.

McInerney, Tim, and Terzopoulos, Demetri, "Medical Image Segmentation Using Topologically Adaptable Snakes", ???, 92-101.

Palmer, P.L., Dabis, H., and Kittler, J., "A Performance Measure for Boundary Detection Algorithms", *Computer Vision and Image Understanding*, Vol. 63, No. 3, May, 476-494, 1996.

Partain, C. Leon, James, A. Everette, Rollo, F. David, and Price, Ronald R., *Nuclear Magnetic Resonance NMR Imaging*, W. B. Saunders Company, Philadelphia, 1983.

Querleux, B. Richard, S. Bittoun, J. Jolivet, O., Idy-Peretti, I., Bazin, R. and Leveque, J., "In Vivo Hydration Profile in Skin Layers by High Resolution Magnetic Resonance Imaging", *Skin Parmacol.*, Vol. 7, 210-216, 1994.

Sandzen, S., *Atlas of Acute Hand Injuries*, McGraw-Hill Book Company, New York, 1980.

Seyfert, Sepp, Boegner, Friedrich, Hamm, Bernd, Kleindienst, Andrea, and Klatt, Christel, "The Value of Magnetic Resonance Imaging in Carpal Tunnel Syndrome", *Journal of Neurology*, Vol. 242, 41-46, 1994.

Srinivasan, M.A., "Surface Deflection of Primate Fingertip Under Line Load," *Journal of Biomechanics*, Vol. 22, No. 4, 343-349, 1989.

Srinivasan, M. A. and Dandekar, K., "An Investigation of the Mechanics of Tactile Sense Using Two-Dimensional Models of the Primate Fingertip," Transactions of the ASME, Vol. 118, February, 48-55, 1996.

Srinivasan, M. A. and Dandekar, K., "Role of Fingertip Geometry in Transmission of Tactile Mechanical Signals," *Advances in Bioengineering*, Vol. 22, 569-572, 1992.

Srinivasan, M. A. and Dandekar, K. "Mechanistic Models for Tactile Neural Coding of Shape," *Society of Neuroscience Abstracts*, 1994b.

Srinivasan, M. A., Gulati, R. J., and Dandekar, K., "*In Vivo* Compressibility of the Human Fingerpad," *Advances in Bioengineering*, Vol. 22, 573-576, 1992.

Song, Hee Kwon, Wehrli, Felix W., and Ma, Jingfei, "In Vivo MR Microscopy of the Human Skin", *MRM*, Vol. 37, 185-191, 1997.

Stoller, David, *Magnetic Resonance Imaging in Orthopaedics & Sports Medicine*, New York, Lippincott-Raven, 2nd Ed., 1997.

Tregear, R.T., *Physical Functions of Skin*, Academic Press, New York, 1966 .

Tubiana, E.R., "The Hand", W. B. Sanders Co., Vol. 1, 107-120, 1987.

Weis, J., Gorke, U., and Kimmich, R., "Susceptibility, Field Inhomogeneity, and Chemical Shift-Corrected NMR Microscopy: Application to the Human Finger In Vivo", *Magnetic Resonance Imaging*, Vol. 14, Vol. 14, No. 10, 1165-1175, 1996.

Weiss, Kenneth L., MD, Beltran, Javier, MD, Shamam, Omran M., MD, Stilla, Randall F., MS, Levey, and Michael, BA, "High-Field MR Surface-Coil Imaging of the Hand and Wrist. Part I. Normal Anatomy", *Radiology*, Vol.160, No. 1, 143-146, 1986.

Weiss, K.L., Beltran J., Shaman OM, Stilla R.F., and Levey M. , "High-field MR Surface Coil Imaging of the Hand and Wrist. Part II. Pathologic Correlations and Clinical Relevance", *Radiology,* Vol. 160, 147-152, 1986.

Wright, G.A., "Magnetic Resonance Imaging", *IEEE Signal Processing Magazine*, January, 1997.

Young, Stuart, *Magnetic Resonance Imaging: Basic Principles*, Raven Press, New York, 2nd Ed., 1988.